

RAPIDITY GAP IN THE FINAL STATE HADRON DISTRIBUTION
IN DEEP INELASTIC ELECTRON SCATTERING AT HERA

by

Thomas Keith Blankenship

Dissertation submitted to the Faculty of the
Virginia Polytechnic Institute and State University
in partial fulfillment of the requirements for the degree of

DOCTOR OF PHILOSOPHY

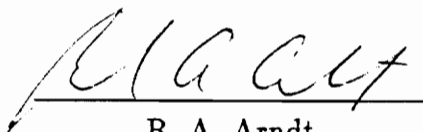
in

Physics

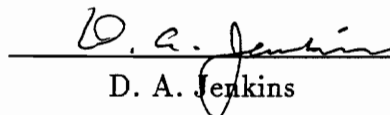
APPROVED:



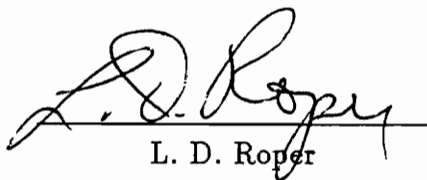
Luke W. Mo, Chairman



R. A. Arndt



D. A. Jenkins



L. D. Roper



C. D. Williams

February, 1995
Blacksburg, Virginia

C.2

LD
5655

V856

1995

B536

C.2

RAPIDITY GAP IN THE FINAL STATE HADRON DISTRIBUTION IN DEEP INELASTIC ELECTRON SCATTERING AT HERA

by

Thomas Keith Blankenship

Committee Chairman: Luke W. Mo

Physics

(ABSTRACT)

The rapidity space available for hadron production in electron-proton interactions at HERA is 11.4 units in width. In such a space the separation of virtual photon fragmentation from proton fragmentation is observed in events where the invariant mass of the final state hadronic system, W , is greater than 130 GeV. Experimental cross sections for the virtual photon fragmentation process are presented. A new class of events is identified, where *only* virtual photon fragmentation and no proton fragmentation is observed. In the final state hadronic system of these events a rapidity gap over four units in width was discovered. Cross sections for these events are also presented, and comparisons are made with the theoretical predictions of the pomeron and hard diffraction models.

Acknowledgements

I hereby gratefully acknowledge those who made the writing of this dissertation possible.

My advisor, Professor Luke W. Mo, pushed our small contingent on ZEUS from Virginia Tech to produce noteworthy results. He gave me my first lessons on particle physics, and taught me the theory and experiment of deep inelastic scattering and neutrino scattering, and the rudiments of the standard model. I am indebted to him for giving me a solid foundation in the methods of experimental physics as well as providing me with the opportunity and tools needed to participate in a cutting-edge high energy physics experiment. On a higher plane, he impressed in me the need to strive for excellence in science, and the fact that in science earth-shattering discoveries are not the norm. On the contrary, we learn little by little, carefully understanding each step before proceeding to the next.

My coworker, Dr. Bin Lu, invested many hours in the research which is presented in this dissertation. Her work was invariably of the highest quality, and in preparing this dissertation I appreciate her allowing me to draw freely on the results she produced. Through constant discussions over three years she helped me make great strides in doing physics.

Ms. Chris Thomas, our physics department secretary, has been immensely supportive of the Virginia Tech members of ZEUS over the years. She has gracefully handled the logistics necessary for members of one team to work effectively on two continents simultaneously.

The National Science Foundation, under grant number PHY-9308074, generously provided the financial support necessary to perform the work which produced the results presented in this dissertation.

The large group of physicists and engineers who constructed the ZEUS detector, the members of ZEUS who oversaw the data-taking operation, and the offline group which reconstructed the data are to be highly commended. I thank them for their painstaking efforts which made this analysis possible.

An excellent performance was turned in by the HERA accelerator group which kept the world's first electron-proton collider running day and night during data-taking. I thank them for their efforts in producing the electron-proton collisions which are analyzed in this dissertation.

I can honestly say that throughout my graduate studies not a single negative or discouraging remark was uttered by my friends and family, but only that which was useful for my edification.

Dr. Loren Rees provided the impetus I needed to survive down the homestretch.

Dr. and Ms. Joe Kochocki provided friendship and nourishing dinners, both in Hamburg, Germany and in Blacksburg.

The congregations at International Baptist Church in Hamburg, Harvest Baptist Church in Blacksburg, and Berean Baptist Church in Manassas bolstered me with their prayers.

My dear friend, Shun Hua Zhou, was a godsend. She was always praying for me; offering me words of consolation, encouragement, or advice; tolerating me at my worst; and in general making my life a happier one. Although she is now a Texas cowgirl she is still a Hokie at heart.

Finally, I would be remiss were I not to thank my family: Karen, Dad and Mom (Thomas and Eula Blankenship). They have unconditionally supported me in every endeavor I have undertaken, always encouraging me to endure in spite of disappointments or difficulties. In providing a Christian home in which to grow up, they attempted to instill in me the simple virtues of honesty, always doing one's best, and treating everybody with the decency and respect that human beings deserve – lofty ideals I humbly hope to transmit to the next generation.

It is to my parents that I dedicate this work, trusting that it offers a little bit more knowledge about the world around us as well as revealing in yet another instance the majesty and wisdom of the One who created it. As such, it would then satisfy the motto, "For the enrichment of humankind, and to the greater glory of God."

Contents

Title	i
Abstract	ii
Acknowledgements	iii
Table of Contents	vi
List of Figures	xi
List of Tables	xiii
1 Introduction and Overview	1
2 Experimental Apparatus	7
2.1 The Electron-Proton Collider HERA	7
2.2 The ZEUS Detector	8
2.2.1 Calorimeter	8
2.2.1.1 Requirements of the Calorimeter	8
2.2.1.2 Physics of Calorimetry and Compensation	10
2.2.1.3 Mechanical Construction and Readout	17
2.2.1.4 Test Results and Calibration	22
2.2.1.5 The DU Signal	23

2.2.2	Tracking Systems	25
2.2.2.1	Central Tracking Detector (CTD)	25
2.2.2.2	Superconducting Solenoid	27
2.2.2.3	Vertex Detector (VXD)	28
2.2.2.4	Forward and Rear Tracking Detectors (FTD, RTD) .	28
2.2.2.5	Transition Radiation Detector (TRD)	29
2.2.3	Veto Wall	30
2.2.4	C5 Counter	30
2.2.5	Luminosity Monitor	31
2.2.6	Iron Yoke and Backing Calorimeter	32
2.2.7	Muon Detection System	32
2.2.8	Data Acquisition System	34
3	Data-taking	36
3.1	Accelerator Operation	36
3.1.1	Beam Collisions	36
3.1.2	Typical Running Conditions	38
3.2	Detector Operation	39
3.2.1	Experimental Running	39
3.2.2	Backgrounds to Deep Inelastic Scattering	40
3.2.2.1	Beam-gas Interactions	40
3.2.2.2	Cosmic Ray Muons	42
3.2.2.3	Sparks	43
3.2.3	Online Trigger	44
3.2.4	Dead Time	46
4	Selection of DIS Events and Identification of the Scattered Elec-	
	tron	47
4.1	Summary Data	47

4.2	Selection of DIS Events from the Summary Data	49
4.2.1	Event Timing	49
4.2.2	Event Vertex	50
4.2.3	$E - P_z$ Requirement	50
4.2.4	C5 and Veto Wall	52
4.2.5	Detector Conditions	52
4.3	Identification of the Scattered Electron	53
4.3.1	Calorimeter Clusters	53
4.3.2	Determination of the Scattered Electron Cluster	54
4.3.3	Efficiency and Misidentification in Finding the Scattered Elec- tron	55
4.3.4	Position and Angle Measurement of the Scattered Electron . .	55
4.3.5	Scattered Electron Energy Restriction	58
4.3.6	Scattered Electron Impact Position Restriction	58
4.3.7	Scattered Electron Angle Restriction	59
5	Radiative Corrections and Acceptance Calculations Using Monte Carlo Methods	60
5.1	The Monte Carlo Package	60
5.2	Acceptance and Efficiency Calculations	62
5.2.1	$(E - P_z)$ Acceptance	62
5.2.2	Scattered Electron Impact Position Acceptance	62
5.2.3	Trigger Efficiency	63
5.2.4	Efficiency for Identifying the Scattered Electrons	63
5.2.5	Electron Scattering Angle Resolution	64
5.3	Radiative Corrections	65
6	The Cross Sections for Final State Hadrons in Electron-Proton Scattering	67

6.1	The Final State Hadrons	68
6.1.1	The Analysis Method	68
6.1.1.1	Calculation of the Rapidity	68
6.1.1.2	Lorentz Transformation for CMS Analysis	69
6.1.1.3	Correction Procedure and Cross Section Calculation	69
6.1.1.4	Error Calculation	70
6.1.1.5	Background Subtraction	70
6.1.2	Analysis of the Rapidity Distributions	71
6.1.2.1	Rapidity Distributions for Large and Small W	71
6.1.2.2	Event Classification Based on the Rapidity Distribution	71
6.2	Cross Sections for Virtual Photon Fragmentation	73
6.2.1	Q^2 Distribution	74
6.2.2	x Distribution	75
6.2.3	$m_{\gamma^*}^2$ Distribution	76
6.2.4	P_t Distribution	77
6.2.5	T Distribution	78
6.2.6	β Distribution	79
7	Physics Results and Conclusions	80
7.1	Summary	80
7.2	Physics Results	80
7.3	Conclusions	83
A	Cross Sections for Deep Inelastic Scattering	85
A.1	Conventions for Four-momenta and Units	85
A.2	Cross Section for Single Photon Exchange	86
A.3	Electroweak Neutral Current Electron-Proton Scattering Cross Section	90

A.4 Cross Sections for the Absorption of Longitudinally and Transversely Polarized Virtual Photons	94
B Kinematic Relations in Deep Inelastic Scattering at HERA	97
References	100
Tables	109
Figures	114
Vita	158

List of Figures

1	$Q^2 - \nu$ space at HERA	115
2	$Q^2 - x$ space at HERA	116
3	The electron-proton collider HERA	117
4	The ZEUS detector	118
5	A r - z projection of the ZEUS detector	119
6	A x - y projection of the ZEUS detector	120
7	Visible energy from proton recoil and neutron capture	121
8	Variation of degree of compensation with DU/scintillator thickness	122
9	A single FCAL tower	123
10	A FCAL module	124
11	The FCAL as seen from the interaction point	125
12	The RCAL as seen from the interaction point	126
13	A BCAL module	127
14	Cross sectional view through a BCAL tower.	128
15	CTD superlayer structure	129
16	A VXD cell	130
17	The ZEUS F/RTD system	131
18	The ZEUS luminosity monitoring system	132
19	Schematic of the ZEUS data acquisition system	133
20	A single calorimeter cluster	134
21	Two calorimeter clusters touching on a corner	135

22	Two calorimeter clusters due to two local maxima	136
23	$(E - P_z)$ acceptance	137
24	Scattered electron identification efficiency	138
25	One boson exchange diagrams	139
26	One photon emission diagrams	140
27	One loop diagrams	141
28	Radiative correction factors	142
29	η_{cms} distributions for large and small W	143
30	$d\sigma/d\eta_{cms}$ for photon and proton fragmentation events	144
31	$d\sigma/d\eta_{cms}$ for photon fragmentation only events	145
32	Experimental $d\sigma/dQ^2$ compared with POMPYT result	146
33	Experimental $d\sigma/dQ^2$ compared with NIKZAK result	147
34	Experimental $d\sigma/dx$ compared with POMPYT result	148
35	Experimental $d\sigma/dx$ compared with NIKZAK result	149
36	Experimental $d\sigma/dm_{\gamma^*}^2$ compared with POMPYT result	150
37	Experimental $d\sigma/dm_{\gamma^*}^2$ compared with NIKZAK result	151
38	Experimental $Ed^3\sigma/d\vec{p}^3$ compared with POMPYT result	152
39	Experimental $Ed^3\sigma/d\vec{p}^3$ compared with NIKZAK result	153
40	Experimental $d\sigma/d T $ compared with POMPYT result	154
41	Experimental $d\sigma/d T $ compared with NIKZAK result	155
42	Experimental $\beta d\sigma/d\beta$ compared with POMPYT result	156
43	Experimental $\beta d\sigma/d\beta$ compared with NIKZAK result	157

List of Tables

1	Parameters of HERA Beams	110
2	Parameters of HERA Rings	111
3	Subtriggers Involving Calorimeter Alone	112
4	Subtriggers Involving Calorimeter and Other Components	113

Chapter 1

Introduction and Overview

The concept that hadrons are composite objects consisting of point-like, spin-1/2 particles with fractional charges was introduced by Gell-Mann [1] and independently by Néeman [2]. This static “quark” model, based on an $SU(3)$ group representation, reproduced the observed hadron spectroscopy at low masses, successfully classifying them into octets and decuplets. The quark model had the same organizing effect for the hadrons that Mendeleev’s periodic table had for the chemical elements. Mesons were explained as being composites of quark-antiquark pairs, and baryons were explained as being composites of three quarks. One problem with the model was that some hadrons, the Δ^{++} for instance, were supposedly composed of three identical spin-1/2 quarks, in direct contradiction to Pauli’s exclusion principle. This inconsistency was remedied by Greenberg [3] who, working with an $SU(3)_C$ group representation, introduced the idea that quarks have another attribute, one of three “colors”, but that physical hadrons are color singlets, i.e., “colorless”.

It was first established by the SLAC–MIT deep inelastic scattering (DIS) experiment at the Stanford Linear Accelerator Center (SLAC) [4] that the nucleon does indeed consist of “point-like constituents”. This was done by measuring the differential electron-nucleon scattering cross section (see Appendix A.2), which behaved as the incoherent summation of the scattering cross sections of electrons from point-like

particles. It was proved that the spin of these particles was $1/2$ by measuring the ratio $R = \sigma_L/\sigma_T$ to be approximately 0.18, where the quantities σ_L and σ_T are the cross sections for the absorption of longitudinally and transversely polarized virtual photons, respectively (see Appendix A.4). Also it was observed that nearly half of the momentum transferred to the nucleon target was missing. This was the first indication that momentum was carried away by unobserved neutral particles, which were later identified with the “gluons” as that conjectured in the Yang-Mills field theory [5]. The existence of the three color attributes was subsequently confirmed in an e^+e^- annihilation experiment at CEA (Cambridge Electron Accelerator) by examining the ratio R , defined by $\sigma(e^+e^- \rightarrow \text{hadrons})/\sigma(e^+e^- \rightarrow \mu^+\mu^-)$ [6].

Feynman interpreted the SLAC-MIT results by picturing the nucleon as being composed of an indefinite number of point-like, spin- $1/2$ particles (see Appendix A.3) which he named “partons” [7]. These partons were identified with Gell-Mann’s quarks, hence they acquired the name “quark-parton”. Feynman’s parton model is a very physical description of nucleon structure: in the infinite momentum frame of the nucleon target, each parton carries a fraction of the total four momentum of the target. This fraction is designated by a scaling variable [8], the well-known Bjorken-Feynman “ x ” (see Appendix B).

Kuti and Weisskopf introduced the idea that a quark-antiquark “sea” was part of the nucleon composition [9], and henceforth nucleons have been considered as being made of “valence” quarks at larger values of x and sea quarks at lower values of x . In the language of Regge theory [10], the valence quarks are equivalent to Regge poles and the sea quarks are equivalent to pomerons. Regge theory is useful in that it describes the general characteristics of scattering amplitudes; however, it makes precise predictions only for the charge exchange reaction, $\pi^-p \rightarrow \pi^0n$ [11]. Nevertheless, the Regge pole and pomeron analysis still holds an important position in physics today.

After the establishment of the quark-parton model the combination of a vast array of experimental discoveries on new quarks and leptons along with theoretical effort led to the successes of the “standard model” [12] based on an $SU(3)_C \times SU(2)_L \times U(1)_Y$ group structure. The main ingredients of the standard model are six left-handed quarks and leptons, arranged in three iso-doublets each:

$$\begin{pmatrix} u \\ d \end{pmatrix}_L \quad \begin{pmatrix} c \\ s \end{pmatrix}_L \quad \begin{pmatrix} t \\ b \end{pmatrix}_L \quad (\text{the quarks})$$

$$\begin{pmatrix} \nu_e \\ e^- \end{pmatrix}_L \quad \begin{pmatrix} \nu_\mu \\ \mu^- \end{pmatrix}_L \quad \begin{pmatrix} \nu_\tau \\ \tau^- \end{pmatrix}_L \quad (\text{the leptons}).$$

The upper member of each family of quarks has $Q = 2/3$ and $I_3 = 1/2$, where Q is the electric charge in units of the absolute value of the electron charge and I_3 is the third component of isospin. The lower member of each family of quarks has $Q = -1/3$ and $I_3 = -1/2$. Each quark also carries one of the three color attributes, commonly denoted by red, blue, and green. The upper member of each family of leptons has $Q = 0$ and $I_3 = 1/2$ while the lower member has $Q = -1$ and $I_3 = -1/2$. For each lepton and quark there is a corresponding antiparticle of opposite Q and I_3 . In the standard model additional right-handed quarks and leptons in the iso-singlet state were also introduced. They are required for the structure of interaction currents in the theory.

Four gauge bosons mediate the electroweak interactions between leptons and quarks. They are the photon (γ) and the heavy bosons (W^+ , Z^0 , W^-). In particular, the photon and the Z^0 are “mixed”. Through the “spontaneous local symmetry breaking” mechanism by a Higgs doublet [13] the W^+ , W^- , and Z^0 acquire heavy masses while the real photon remains massless.

The quark-quark interactions are mediated by eight colored gluons. They are the quanta identified with massless fields in the Yang-Mills field theory, and were observed in electron-positron collisions [14]. The theory of strong interactions involving the colored gluons has been named QCD (quantum chromodynamics), which today is generally regarded as the most viable theory of strong interactions.

In QED (quantum electrodynamics) charged particles interact with each other through the exchange of virtual photons, γ^* , representing the long-range Coulomb force. In the virtual process of vacuum polarization the γ^* converts for a brief period of time into a virtual lepton-antilepton pair (e^+e^- , $\mu^+\mu^-$, $\tau^+\tau^-$), which then acts as a charge cloud to shield the unmeasurable “bare” charge and make the observed charge finite. In contrast, the gluons of QCD have an opposite effect. Inside the hadron the partons (henceforth the name parton is meant to include quarks, gluons, and virtual photons) are “asymptotically free” [15] which makes perturbative calculations possible in terms of a strong interaction coupling constant, $\alpha_s < 1$. Moving partons to the outside of the hadron requires an enormous amount of energy because the color force represented by the gluon follows a “Hooke’s Law”. The dielectric “medium” created by the virtual parton pairs has an “anti-shielding” effect. Therefore, the gluon-quark coupling constant observed in the real world is greater than that inside the hadron. As a result, no free parton has ever been experimentally observed. All particles crossing the boundary of the hadron “bag” [16] into the outside world must fragment into known particles.

The application of QCD to the quark-parton model for DIS added the effect of gluons in analogy to the effect of photons in QED. The specific theory of GLAP [17] predicted the pattern of deviation from Bjorken’s scaling law [8]. That is, in the low- x region ($x \lesssim 0.2$) the nucleon structure function (see Appendix A.2) would increase as the Q^2 value increases (Q^2 is the negative of the square of the four-momentum transferred to the proton - see Appendix B), but in the higher x region the structure function would decrease. These trends are in good agreement with many observa-

tions in deep inelastic lepton-nucleon scattering, where the lepton beams have included electrons, positrons, muons of both charge, neutrinos, and antineutrinos. The maximum value of Q^2 reached in these experiments was approximately 400 GeV^2 .

In all previous lepton-nucleon DIS experiments the final state hadrons were not thoroughly investigated, mostly due to incomplete solid angle coverage, or the lack of apparatus for measurements of neutral particles. The study of the final state hadrons is particularly interesting. The square of the four-momentum transfer to the initial state proton is calculated by the following formula: $Q^2 \equiv |\vec{p}_{\gamma^*}|^2 - E_{\gamma^*}^2$, where \vec{p}_{γ^*} and E_{γ^*} are the three-momentum and energy of the exchanged virtual photon, respectively. If the Q^2 value is very high the virtual photon carries a much larger three-momentum, $|\vec{p}_{\gamma^*}|$, as compared to its energy and thus has an energy deficiency. It is ineffective in producing new particles, but is effective in giving a parton target a “violent” impulse. The first property could simplify the experimental detection, and the latter property should help to reveal the quark confinement and fragmentation mechanisms.

The kinematic space available at HERA, the electron-proton collider presently producing $26.7 \text{ GeV} \times 819.9 \text{ GeV}$ collisions, is much larger than available to previous experiments. For example, with lines of constant x superimposed, Figure 1 shows the (Q^2, ν) space available at HERA, which is 290 times greater in each dimension than previously explored. (The variable ν is the energy transfer to the proton in its rest frame - see Appendix B.) In Figure 2 the kinematic range in (Q^2, x) space available at HERA is shown, where lines of constant scattered electron energy and angle are drawn as well.

Hadron distributions are usually studied in pseudorapidity space, a variable which originated in cosmic ray experiments. All pseudorapidity distributions observed thus far have been continuous. Bjorken first suggested [18] that gaps might exist in the pseudorapidity distribution of the final state hadrons in deep inelastic electron-proton scattering. HERA, because of its high energy, is an excellent ma-

chine for studying this proposed phenomenon. HERA presently provides a center-of-mass energy squared (s) of 87,565 GeV², which admits a range of pseudorapidity of 11.4 units. This is wide enough to investigate the existence of a rapidity gap several units in width.

This dissertation will begin by detailing the experiment in which observations of electron-proton interactions at HERA were made, including the experimental apparatus used, and the data-taking and data selection procedures. Radiative corrections, corrections for inefficiencies in the data selection, detector acceptances, and any Monte Carlo simulations used for their calculation will be explained. Having made all necessary corrections to the experimental data and converting them into cross section forms, the physics results will commence with a presentation of rapidity distributions of the final state hadrons using the direction of travel of the virtual photon as the reference direction. In events where the final state hadronic mass, W , is large two peaks in this distribution will be revealed. One peak lies along the virtual photon direction, indicating those products arise from fragmentation of the virtual photon, and the other opposite to it, indicating those products arise from fragmentation of the proton. Thus it will be possible to reliably separate the products of virtual photon fragmentation from the products of proton fragmentation, and this procedure will be introduced. The distributions over kinematic variables of interest of events where virtual photon fragmentation occurs will be presented and the properties of the virtual photon fragmentation system will be examined. A new class of events in which only virtual photon fragmentation and no proton fragmentation occurs will be observed. The rapidity distribution of the hadrons in these events is thus discontinuous, containing a gap of over four units in width. The distributions of these events will be presented as well. This dissertation will conclude with a discussion of possible interpretations of the physics results contained herein using as a framework the current model of hadron structure.

Chapter 2

Experimental Apparatus

2.1 The Electron-Proton Collider HERA

The electron-proton collider HERA consists of two accelerator/storage rings, one for protons and one for electrons. An aerial view of HERA and the injection scheme is given in Figure 3. There are four beam interaction regions. The ZEUS experiment is located at the southern interaction region.

HERA consists of 4 straight sections of length 360 m separated by 4 quarter-circle sections of radius 779 m. The maximum collision rate between bunches of electrons and bunches of protons is 10.417 MHz, or one collision every 96 ns. A maximum of 210 bunches of both electrons and protons can be stored. HERA has a design luminosity of $1.5 \times 10^{31} \text{ cm}^{-2}\text{s}^{-1}$. Tables 1 and 2 list the important parameters of HERA [19].

The vacuum pipes for the beams have an average internal pressure of approximately 0.5×10^{-9} torr; hence, there are still gas molecules remaining with which either beam may interact. The rate of these interactions was studied by circulating unpaired “pilot” bunches of protons and electrons during data-taking.

2.2 The ZEUS Detector

Figures 4, 5, and 6 show the ZEUS detector and identify by their acronyms its main components. Not shown are a luminosity monitoring system downstream of the main detector along the electron direction and a leading proton spectrometer downstream of the main detector along the proton direction.

The calorimetry, consisting of the forward, barrel, rear, and backing calorimeters, provides energy measurements of charged and neutral particles. The tracking system, consisting of the vertex detector, central tracking detector, forward tracking detector, rear tracking detector, transition radiation detector, and solenoidal magnet, provides momentum measurements and identification of charged particles. The outer periphery of the ZEUS detector is instrumented with an iron magnet and wire chambers for muon detection. The rate of electron-proton interactions is determined by the luminosity monitoring system. The leading proton spectrometer tags protons which scatter elastically at small angles and would otherwise escape the main detector.

The physics analysis contained in this dissertation is based on data taken with the ZEUS detector during its first two running periods, which occurred during 1992 and 1993. Most of this analysis relies on data from the calorimeter. Therefore, in the following section a detailed description of the calorimeter will be given, including its requirements, mechanical construction, readout, test, and calibration. A cursory description of the tracking system, muon detection system, and luminosity monitor will also be given, including their main parameters and resolutions.

2.2.1 Calorimeter

2.2.1.1 Requirements of the Calorimeter

In electron-proton collisions at HERA, in addition to the scattered electron, the final state may contain numerous hadrons which are distributed over the full 4π

steradians of solid angle. In order to extract the physics content from the data it is necessary to measure as completely as possible the energies of the particles produced in these collisions. The energy measurement of the scattered electron is especially important, for a full reconstruction of the event kinematics relies on it.

The calorimeter serves the purpose of measuring the energies of both charged and neutral particles. The momentum of charged particles can in fact be measured using a tracking chamber in a magnetic field. However, above energies of 50 GeV the energy resolution of a calorimeter is significantly better than the momentum resolution of a tracking chamber. Since particle energies in collisions at HERA can extend up to 820 GeV it is therefore essential that a calorimeter be employed for energy measurements.

Bearing in mind the characteristics of the collisions to be encountered in the ZEUS experiment at HERA, the calorimeter was built to fulfill several requirements:

- Ability to measure the energies of single particles and jets precisely, i.e., good energy resolution;
- Segmentation finer than the typical shower size, i.e.,

$$\sqrt{(\Delta\eta)^2 + (\Delta\phi)^2} < 0.7,$$

where $\Delta\eta$ is the segmentation in pseudorapidity space and $\Delta\phi$ is the segmentation in azimuthal space; this is because the typical radius of a hadronic shower in pseudorapidity-phi space is 0.7;

- Helps to discriminate between electromagnetic showers and hadronic showers;
- Ability to take data at the maximum collision rate at HERA (10.417 MHz);
- Coverage of nearly 4π steradians of solid angle, allowing holes only for the beam pipes and cables;

- Identical calibration curves for electromagnetic and hadronic showers;
- A linear energy calibration over the whole dynamic range.

The fact that the ZEUS calorimeter meets all these requirements makes it an invaluable tool for physics measurements at HERA.

2.2.1.2 Physics of Calorimetry and Compensation

The operation of a calorimeter is founded upon the interactions of radiation with matter. A particle entering the calorimeter media will create a cascade or “shower” of new particles which travels longitudinally and transversely to the direction of the incident particle. Each charged particle in the shower loses energy by the ionization process. Eventually, if the calorimeter is thick enough, all the energy of the incident particle will be absorbed and the shower completely contained.

A calorimeter takes its name from the fact that measuring the energies of incident particles is analogous to the determination of the thermal energy of a heat-bath by the measurement of its temperature. In a calorimeter the shower created by an incident particle is measured or “sampled” at various stages in its development by interleaving layers of detector material with layers of absorber material in a regular pattern. The detector layers are used to measure the ionization which is produced in them. The total ionization produced in all detector planes, which can also be called the “response” of the calorimeter, is a measure of the total energy of the shower.

In practice, a calorimeter is calibrated by measuring its response to single incident particles of various energies. Due to the random nature of the processes involved in the creation of a shower and of the sampling procedure the calorimeter will exhibit a distribution of responses about a mean response at each energy. The width of this distribution represents the energy resolution of the calorimeter.

There are basically two different types of showers: the electromagnetic shower and the hadronic shower. The physics principles governing the development of elec-

tromagnetic showers are quite different from those governing the development of hadronic showers. The remainder of this section is devoted to explaining these physics principles and the main features of these two types of showers. The characteristics of energy measurements by calorimeters of electromagnetic and hadronic showers will also be discussed.

(1) The Electromagnetic Shower

An electromagnetic shower is initiated upon the entrance of either an electron, positron, or photon into a medium. From the observation of the ensuing shower alone it is impossible to discern by which particle an electromagnetic shower has been created. The shower itself is composed of numerous electrons, positrons, and photons, each having been produced by one of several fundamental interactions. For the electrons and positrons in the shower these interactions are bremsstrahlung, the ionization process, and Čerenkov radiation. For the photons in the shower these interactions are electron-positron pair production, Compton scattering, and the photoelectric effect. These electromagnetic interactions have large cross sections. As a result, at any given depth the number of particles with energy greater than some threshold value is large.

The electromagnetic shower has been studied extensively by Rossi [20] and many others, and can be modelled fairly accurately by Monte Carlo programs, such as the EGS4 [21] program by Nelson *et al.* An important result of such studies is the quantitative calculation of the function $\Pi(E_0, E, t)$, which is the number of electrons of energy greater than E in a shower initiated by a particle of energy E_0 , as a function of the depth, t , in the absorber. The natural unit of length for use in such descriptions of the electromagnetic shower is the “radiation length” (r.l.). This is defined [22] as the ratio of the incident energy to the average energy loss per unit length of a high energy electron traversing a medium. The absorber material most widely used in the construction of electromagnetic calorimeters is lead (Pb), for which $1 \text{ r.l.} = 5.6 \text{ mm}$.

In an electromagnetic shower the energy deposition per unit length increases rapidly up to approximately the fifth radiation length, the location about which the largest fraction of the total shower energy is deposited. After the fifth radiation length the energy deposition per unit length decreases more slowly than it increased up to the fifth radiation length. The electrons and positrons in the shower eventually lose all their energy through the ionization process. The photons in the shower eventually lose all their energy through Compton scattering and absorption by the photoelectric effect. An electromagnetic shower will be completely absorbed over a distance of 22 to 25 r.l. This phenomenon does not depend on the energy of the initiating particle.

Over the first three radiation lengths the energy deposition of an electromagnetic shower is considerably larger than that of a minimum ionizing particle, such as a high energy hadron or muon. By measuring the energy deposition per unit length, dE/dx , at the beginning of the calorimeter this property of the electromagnetic shower can be used to distinguish between electrons and hadrons. With this technique a small probability of misidentification still exists, since a π^- can participate in the charge exchange process, $\pi^- p \rightarrow \pi^0 n$, in which the produced π^0 decays into two photons. These photons initiate an electromagnetic shower, producing a signal identical to that of an electron.

Due to the large number of particles created in an electromagnetic shower, the energy deposition per unit length of the shower will be very well defined. Accordingly, the statistical fluctuations in the sampling of the shower will be small. Therefore, the energy resolution of a calorimeter for electromagnetic showers will be relatively good. A typical sampling calorimeter, made of Pb absorber and scintillator detector layers, has an energy resolution for electromagnetic showers, σ_E , of $\sigma_E/E = 18\%/\sqrt{E}$ or better, where E is the energy of the incident particle in GeV.

(2) The Hadronic Shower

A hadronic shower is initiated by a high energy hadron passing through matter. The shower itself consists of an array of particles: protons, neutrons, pions, and kaons among others. These particles originate in the nuclear interactions, which, along with ionization energy loss, are the fundamental processes governing the development of hadronic showers. The charged particles produced in the nuclear interactions lose energy by ionization of the media. Neutral pions produced in the nuclear interactions decay with a lifetime of approximately 10^{-16} sec. into two photons, which initiate an electromagnetic shower internal to the hadronic shower.

The nuclear interactions have relatively small cross sections; therefore, the number of particles produced and the rate of particle multiplication in hadronic showers is small, especially in comparison with electromagnetic showers. Thus, the amount of material required for complete absorption of a hadronic shower is much greater than required for complete absorption of an electromagnetic shower.

The natural unit of length for use in the description of the hadronic shower is the “interaction length” (λ). This is defined as the mean free path between inelastic collisions in the medium [23]. Typically, in a given medium $1 \lambda \approx 25$ r.l., reflecting the large difference in the magnitude of the electromagnetic interaction cross sections in comparison with the nuclear interaction cross sections.

Because the number of particles produced in hadronic showers is smaller than the number produced in electromagnetic showers the statistical fluctuations in the sampling of a hadronic shower will be greater than those in the sampling of an electromagnetic shower. Thus, the calorimeter energy resolution for hadronic showers will be worse than that for electromagnetic showers. A typical energy resolution for hadronic showers, σ_E , of a calorimeter with steel absorber and scintillator detector layers is $\sigma_E/E = 80\%/\sqrt{E}$, where E is the energy of the incident hadron in GeV.

Typically, the response of a calorimeter to a hadronic shower, denoted h , will be less than the response to an electromagnetic shower of the same energy, denoted e , i.e., $e/h > 1$. This again is due to the difference in the number of particles in electromagnetic showers as compared with hadronic showers. The smaller number of particles in hadronic showers means that there will be less ionization in the detector layers, and the response to hadronic showers is therefore lower. Thus, sampling calorimeters usually have different calibration curves for electromagnetic showers and hadronic showers, unless appropriate measures are taken to make them identical.

This property of sampling calorimeters is particularly troublesome in the measurement of jet energies. It is well established that up to approximately 15% of the particles in the jets which appear in the final state hadronic system in deep inelastic scattering could be neutral. In particular, the π^0 constituents of the jets decay into two photons, which then initiate electromagnetic showers in the calorimeter. If these electromagnetic showers are wrongly assumed to be hadronic showers then the measurement of the apparent jet energy will be higher than the true energy.

It is thus of benefit to construct a calorimeter which has the same response to electromagnetic showers as to hadronic showers, i.e., $e/h = 1$. This act is referred to as “compensation”. Incidentally, compensated calorimeters also have the best energy resolution for hadronic showers; however, this is bought at the expense of a slightly worse energy resolution for electromagnetic showers relative to that which is practically attainable.

Calorimeter compensation can be achieved by taking two measures: (1) addition of energy to the calorimeter and (2) suppression of the calorimeter response to electromagnetic showers. Brückmann *et al.* showed that both could be achieved simultaneously by using depleted uranium (DU) as an absorber layer and scintillator as a detector layer [24]. This was done on the basis of quantitative Monte Carlo calculations using the EGS4 package for electromagnetic showers and codes

developed at Oak Ridge National Laboratory (ORNL) for hadronic interactions, neutron transport, and gamma transport. Brückmann *et al.* also incorporated a time development of the neutron induced processes.

In DU, fission of the uranium content can occur as part of hadronic showers. The fission of the ^{238}U in DU can be accomplished by neutrons with energy greater than about 1 MeV, while the fission of the ^{235}U can be accomplished by lower energy thermal neutrons. The fission process in hadronic showers is not important in absorber materials other than DU. When a uranium nucleus undergoes fission, binding energy is released. Some of this binding energy appears as kinetic energy of the neutrons which are produced.

Another important process available in DU is the neutron capture process. In this process a slow neutron is absorbed by a nucleus. The excited state formed when this happens decays by the emission of a photon. The photon is detected by Compton scattering and the photoelectric effect in the detector layers.

Brückmann *et al.* realized that a calorimeter detector layer capable of converting neutron energy into ionization energy loss is necessary to take advantage of the energy released to the neutrons by fission. This is most readily accomplished by a detector layer copious in hydrogen. In a detector layer with this property the neutrons will very rapidly transfer all their energy by elastic collisions to the protons of the hydrogen. The recoiling protons then produce the ionization of the detector layer. The need for a detector layer in which the protons can recoil to produce ionization rules out the use of liquid argon, since it has more neutrons than protons in its nucleus, and makes hydrogen-rich scintillator the detector layer of choice.

However, neither ionization in the detector layers by proton recoil nor detection of photons from neutron capture is prompt. Both processes, fission and neutron capture, take a finite amount of time. Hence, their products do not appear in the detector layers until some time after the main part of the hadronic shower has passed through. Brückmann *et al.* calculated the contribution to the calorimeter

response from both proton recoil and neutron capture. These contributions are shown in Figure 7, where the energy visible in the detector layers due to proton recoil and neutron capture versus time are plotted. This result illustrates that to take advantage of the energy released in these two processes the calorimeter signal must be integrated over time, and that the degree of compensation is a function of the gate width.

Having illustrated that the energy released by the DU could indeed be detected, Brückmann *et al.* proceeded to show how the calorimeter response could be tuned for compensation. This was shown to be feasible by adjusting the ratio of the thickness of the absorber layer to the thickness of the detector layer. For a fixed scintillator thickness, increasing the absorber thickness has the effect of causing showers to lose a greater amount of energy in the passive absorber layers. This has a significant effect on electromagnetic showers, since they have such a large number of particles. The effect of increasing the absorber thickness is to suppress the calorimeter response to electromagnetic showers. Cladding of the DU plates and wrapping of the scintillator tiles also play a role in compensation.

Figure 8 illustrates how compensation varies with the ratio of absorber layer thickness to detector layer thickness. In this figure the degree of compensation is plotted versus the ratio of DU thickness to scintillator thickness for scintillator layers 2.5 mm and 5.0 mm in thickness. The region in which full compensation is achieved is illustrated, as are the regions of undercompensation and overcompensation.

The ZEUS calorimeter was designed on the basis of these careful calculations of Brückmann *et al.* The final design called for the use of 3.3 mm DU plates clad in 0.2 mm stainless steel sheets and 2.6 mm thick scintillator layers. Test results verified the compensation of the calorimeter with these parameters.

2.2.1.3 Mechanical Construction and Readout

The ZEUS calorimeter is composed of three main sections. The forward calorimeter (FCAL) provides coverage of the polar angles $2.2^\circ < \theta < 39.9^\circ$, the barrel calorimeter (BCAL) provides coverage of the polar angles $36.7^\circ < \theta < 129.1^\circ$, and the rear calorimeter (RCAL) provides coverage of the polar angles $128.1^\circ < \theta < 176.5^\circ$. In this description the proton direction is along the z -axis, the electron direction is along the $-z$ -axis, the x -axis points towards the center of HERA, and the y -axis completes a right-handed coordinate system.

The FCAL and RCAL are composed of “towers” in the shape of rectangular blocks whose long axes lie parallel to the z -axis. Each tower consists of an electromagnetic (EMC) section 25 r.l. long followed by one (in RCAL) or two (in FCAL) hadronic (HAC) sections each of length 3.1λ . In the transverse dimensions each tower is $20 \text{ cm} \times 20 \text{ cm}$ square. Figure 9 shows a cross sectional view through an FCAL tower. The EMC section of the FCAL (FEMC) towers is divided into four smaller cells of transverse dimension $20 \text{ cm} \times 5 \text{ cm}$, while the EMC section of the RCAL (REMC) towers is divided into two smaller cells of transverse dimension $20 \text{ cm} \times 5 \text{ cm}$. Figure 10 is a cut-away view of a FCAL module, which consists of 23 stacked towers. Figures 11 and 12 are views of the FCAL and RCAL, respectively, as seen from the interaction point.

The BCAL is in the shape of an annulus. It is divided into 32 modules each covering 11.25° around the azimuth. A cut-away view of a single BCAL module is shown in Figure 13. Each BCAL module consists of 14 towers whose long axes lie along the radius. Each tower consists of an EMC section (BEMC) extending 25 r.l. along the radius followed by two hadronic sections (BHAC1 and BHAC2) each extending 2.1λ along the radius. A cross sectional view through a BCAL tower is shown in Figure 14. The BEMC section is divided into four cells with front face dimensions of $24 \text{ cm} \times 5 \text{ cm}$. The BEMC cells are “projective”, that is, they would point towards the nominal interaction point. However, all BCAL modules are

tilted by 2.5° to ensure that particles coming from the interaction point cannot travel through the intermodular cracks and hence escape detection by the calorimeter.

Figures 9, 10, 13 and 14, to which we refer throughout the remainder of this section, illustrate the basic construction of the calorimeter. As shown, the calorimeter is constructed by interleaving 3.3 mm thick DU plates with 2.6 mm thick scintillator tiles. Each DU plate is covered by a 0.2 mm thick stainless steel sheet which reduces the exposure of the scintillator to the radioactivity of the DU. The scintillator tiles are covered by a layer of reflective wrapping on which a pattern is printed. The pattern is darker at the outside edges of the tiles and lighter near the center. This ensures that the magnitude of the attenuation of all light propagating in the scintillator is the same, regardless of the location of its origin in the scintillator, and thus provides for a uniform light yield.

There is extra space in the EMC sections of the calorimeter to provide for a hadron-electron separation system. Including the thickness of the inactive material intervening between the interaction point and the calorimeter, the location of the extra space for the hadron-electron separation system is at a depth of approximately five r.l. from the nominal interaction point. This being the location of the shower maximum of an electromagnetic shower, one should expect a much larger signal there from electromagnetic showers as compared to hadronic showers. However, π^- particles traversing the five r.l. of material between the interaction point and the location of the hadron-electron separation system have a good chance of undergoing the charge exchange process. The two photons coming from the decay of the produced π^0 cause an electromagnetic shower, which mimics the signal of an incident electron. Unfortunately, this phenomenon makes using a hadron-electron separation system at this location difficult in practice. Hadron-electron separation can be better done over the first three radiation lengths. However, a detector at five radiation lengths can be useful for measuring the position of the shower maximum of electromagnetic showers.

For the 1992 and 1993 data-taking only part of the RCAL close to the beam pipe was fitted with a hadron-electron separation system, forming the RHES (RCAL hadron-electron separation) system. The RHES is composed of silicon diode detectors, each of dimension $3\text{ cm} \times 3\text{ cm}$. The silicon diodes are pn junctions operated in reverse bias (up to ≈ 60 volts). For every 3.62 eV of energy deposited by a particle in the ion-free “depletion” layer an ion-hole pair is created. The charges of the ions are collected and sent into a charge sensitive amplifier in order to produce a voltage signal. The subsequent processing of the signal is similar to that of the calorimeter. Since a large number of ion-hole pairs are produced during the traversal of the diode by a high energy particle, the good statistics makes the silicon detector sensitive and it gives a good energy resolution.

Although not extensively used for hadron-electron separation during the 1992 and 1993 data-taking periods, the RHES did prove valuable for obtaining improved position measurements of the shower maximum of electromagnetic showers in the calorimeter. This is because the silicon diodes of the RHES are smaller in area than the calorimeter cells and therefore provide better resolution for position measurement.

Wavelength shifter (WLS) bars are placed perpendicular to the scintillator tiles on both sides of the calorimeter towers. They are separated from the scintillator tiles by a small air gap. The WLS bars absorb photons emitted in the scintillator tiles and re-emit photons of a different wavelength. Since the index of refraction of the WLS bars is greater than that of air, the photons emitted by the WLS material can travel inside the bars by total internal reflection. The reason for reading out each cell on two sides is to allow for a rough position measurement of the location of the maximum energy deposition of a shower. The location of the maximum energy deposition of a shower is usually calculated as the energy-weighted mean of the shower “positions” in all cells over which the shower spreads. Without using readout of both sides of the cell, the shower position in each cell would be taken as

the position of the center of the cell. However, with readout of both sides of the cell the shower position in each cell can be taken to be closer to the side having the greater energy deposition.

Readout of both sides of the cell also allows for redundancy, since if one of the channels is dead for some reason the cell can still be read out. During data-taking, in the case that one channel of a given cell was dead the total energy in the cell was assigned to be twice the amount of energy in the good channel.

The WLS bars, like the scintillator tiles, are wrapped in reflective paper having a printed pattern to achieve spatial uniformity of response. The pattern ensures that light traveling longer distances will suffer roughly the same amount of attenuation as light traveling shorter distances.

If a charged particle happens to travel along a WLS bar, the Čerenkov radiation produced will falsely enhance the energy measured by the calorimeter. This effect was observed to be as large as approximately 15%, and several measures were taken to remove it. In the case of BCAL, where each module is tilted by 2.5° , 1.6 mm of lead sheets and 0.8 mm of stainless steel sheets were inserted into each intermodule space. In the case of FCAL and RCAL, 2.6 mm of lead sheets and 0.5 mm of stainless steel sheets were placed into each intermodule space. These measures combined to improve the energy measurement uniformity to approximately the 1% level.

The end of the WLS bar is connected to a light guide. The light guide in turn connects to a cylindrical transition piece, or “cookie”, which couples the light guide to the front face of a photomultiplier tube (PMT) and disperses light uniformly over its face. Photons traveling the length of the WLS bar strike the photocathode of the PMT and eject electrons from it via the photoelectric effect. The ZEUS experiment uses the R580 PMT, made by Hamamatsu, which is a ten stage tube. Starting from the photocathode, which is at negative high voltage, each successive dynode of the PMT is at a higher voltage than the previous one. The electrons ejected from the photocathode are thus accelerated to the first dynode, where they eject two or three

new electrons. The ejected electrons are accelerated to the next dynode, where in turn they each eject two or three new electrons. This process is repeated over all ten stages. The number of electrons initially ejected from the photocathode is thus amplified by a factor of about 10^5 .

The gain, G , of the PMT is the number of electrons arriving at the anode of the PMT, which is at high voltage, per photoelectron liberated at the photocathode. It was empirically determined that the PMT gain could be related to the applied voltage, V , by the formula $G = (V/V_0)^a$, where V_0 and a are constants, and $a \approx 7.5$. Individual Cockcroft-Walton type bases [25] supply the high voltages to the dynodes and cathode of each PMT.

Electrical signals coming from the PMT anode travel to the readout electronics [26], where a four-way split of the current occurs. Part of the current is sent through a uranium signal integration channel. This channel integrates the current through it over 20 msec and is used for calibration purposes. Part of the current is sent through a low gain amplifier channel. This channel is used to measure the energies of electromagnetic and hadronic showers in the detector. Part of the current is sent through a high gain amplifier channel, which is used for calibration purposes for the measurement of energy deposited by muons. Lastly, part of the current is sent through the trigger channel, where it is attenuated and added to the signals of other channels to form energy sums in each calorimeter “tower”.

In the low and high gain channels the signal is stretched so that it spreads over a time interval of 500 nsec. With the pulse stretched, its voltage is sampled at several points in time. The samples are placed into a switching capacitor pipeline pending the decision of the trigger electronics. The switching capacitor pipeline consists of an array of capacitors multiplexed to a common input line. During the write cycle, one-by-one the voltage samples are placed on the input line. A clock pulse closes the switch connecting a capacitor to the input line. The capacitor is charged to the input voltage for a fixed time interval and the switch reopened. Each capacitor

holds one sample; thus, each event is stored on several capacitors. There are enough capacitors to allow more than one event to be stored.

While the samples are stored in the analog pipeline the trigger electronics decides whether or not the event should be retained for further processing. The decision is based on event characteristics such as total energy or total transverse energy in the calorimeter. The trigger logic will be discussed in section 3.2.3.

All the capacitors in the switching capacitor pipeline are also multiplexed to a common ADC (analog-to-digital converter). If a trigger is issued the event is read out by connecting the capacitors one at a time to the ADC for digitization of the voltage. After correcting for ADC pedestal, the energy and time of the signal are computed from the samples by a signal processor. If a trigger is not issued then the event is cleared from the pipeline by discharging the capacitors to ground.

2.2.1.4 Test Results and Calibration

A number of calorimeter modules were tested by placing them in high energy beams of electrons, pions and muons [27, 28]. In addition, 22 BCAL modules underwent similar tests with cosmic ray muons [29]. The purpose of these tests was to calibrate the calorimeter energy scale, to measure the energy resolutions, and to confirm the compensating nature of the calorimeter. The important results of these beam tests follow.

- **Calibration and Compensation**

The calibration curve with respect to particle energy was determined. Inactive material was placed in front of the calorimeters to simulate the ZEUS experimental environment and the calorimeter response recorded under these conditions. All three calorimeters, FCAL, BCAL, and RCAL were found to have identical calibration curves for electrons and pions. For the FCAL, e/h was measured to be 1.00 ± 0.01 . For the BCAL, e/h was measured to be 1.00 ± 0.03 .

- Energy Resolution, σ_E

For the BCAL, the electromagnetic energy resolution was found to be $\sigma_E/E = (19.0 \pm 1.7)\%/\sqrt{E}$ and the hadronic energy resolution was found to be $\sigma_E/E = 35\%/\sqrt{E}$, where E is the energy of the electron or hadron in GeV.

For the FCAL, the electromagnetic energy resolution was found to be $\sigma_E/E = 17.6\%/\sqrt{E}$, where E is the energy of the electron in GeV. From tests of a prototype module, the hadronic energy resolution was found to be $\sigma_E/E = (35.0 \pm 0.3)\%/\sqrt{E}$, where E is the energy of the hadron in GeV.

For the RCAL, the electromagnetic energy resolution was found to be $\sigma_E/E = 17.4\%/\sqrt{E}$, where E is the energy of the electron in GeV. For hadrons the energy resolution was also found to be $\sigma_E/E = 35\%/\sqrt{E}$, where E is the energy of the hadron in GeV.

- Linearity

The calibration curve for FCAL and BCAL was found to be linear within 1% and the calibration curve for RCAL to within 2% for electrons with energies up to 75 GeV.

2.2.1.5 The DU Signal

The heavy elements of which DU is composed decay into lighter elements via the emission of α particles, electrons, and photons. There are many hundreds of decay chains which can occur. The lifetimes of all these elements are very long relative to the time over which the ZEUS experiment is run. Therefore, the number of decays per second can be regarded as constant.

In the DU absorber plates of the ZEUS calorimeter the α particles emitted are stopped within the plates themselves, since the range of α particles in DU is typically 7 μm . Any α particles emitted near the surface of the plates are stopped by the 2 mm thick stainless steel sheet covering each plate. The electrons and photons, on the other hand, emanate from the plates and pass into the scintillator. The electrons

produce scintillation light by ionizing the scintillator and the photons produce light via Compton scattering or the photoelectric effect.

The amount of scintillation light produced by decay particles passing through the scintillator is large enough that it is detected as an electrical signal from the PMT. Integrating this signal over a period of time measures the total number of electrons at the anode of the PMT over the integration period. Since the number of decays per second is constant, the number of photons striking the photocathode of the PMT per second is also constant. Thus, measuring the number of electrons at the anode of the PMT by integrating the DU signal measures the gain of the PMT.

A nominal gain is defined for each channel of the calorimeter. It depends on the size of the calorimeter cell, since larger cells subtend larger amounts of DU and therefore larger decay signals will be detected in them. Each channel of the calorimeter can be calibrated by comparing the gain determined by integrating the DU decay signal with the nominal value of the gain for that channel. The integration is performed over a 20 msec time interval. The high voltage applied to the PMT can then be adjusted in order to make the measured gain for the channel match the nominal gain. Calibration of the channel gain by using the DU signal in this manner has been a very important calibration tool for the ZEUS calorimeter.

The presence of the DU signal has two unfortunate disadvantages. First, due to the random nature of the decay process, during data-taking it is possible to obtain a false low energy signal in a given channel from DU decay. This inconvenience was handled by placing an energy threshold on all calorimeter cells at the start of event reconstruction. The energy thresholds used were 60 MeV for EMC cells and 110 MeV for HAC cells. Second, the stability of the DU signal means that the scintillator is constantly being ionized and the cathode of the PMT is constantly producing current. This contributes to the aging of the scintillator, photocathode, and dynodes resulting in a loss of gain over time.

2.2.2 Tracking Systems

The inner parts of ZEUS are instrumented with detectors capable of measuring the tracks of charged particles emerging from an electron-proton interaction. These detectors are the vertex detector (VXD), the central tracking detector (CTD), the forward (FTD) and rear (RTD) tracking detectors, and the transition radiation detector (TRD). A superconducting solenoid provides a magnetic field over the major part of the tracking system.

For the 1992-93 experimental runs the FTD, TRD, and RTD were not operational; therefore, the CTD and VXD are the only elements of the tracking system used in the physics analysis which follows. Their primary use for the analysis contained in this dissertation was for determination of the event vertex.

2.2.2.1 Central Tracking Detector (CTD)

The main part of the tracking system is the CTD, which is 205 cm long ($z = -100$ cm to $z = 105$ cm) and extends outward from the z -axis between the radii 16.2 cm and 85 cm. The CTD is a cylindrical wire drift chamber consisting of 9 superlayers. Five of the superlayers have wires strung parallel to the z -axis (axial wires) and four of the superlayers have wires strung at a pitch of $\pm 5^\circ$ to the z -axis (stereo wires). Each superlayer is divided into many cells. The innermost layer has 32 cells, and the outermost layer has 96 cells. Each cell is eight sense wires thick.

Figure 15 is an end view through one octant of the CTD. In this figure the thick dots represent the sense wires of the CTD, which are used to record the signals. They are at high voltage in order to attract electrons produced by the ionization process in the chamber. The sense wires are read out on one end by FADC's (flash ADC's), which are ADC's operating at 104 MHz. The sense wires in superlayer one and part of superlayers three and five are also read out on both ends by TDC's (time-to-digital converters). The thin dots in Figure 15 represent the field wires of the CTD, which are used to shape the electrostatic field within the volume of the CTD.

The chamber is filled with a gas mixture of 90.8% argon, 7.1% carbon dioxide, and 2.1% ethane. Charged particles traversing the chamber ionize this gas. As the electrons liberated in the ionization process drift towards the sense wires they in turn ionize other gas molecules, thus amplifying the number of electrons approaching the wire. The electrostatic field in the chamber is perpendicular to the magnetic field of the superconducting solenoid (which points in the $+z$ direction). This causes a Lorentz force to act on the drifting electrons, thus rotating their trajectories by an angle with respect to the direction of the electrostatic field. In the CTD this angle was designed to be 45° , based on the strength of the electrostatic and magnetic fields and the electron drift velocity in the gas. To optimize the spatial resolution of the CTD the sense wires are tilted by this same angle, as seen in Figure 15. This ensures that the electron drift trajectory is almost perpendicular to the sense wires.

The electrons arriving at a sense wire cause a negative signal to be produced. The FADC for the sense wire digitizes the voltage on the wire every 9.6 nsec. A digital signal processor is used to reconstruct the arrival time and pulse height of the signal. The time of arrival of the signal is measured with respect to an artificial time, “ t_0 ”, for the wire. The chamber is calibrated so that the difference between the signal arrival time and the reference time t_0 is a measure of the track position with respect to the wire.

The axial wires read out by FADC’s provide only the r - ϕ positions of traversing particles. The current position resolution in the r - ϕ plane is $260\ \mu\text{m}$, but this should improve to the design resolution of $100\text{-}140\ \mu\text{m}$ as data-taking experience increases. The stereo wire readout is used to determine the z position of the traversing particles. This is because the stereo wires cross several axial wires, each at different coordinates in z . If a signal is detected on a stereo wire it is projected back until it crosses an axial wire on which a signal has also been detected. The z position at which the axial and stereo wires cross gives the z position of the traversing particle.

The TDC readout on both ends of the sense wires in layers one, three, and five uses the difference in the arrival time of the signals at both ends of the wires to give z position information in addition to r - ϕ position information. This is done as follows. The arrival of a signal from one end of the wire starts the charging of a capacitor at constant current. The arrival of a signal from the other end of the wire stops the charging of the capacitor. The voltage level on the capacitor is digitized using an FADC. This voltage level is proportional to the time difference between the start and stop signal. This time difference indicates the z position of the signal on the wire. The resolution of this “z-by-timing” system is poorer than the resolution of the FADC readout.

In the plane transverse to the magnetic field, the path taken by a particle appears circular. This knowledge can be used to piece together position information from the wire signals to deduce the tracks of a particles traversing the CTD. The charge of the particle is determined by direction in which the track curves. The momentum of the particle is determined by the radius of curvature of the track. The achieved resolution on particle momentum determination by the CTD is $\sigma_p/p = 0.005p$, where p is the momentum of the particle measured in GeV. The momentum resolution is expected to improve with more data-taking experience to the design resolution of $\sigma_p/p = 0.002p$. The resolution is best at 90° where the particle track is perpendicular to the sense wires, but worsens at large and small polar angles. Particle identification by the CTD can be accomplished by a measurement of the ionization energy loss, $-dE/dx$, of the particle as it traverses the gas volume of the CTD.

2.2.2.2 Superconducting Solenoid

A superconducting solenoidal magnet of inner radius 93 cm and outer radius 95 cm provides an axial field directed along the z -axis of 1.43 T within the volume of the CTD. The magnet is 2.5 m long, extending from $z = -1.2$ m to $z = 1.3$ m. The solenoid is a two-layered structure consisting of 457 windings for the inner layer

and 450 windings for the outer layer. The windings are made of strands of the superconducting material niobium-titanium (Nb-Ti) mixed with copper (Cu). The Cu/Nb-Ti strands are clad in an aluminum (Al) extrusion. The (Cu + Al)/Nb-Ti ratio is 14.6, so the Nb-Ti accounts for 6.4% of the wire structure. If the current in the superconductor becomes larger than the critical value it will undergo a phase transition from the superconducting phase to the normal phase. In the normal phase the superconducting material has a high resistance. When a phase transition like this occurs, the Cu and Al act to stabilize the superconductor by shunting the current out of it. With the current shunted away the superconductor then returns to the superconducting phase. The superconducting windings are cooled to 4.45 K by a cryogenic system using liquid helium. A small magnet located behind the RCAL serves to cancel the field of the solenoid within the confines of the beam pipe so as not to disturb either electron or proton beam.

2.2.2.3 Vertex Detector (VXD)

To measure charged particle tracks close to the interaction point and provide for studies of short-lived particles a vertex detector (VXD) is included in the tracking system. The VXD is a cylindrical wire drift chamber 1.6 m in length extending outward from the z -axis between the radii 9.9 cm and 15.9 cm. It consists of 120 cells, each containing 12 sense wires, of the type shown in Figure 16. The cells are positioned azimuthally around the beam pipe. Dimethyl ether (DME) gas fills the chamber.

2.2.2.4 Forward and Rear Tracking Detectors (FTD, RTD)

Using the CTD, particle tracks can be constructed reliably only between the polar angles, θ , of $15^\circ < \theta < 164^\circ$. This is because the best track measurements are made when the path of the traversing particles is perpendicular to the chamber wires. In order to track particles at more extreme polar angles the forward tracking (FTD)

and rear tracking (RTD) detectors are included in the ZEUS tracking system.

The FTD measures tracks between the polar angles $7.5^\circ < \theta < 28^\circ$, while the RTD measures tracks between the polar angles $160^\circ < \theta < 170^\circ$. The FTD consists of three disk-like planar drift chambers and the RTD consists of one disk-like planar drift chamber. The basic construction of all FTD and RTD drift chambers is essentially the same. They differ only in their spatial dimensions. An example of a F/RTD drift chamber is shown in Figure 17.

Each chamber consists of three layers of drift cells. The wires of the three layers lie at 120° angles with respect to each other. Within each layer the wires lie transverse to the z -axis. Each cell is six sense wires deep along the direction of the track. The wires of the cells are staggered by $\pm 150 \mu\text{m}$ in order to resolve the left-right ambiguity posed by traversing tracks. A gas mixture of 50% argon and 50% ethane fills the chambers. The position resolution of the FTD and RTD wire chambers is expected to be 120-130 μm .

2.2.2.5 Transition Radiation Detector (TRD)

Electron-pion separation in the forward region is accomplished by the inclusion of a transition radiation detector (TRD). There are four TRD modules in the forward region. Two are placed between the first and second wire chambers of the FTD and two are placed between the second and third wire chambers of the FTD. Each TRD module consists of a 7 cm thick layer of polypropylene fibers followed by a wire chamber. The wire chamber is filled with a gas mixture of 90% xenon, 8% carbon dioxide, and 2% isobutane. Particles passing through the polypropylene layer will emit transition radiation. The transition radiation photons, which are in the x-ray region, are then detected by their ionization of the gas in the wire chamber.

Transition radiation is produced when a particle crosses the boundary between two materials having different dielectric constants. The number of transition radiation photons produced is proportional to the relativistic γ factor of the particle,

$\gamma \equiv E/m_0$, where E is the energy of the particle and m_0 is the rest mass of the particle. By counting the numbers of transition radiation photons produced the TRD measures the γ factor of the traversing particle. The energy of the particle can be measured by the calorimeter. Combining the γ factor measurement of the TRD with the energy measurement by the calorimeter determines the mass of the traversing particle. Electrons and pions are readily separated by the large difference in their masses.

2.2.3 Veto Wall

The veto wall is a solid iron wall 87 cm in thickness, 800 cm in width, and 907 cm in height. Its purpose is to shield the main detector from stray beam particles and products of upstream interactions of the proton beam with residual gas in the beam pipe. The veto wall is located 7.5 m upstream of the interaction region along the proton direction ($z = -7.5$ m).

Part of the iron wall is covered by a scintillator hodoscope consisting of identical arrays of scintillator counters placed transverse to the z -axis on either side of the wall. The hodoscope covers the area between $-240 \text{ cm} < x < 400 \text{ cm}$ and $-220 \text{ cm} < y < 300 \text{ cm}$. It is triggered whenever signals are detected in one counter and in its corresponding counter on the opposite side of the wall. Triggers are caused by particles which are not completely absorbed in the iron wall. These particles will continue on towards the main detector. Therefore, in order to prevent false event triggers any event which is triggered in the main detector in which the veto wall is also triggered was rejected.

2.2.4 C5 Counter

The C5 counter consists of four scintillation counters positioned immediately behind the RCAL at the position $z = -315$ cm. One pair of scintillation counters is above

the beam pipe and another pair is below. The system measures the arrival time of the stray “halo” particles accompanying the electron and proton beams. The C5 may also be triggered by particles coming from interactions between the proton beam and the residual gas in the beam pipe.

The C5 was used during data-taking in three capacities. First, since the halo particles indicate the times at which the beams are passing, the C5 was used to estimate an average vertex position during data-taking. Second, the rate at which the C5 is triggered was used as a measure of the beam-related background encountered during data-taking. Third, the C5 was used as a veto to prevent false triggers in the main detector from halo particles or products of beam-gas interactions.

2.2.5 Luminosity Monitor

Luminosity is the event rate per unit cross section. In the ZEUS experiment the luminosity was determined by measuring the rate of wide-angle bremsstrahlung events, $e + p \rightarrow e + p + \gamma$, since its cross section is large and can be calculated. The bremsstrahlung events are identified by the final state ($ep\gamma$).

The luminosity monitoring system is shown in Figure 18. The final state photons and electrons are tagged by two lead-scintillator calorimeters. The photon calorimeter is placed at 0° with respect to the electron beam direction 105 m distant from the nominal interaction point. The electron calorimeter is placed at a small angle with respect to the electron beam direction 35 m distant from the nominal interaction point.

The luminosity is found by measuring the rate of wide-angle bremsstrahlung events and dividing this rate by its theoretically calculated cross section, taking care to include all detector acceptances. However, the measured bremsstrahlung rate is not the true rate of bremsstrahlung between electrons and protons in the two beams. This is because the measured rate includes background from interactions of the electron beam with the residual gas in the beam pipe. The electron pilot

bunches were used to correct the measured bremsstrahlung rate for the electron-gas background. This was done according to the formula

$$R_{true} = R_{coll} - \frac{N_{coll}}{N_{pilot}} R_{pilot},$$

where R_{true} is the true bremsstrahlung rate, R_{coll} is the measured bremsstrahlung rate for the colliding bunches, N_{coll} is the total number of particles in all electron colliding bunches, N_{pilot} is the total number of particles in all electron pilot bunches, and R_{pilot} is the measured bremsstrahlung rate for the pilot bunches.

2.2.6 Iron Yoke and Backing Calorimeter

An iron yoke in the shape of an octagonal cylinder and closed by endcaps on either end encloses the ZEUS calorimeter and tracking systems. The yoke returns the magnetic flux of the superconducting solenoid. In addition, copper coils on the endcaps and cylinder are used to generate a toroidal magnetic field of 1.6 T in the yoke. This magnetic field serves as part of the muon detection system. The difference in direction before and after a muon passes through the yoke gives both its charge and momentum.

Wire chambers are inserted into the yoke to form a backing calorimeter (BAC). The purpose of the backing calorimeter is to contain and measure the energy of the tail end of any hadronic shower not fully contained in either the FCAL, BCAL or RCAL. The iron of the yoke serves the purpose of an absorber material while the wire chambers are used as calorimeter detector layers measuring the ionization energy loss of the tail end of the shower.

2.2.7 Muon Detection System

Muons which are produced in electron-proton collisions will generally behave as minimum ionizing particles. The reason for this is that the muon is relatively heavy,

and hence the energy loss due to bremsstrahlung of muons passing through matter is much smaller than that for electrons. Therefore, muons rarely create electromagnetic showers in passing through the calorimeter. If the energy of an outgoing muon is large enough it will pass completely through the calorimeter and its energy will not be completely absorbed. From the calorimeter data alone, such events will appear to possess a missing transverse energy. Tagging outgoing muons and determining their momentum is thus a necessity to ensure proper reconstruction of the event.

Muon pairs can appear in events in which pair production of heavy quarks occurs via photon-gluon fusion. The main purpose of the muon system is to detect the muons in such events. The muon system can also prove valuable in the rejection of events triggered by cosmic ray muons traversing the detector.

The muon detection system is divided into forward (FMUON), barrel (BMUON), and rear (RMUON) subsystems. The FMUON covers the polar angles, θ , between 5° and 32° . Two large toroids are used to produce a toroidal magnetic field of 1.7 T. The magnetic field in the endcap of the iron yoke is also used by the FMUON. On either side of the magnetic fields are placed limited streamer tubes and drift chambers. The streamer tubes are used to trigger on traversing muons. The drift chambers are then used to measure the polar coordinates of the traversing muons. A measurement of the direction of a muon before and after its traversal through the magnetic fields determines both its charge and momentum. The drift chambers of the FMUON are filled with a gas mixture of 90% argon, 9% carbon dioxide, and 1% methane at atmospheric pressure and the limited streamer tubes are filled with a gas mixture of 30% argon and 70% isobutane.

The BMUON covers the polar angles, θ , between 34° and 133° , while the RMUON covers polar angles greater than 133° . The BMUON consists of two layers of limited streamer tubes placed inside and outside of the iron yoke. The tubes are placed parallel to the z -axis. The RMUON also consists of limited streamer tubes inside and outside the iron yoke. The tubes of the RMUON are placed transverse to the

z -axis. A trigger is issued whenever streamer tubes both inside and outside the iron yoke detect signals. The charge and momentum of the muon are then determined by the direction of the muon before and after passing through the magnetic field of the yoke. The limited streamer tubes of the BMUON and RMUON are filled with a gas mixture of 70% C_4H_{10} and 30% argon.

2.2.8 Data Acquisition System

Figure 19 shows the ZEUS data acquisition scheme. At each beam crossing all detector components open an electronic gate, record data, and place the data in an analog pipeline. The switching capacitor analog pipeline of the calorimeter, for instance, was described in detail in section 2.2.1.3. The first level trigger (FLT) electronics of each component performs some elementary determinations of total energy and transverse energy by hardwired electronics and applies decision criteria on whether or not the event is likely to have been caused by an electron-proton interaction. The FLT decision of all components is passed to the global first level trigger (GFLT), which then decides whether or not to retain the event for further processing. Data from events passing the GFLT decision are digitized and moved on to the second level trigger (SLT) of each component, whereas events failing the GFLT decision are cleared from the pipelines.

The number of events processed by the SLT will be much smaller than the number of events processed by the FLT; therefore, more extensive calculations on computers can be performed at the second level. In the SLT further requirements are made of the data to reject background events while retaining events from electron-proton interactions. Each component passes its decision on to the global second level trigger (GSLT), which then, based on the individual component SLT decisions, decides whether to clear the event from the digital buffers or to move the event on to the event builder (EVB).

The EVB collects the data from the digital buffers of all components and combines them to form a single event. The data are organized, placed into the format of the database management package ADAMO [30], and then passed on to the third level trigger (TLT).

The TLT uses global event information from all detector components to decide whether or not to retain each event received from the EVB. As the number of events reaching the TLT is much smaller than the FLT or SLT, the TLT has much more time per event to perform extensive calculations in making its decision. Events surviving the decision criteria of the TLT are then written to mass storage media.

HERA produces bunch crossings at a maximum rate of 10.417 MHz. Typically, the FLT issues triggers at a rate of about 1 kHz. The SLT reduces the rate to about 100 Hz. Finally, the TLT issues triggers and events are written to mass storage media at a rate of 3 to 5 Hz. A run control process starts and stops the data-taking, configures the data-taking setup and which components are included in the run, and monitors the trigger rates and associated dead times of each component.

Once on the mass storage media, offline software programs are run to fully reconstruct the events. Calibration constants and noise suppression thresholds are applied, extensive tracking and calorimeter reconstruction is performed, electron identification routines are run, and data from different detector components are correlated. The physics analysis begins from these fully reconstructed events.

Chapter 3

Data-taking

3.1 Accelerator Operation

Physics data were collected at HERA between June and December of 1992 and between June and December of 1993. HERA ran continuously over these periods, although there were some short shutdown periods for either detector or accelerator maintenance. In this section the procedure followed to achieve beam collisions for data-taking is outlined. The typical accelerator conditions under which the physics data analyzed in this dissertation were taken are also described.

3.1.1 Beam Collisions

The operation of HERA followed a cycle of beam injection, acceleration to the running energy, tuning for beam collisions, and storage. Injection of the proton beam begins by accelerating negatively charged hydrogen ions (H^-) to 50 MeV in a RF quadrupole linac. The H^- ions are stripped of both electrons to produce protons and the protons are injected into the DESY III synchrotron. DESY III is filled with 11 bunches of protons spaced 28.8 m apart (the bunch spacing in HERA is also 28.8 m), and the beam is accelerated to 7.5 GeV. The protons are then transferred

to the PETRA II synchrotron. PETRA II is filled with 70 bunches of protons which circulate with a spacing of 28.8 m, and the beam is accelerated to 40 GeV. The protons are then transferred to HERA, which is filled with a maximum of 210 bunches, and the beam is then accelerated to its final running energy.

Injection of the electron beam begins by accelerating electrons to 500 MeV in a linac. A single electron bunch is accumulated in the small storage ring PIA. From PIA, the single bunch is transferred to the DESY II synchrotron, where it is accelerated to 7.5 GeV. The bunch is then transferred to the PETRA II synchrotron. In this manner, PETRA II is filled with 70 electron bunches which circulate with a spacing of 28.8 m. Once filled, the beam is accelerated in PETRA II to 14 GeV and transferred to HERA. HERA stores a maximum of 210 electron bunches, and then accelerates the beam to its final running energy.

Tuning for collisions begins when both beams are at their final running energies. Magnet and RF phase adjustments are made to achieve the highest possible luminosity and to make the collisions occur roughly at the nominal interaction point ($z = 0$). Collimators, which are extrusions into the beam pipe which can be moved in and out, are inserted in order to collimate the beams and scrape away beam halo particles.

During beam injection and tuning for collisions the ZEUS detector is held in the "safe state". In the safe state the CTD high voltage remains off, and the FCAL and RCAL remain open by 50 cm. The calorimeter supporting structures are constructed so that the FCAL and RCAL can be separated into two halves, both of which can be moved away from the beam pipe by 50 cm. These measures prevent damage to the detector due to high backgrounds experienced during beam injection and tuning.

During beam injection and tuning for collisions the backgrounds are monitored using the C5 and veto wall trigger rates. When the trigger rates are acceptable the FCAL and RCAL are closed, the CTD high voltage is switched on, and stable data-taking ensues.

When the beam currents or luminosity become low or beam conditions degrade giving high backgrounds the beams are dumped. This is done by pulsing “kicker” magnets in HERA which direct the beams out of the beam pipe and into a beam dump.

3.1.2 Typical Running Conditions

During the 1992 and 1993 experimental running periods HERA ran at an electron beam energy of 26.7 GeV and a proton beam energy of 819.9 GeV. For the 1992 running period HERA ran with nine colliding bunches, one electron pilot bunch, and one proton pilot bunch. For the 1993 running period HERA ran with 84 colliding bunches, 10 electron pilot bunches, and six proton pilot bunches.

Beam currents during stable data-taking were typically 10-15 mA for both electron and proton beams. The length of time for which the beams could be stored varied, but generally proton beams could be stored for 10-12 hours or more. The lifetime of the stored electron beam was shorter, typically several hours.

At the beginning of the 1993 experimental running period the proton ring of HERA was run with its 52 MHz RF system. Using this system the average proton bunch length was observed to be 40 cm. After about one-third of the running period had expired HERA switched to running with its 208 MHz proton ring RF system. With the 208 MHz RF system the proton bunch length was observed to be 20 cm. In comparison, the electron bunch length was always small, typically shorter than 10 cm. The finite electron and proton bunch lengths resulted in a distribution of event vertices.

In the first two experimental running periods, “satellite” bunches were observed in the running of HERA. These are small bunches which follow and/or precede the main bunches in the HERA rings. In the 1992 running period, satellite electron bunches were observed to follow the main electron bunches by 8 nsec. Any bremsstrahlung events from these satellite bunches contributed to the luminosity mea-

surement. However, any deep inelastic scattering (DIS) events from these satellite bunches were removed by timing cuts. Therefore, the measured integrated luminosity for the 1992 running period was decreased by about 6% to account for the unused luminosity from the electron satellite bunches.

During the 1993 running period satellite proton bunches were observed 5 nsec both before and after the main proton bunches. The events from these proton satellite bunches contributed to the luminosity measurement. The event times they produce are within the timing cuts, and they were thus retained in the data sample. However, they are responsible for producing a second peak in the overall event vertex distribution at $z \approx 60$ cm.

During stable data-taking the typical luminosity was about $0.7 \times 10^{30} \text{ cm}^{-2}\text{s}^{-1}$. Over the entire 1992 running period HERA delivered a total integrated luminosity of 30.5 (nb)^{-1} . Over the entire 1993 running period HERA delivered a total integrated luminosity of 1006 (nb)^{-1} .

3.2 Detector Operation

3.2.1 Experimental Running

The ZEUS detector is manned by a crew of four people. They determine whether or not conditions are suitable for data-taking, move ZEUS between its safe and data-taking states, use run control to include various components of ZEUS in the data-taking, establish the trigger, and keep a check on the functioning of the ZEUS detector. During stable data-taking the crew monitors the background conditions and luminosity, and checks the validity of the data passing through the data collection chain using online event displays and histograms giving statistics on triggered and rejected events. Data-taking stops if either backgrounds increase too much, the dead time is too high, the beams are about to be dumped, or some component experiences hardware problems.

During the 1993 experimental running period a total of 636 runs were taken. The average integrated luminosity per run, referred to as the “gated” luminosity, was 0.965 (nb)^{-1} . The average elapsed time per run was 74 min. The total gated luminosity for the 1993 running period was 615 (nb)^{-1} . The ZEUS experiment was not able to use all luminosity delivered by HERA for reasons of bad beam conditions, beam tuning by HERA, time spent closing the calorimeter and ramping up the CTD high voltage, hardware failures, or other trigger-related dead time.

Of the 615 (nb)^{-1} of gated luminosity collected by the ZEUS experiment only 554 (nb)^{-1} was good for analysis purposes. The 61 (nb)^{-1} of rejected luminosity was collected when the CTD high voltage was not on, the magnets were not on, the calorimeter was not completely closed, or the data had passed through a channel known to produce transmission errors. Data taken under these conditions were rejected to ensure data quality.

3.2.2 Backgrounds to Deep Inelastic Scattering

Three major sources of background to the deep inelastic scattering processes were encountered during data-taking: beam-gas interactions, cosmic ray muons, and sparks. In this section the measures taken online to remove these backgrounds from the data will be discussed.

3.2.2.1 Beam-gas Interactions

Events where either the electron beam or proton beam interacts with the residual gas in the beam pipe are referred to as beam-gas interactions. An event may be triggered when ZEUS detects the products of these interactions. The calorimeter timing was used to reject such triggers.

In each channel of the calorimeter, the signal time is first calculated with respect to a fixed reference which is the same for all channels. Then a time offset is applied

to each channel based upon its spatial location within the calorimeter. This time offset moves the reference time for each channel to be the signal time a particle coming from the interaction point traveling at the speed of light would produce. For convenience, this time, t , is assigned as $t = 0$.

The FCAL time, t_{FCAL} , and RCAL time, t_{RCAL} , are calculated as weighted averages of the signal times in all channels in the respective calorimeter, i.e.,

$$t_{FCAL,RCAL} = \frac{\sum_i w_i t_i}{\sum_i w_i},$$

where t_i is the time of the channel signal and w_i is the weight. The SLT (second level trigger) and TLT (third level trigger) definitions of the weights, w_i , used for calculating t_{FCAL} and t_{RCAL} differ slightly. In general, the quantity w_i depends upon the energy in the channel. For instance, in the TLT w_i is defined by

$$w_i = \begin{cases} 2 & \text{if } E_i > 2 \text{ GeV} \\ E_i & \text{if } 0.2 \text{ GeV} < E_i \leq 2 \text{ GeV} \\ 0 & \text{if } E_i \leq 0.2 \text{ GeV}, \end{cases}$$

where E_i is the energy in the channel. In genuine electron-proton interactions, the distributions of t_{FCAL} and t_{RCAL} should be centered around zero.

In proton-gas events occurring behind the RCAL, the interaction products strike the RCAL at roughly the same time at which the proton beam passes by the RCAL. Consequently, t_{RCAL} will be “early” by the amount of time it takes to travel twice the distance between the RCAL and the interaction point. Since the RCAL is roughly 150 cm from the interaction point, proton-gas interactions will have RCAL times of $t_{RCAL} \approx -10$ nsec. On the other hand, the products of proton-gas interactions will be “on time” in the FCAL, i.e., $t_{FCAL} \approx 0$. Equivalently, the time difference, $|t_{FCAL} - t_{RCAL}|$, will equal approximately 10 nsec in proton-gas events occurring behind the RCAL.

The situation is similar for electron-gas events occurring behind the FCAL. In this case the interaction products strike the FCAL at roughly the same time at

which the electron beam passes by the FCAL. This leads to FCAL times which are early by the amount of time it takes to travel twice the distance between the FCAL and the interaction point. As the FCAL is about 220 cm from the interaction point, the FCAL time for these events will be $t_{FCAL} \approx -14$ nsec. In these same events the interaction products will be on time in the RCAL, i.e., $t_{RCAL} \approx 0$. Equivalently, the time difference, $|t_{FCAL} - t_{RCAL}|$, will be approximately 14 nsec in electron-gas events occurring behind the FCAL.

Timing cannot be used to reject beam-gas events when the interaction occurs between the FCAL and RCAL. In proton-gas events occurring between the FCAL and RCAL, the products strike the FCAL with a time of $t_{FCAL} \approx 0$ and there will be no RCAL signal. In electron-gas events occurring between the FCAL and RCAL, the products will strike the RCAL with a time of $t_{RCAL} \approx 0$ and there will be no FCAL signal. Therefore, neither the absolute calorimeter times nor the time difference between the two calorimeters can be used to reject the event.

The electron and proton pilot bunches were used to estimate the rate of triggers in the colliding bunches due to beam-gas interactions. This was done by subjecting all data taken in the pilot bunch crossings to the same online trigger as data taken in the colliding bunch crossings. It can be assumed that the interactions of a given beam with the other colliding beam is independent of the interactions of the beam with the residual gas in the beam pipe. The number of events triggered in the pilot bunches which pass through the complete data collection chain is then a measure of the number of triggers in the colliding bunches due to beam-gas interactions.

3.2.2.2 Cosmic Ray Muons

Cosmic ray muons passing through the detector were another source of background. Events triggered by cosmic ray muons were identified and rejected online by algorithms based on event topology, calorimeter timing, and tracking. The algorithms were not completely efficient, and even after offline processing some events triggered

by cosmic ray muons remained in the data sample. As far as possible these events were identified and removed by hand. The trigger rate due to cosmic ray muons was studied by triggering on empty bunch crossings having neither proton nor electron bunches. Since most of the cosmic ray muon background is caused by almost vertical muons, the rate was quite low to begin with.

3.2.2.3 Sparks

The last major background was from so-called “sparks” in the calorimeter. Each PMT was surrounded by a metal cylinder, often at ground potential, which shielded it from any residual magnetic field of the superconducting solenoid. The surface of this magnetic shield and the surface of the PMT thus formed a cylindrical capacitor. Careful measurements revealed that the PMT’s leaked charges through the front face at the photocathode and through the cylindrical surface, placing the entire surface of the PMT at negative high voltage. The strong transverse electric field between the PMT and the magnetic shield produced electrical discharges, or sparking, between the two. Because the cylindrical capacitor formed by the PMT and magnetic shield could store 9.28×10^{-5} Joules, these discharges could cause spurious experimental triggers and be detrimental to the Cockcroft-Walton PMT bases. This problem was handled by wrapping the cylindrical surface of all PMT’s in aluminum foil, and then grounding the aluminum foil, effectively draining the charges so that none could build up on the cylindrical surface of the PMT.

In addition, since the front face of the PMT was at negative high voltage (typically -1500 V) while the transition piece (see Section 2.2.1.3) was grounded, a high electric field existed between the two. In addition to possible sparking, this electric field could incite scintillations, ionizations, or excitations due to collisions of the air molecules lying between the front face of the PMT and the transition piece. Any light emitted when this happened could be detected as a signal.

Sparking was mainly confined to the BCAL, where there were installation errors as described in the previous two paragraphs. Since the sparking only affected individual channels, an event triggered by sparking could be identified and rejected by requiring that the event be triggered only by one BEMC tower and that a single cell contain most of the energy. This cell was required to possess a large “imbalance”, and to have the electronics in both of its channels functioning properly. A cell had a large imbalance when there was much more energy in the channel on one side of the cell than in the channel on the opposite side. With greater luminosity the spark nuisance can be overcome by increasing the trigger thresholds.

3.2.3 Online Trigger

A broad overview of the online trigger scheme was presented in section 2.2.8. The global first level trigger (GFLT) receives 51 16-bit hardware signals from the first level triggers (FLT) of the various components of ZEUS at each bunch crossing. From these, the GFLT forms 64 subtriggers, which are either the hardware signals themselves, or coincidences between two or more signals. The decision on whether or not to accept the event is the logical OR of a subset of the 64 subtriggers. If a subtrigger is “prescaled” by a factor of n , only every n^{th} time the subtrigger is satisfied will it contribute a logical TRUE signal to the GFLT logical OR. Some subtriggers are prescaled in order to reduce the volume of data passing through the data collection chain.

The component providing the largest number of subtriggers for the GFLT decision is the calorimeter. The calorimeter cells are grouped together to form 896 trigger towers. A trigger tower has an EMC component and a HAC component, each with a separate, programmable threshold. The EMC component consists of two (RCAL) or four (BCAL and FCAL) EMC cells, and the HAC component consists of one HAC1 cell and one HAC2 cell. For each trigger tower the trigger electronics produces sums of the total EMC energy, total HAC energy, and the transverse energy in the tower. These quantities are compared to the thresholds, and a trigger is issued for the tower if any of the thresholds are exceeded.

A non-exhaustive list of some GFLT subtriggers involving the calorimeter are given in Tables 3 and 4. Three types of calorimeter quantities appear in these tables. “Total energy” is a scalar sum of energy in the calorimeter. “Transverse energy” is the scalar sum of the energy flow transverse to the z -axis. Lastly, “missing energy” is the vector sum of transverse energy, which by conservation of momentum should be nearly zero. The trigger electronics sets bits (0 through 7) for each tower depending on the amount of energy it contains. In the “threshold sum” the trigger decision is based on the summation of these bits.

The SLT removes events passing the FLT which are triggered by beam-gas interactions or sparks. The timing algorithm rejects events where $|t_{RCAL}| > 8$ nsec or $|t_{FCAL}| > 8$ nsec. Only events surviving the SLT selection criteria are passed on to the TLT.

The TLT removes events triggered by cosmic ray muons, beam-gas interactions, and sparks. The timing algorithm rejects events where

$$|t_{FCAL} - t_{RCAL}| > 8 \text{ nsec}, \quad |t_{RCAL}| > 8 \text{ nsec}, \quad \text{or} \quad |t_{FCAL}| > 8 \text{ nsec}.$$

In addition, a “global” calorimeter time, t_{GLOBAL} , is calculated. This is a weighted average of the signal times of all channels in the calorimeter, such that an “in time” event should possess a global time of $t_{GLOBAL} \approx 0$. The TLT rejects events where $|t_{GLOBAL}| > 8$ nsec.

All events surviving the cosmic, beam-gas, and spark removal algorithms of the TLT then pass through online algorithms which classify the events according to their physics content. Each event is classified as belonging to at least one of the following classes: photoproduction, DIS, exotic, or boson-gluon fusion. Within each of these classes several subclasses exist. For instance, DIS events are categorized as being nominal neutral current, high- Q^2 neutral current, or charged current. The TLT sets tagging bits that indicate to which class and subclass each event belongs.

3.2.4 Dead Time

The trigger dead time during the 1992 and 1993 experimental running was consistently at the 1% level. This was because during 1992 and 1993 HERA ran at less than 5% of its design luminosity. Also responsible for keeping the dead time low is that the FLT and SLT are buffered, so the data can be stored while the trigger electronics makes its decision.

Chapter 4

Selection of DIS Events and Identification of the Scattered Electron

During the 1993 data-taking period, 6.1 million events were collected and written to mass storage media. By applying some loose criteria, 320K candidate neutral current (NC) interaction events were selected and written to data summary files. These data summary files were the starting point for the analysis presented in this dissertation. More stringent timing and kinematic requirements were imposed and an electron identification routine was implemented in order to extract a pure sample of about 28K DIS events from which the physics analysis could begin.

4.1 Summary Data

In this section the loose criteria used to select candidate NC events for the summary data will be listed. These criteria reduced the number of events so that the entire data set could be stored on computer disk, rather than computer tape, which facilitated the physics analysis.

For a given event to be chosen as a candidate NC event it was first required that the event be classified as a nominal NC event by the TLT. This occurred if in the event the following criteria were satisfied :

- One or more of the BEMC_E(3404), REMC_E(2032), and REMCth(3750) sub-triggers were satisfied (see Table 3);
- $(E - P_z) + 2E_\gamma > 20$ GeV where E is the total energy in the calorimeter, P_z is the total z -component of momentum as measured by the calorimeter, and E_γ is the amount of energy in the photon detector of the luminosity monitor; and
- $(E - P_z) < 100$ GeV where E and P_z are the same as in the previous item.

The quantity $(E - P_z)$ as measured by the calorimeter proved to be effective in the selection of DIS events. A discussion of this quantity will be deferred until Section 4.2.3.

A requirement on the event timing, using the fully calibrated timing signals in the calorimeter, was made to remove events triggered by beam-gas interactions or out-of-time cosmic ray muons. This requirement rejected any event in which

$$|t_{RCAL}| > 6 \text{ ns}, \quad |t_{FCAL}| > 8 \text{ ns}, \quad |t_{FCAL} - t_{RCAL}| > 8 \text{ ns}, \text{ or } |t_{GLOBAL}| > 8 \text{ ns}.$$

Here t_{RCAL} is the timing signal of the RCAL, t_{FCAL} is the timing signal of the FCAL, and t_{GLOBAL} is the global timing signal.

Events triggered by cosmic ray muons, beam halo muons, or sparks were rejected by means of pattern recognition programs. The algorithm for identifying cosmic ray muons was the same as the one used online, with the exception that the offline version used more stringent rejection criteria.

A more stringent requirement on the quantity $(E - P_z)$ than that applied by the TLT was imposed. This requirement was that

$$(E - P_z) + 2E_\gamma > 25 \text{ GeV},$$

where E is the total energy in the calorimeter, P_z is the total z -component of momentum as measured by the calorimeter, and E_γ is the amount of energy in the photon detector of the luminosity monitor.

Finally, four electron identification algorithms were run on the events selected by the criteria listed above. Only events in which at least one of the four algorithms succeeded in identifying a scattered electron were written to the data summary files.

4.2 Selection of DIS Events from the Summary Data

Extraction of the DIS events from the data summary files was accomplished by tightening the event timing and $(E - P_z)$ criteria. Additional background rejection was also employed by removing events in which either the C5 counter or veto wall were triggered. An electron identification algorithm, discussed in the next section, was used to obtain the final sample of electron scattering events.

4.2.1 Event Timing

The event timing requirement was tightened slightly by rejecting events where

$$|t_{RCAL}| > 6 \text{ ns}, \quad |t_{FCAL}| > 6 \text{ ns}, \text{ or } |t_{FCAL} - t_{RCAL}| > 6 \text{ ns}.$$

The quantities t_{RCAL} and t_{FCAL} are the RCAL and FCAL timing, respectively. These criteria ensured that the event vertex was located between the FCAL and RCAL in addition to removing events triggered by beam-gas interactions or out-of-time cosmic ray muons.

4.2.2 Event Vertex

For each event the interaction vertex needed to be determined. This was done by first checking whether or not the ZEUS tracking software had located a primary vertex. If so, then this was used as the event vertex.

In some instances the tracking software was unable locate an event vertex. In this case the calorimeter timing was used. The calorimeter is calibrated to produce a timing of zero for any particles arriving from the nominal interaction point (see Section 3.2.2.1). Any deviation from this timing therefore indicates that the particles originated from somewhere other than the nominal interaction point. For purposes of determining the event vertex the FCAL timing was used.

For reliable results, the algorithm to determine the event vertex using the FCAL timing required a minimum amount of energy in the FCAL. If there was not enough energy in the FCAL to satisfy the algorithm then the vertex had to be set by hand. The distribution of all tracking and calorimeter vertices indicated that, over the entire data-taking period, the average event vertex was located at $z = -6.3$ cm. Therefore, if both the tracking and calorimeter timing failed to find an event vertex then it was assigned to be -6.3 cm.

The tracking was able to locate a vertex in 89.5% of all DIS events. The calorimeter timing was resorted to in 10% of the DIS events. In the remaining 0.5% of the DIS events the vertex was assigned to be the average vertex.

4.2.3 $E - P_z$ Requirement

It follows from energy-momentum conservation that $2E_e = (E - P_z)$, where E_e is the incident electron energy. E is the total energy of the final state, i.e., $E = \sum_i E_i$, where E_i is the energy of the i^{th} final state particle. P_z is the total z -component of momentum of the final state, i.e., $P_z = \sum_i p_{zi}$, where p_{zi} is the z -component of the momentum of the i^{th} final state particle.

The quantity $(E - P_z)$ is measured by the calorimeter as

$$(E - P_z) \approx \sum_i E_i(1 - \cos \theta_i),$$

where E_i is the energy in the i^{th} calorimeter cell and θ_i is the polar angle of the i^{th} calorimeter cell with respect to the position of the event vertex. The summation runs over all calorimeter cells with energy greater than the DU signal suppression thresholds (see Section 2.2.1.5).

For events which are “fully contained” in the sense that the energies of all final state particles are measured by the calorimeter, $(E - P_z)$ as measured by the calorimeter should be approximately 53.4 GeV, since $E_e = 26.7$ GeV. However, final state particles often escape undetected by staying in the beam pipe. When this happens the measured value of $(E - P_z)$ will be smaller than 53.4 GeV.

Particles traveling in the forward direction have $E_i \approx p_{zi}$, and so they do not contribute significantly to $(E - P_z)$. Therefore, particles going in the forward direction which escape undetected do not significantly change the value of $(E - P_z)$ as measured by the calorimeter. On the other hand, particles which travel in the rear direction have $E_i \approx -p_{zi}$, and therefore contribute roughly $2E_i$ to the value of $(E - P_z)$. Thus, any high energy particles going in the rear direction which escape undetected can cause a significant decrease in the value of $(E - P_z)$ as measured by the calorimeter.

Three particular types of events merit special attention. First, in low- Q^2 events ($Q^2 \approx 0$) the electron scattering angle is so small that the scattered electron stays in the beam pipe and escapes detection by the calorimeter. Second, in events where the incident electron radiates a photon, the photon tends to travel collinear to the direction of the incident electron. Thus, it stays in the beam pipe and escapes detection by the calorimeter. Third, in proton beam-gas interactions occurring between the RCAL and FCAL all produced particles travel in the forward direction. Thus, the calorimeter should measure a value of $(E - P_z)$ of approximately zero in proton beam-gas events.

In summary, requiring $(E - P_z)$ as measured by the calorimeter to be approximately 53.4 GeV selects the DIS events with a scattered electron in the calorimeter, while removing the low- Q^2 and proton beam-gas backgrounds. For extracting DIS events from the summary data it was required that $(E - P_z)$ as measured by the calorimeter satisfy the relation

$$35 \text{ GeV} < (E - P_z) < 60 \text{ GeV}.$$

The inefficiency introduced by this criterion was estimated using a Monte Carlo simulation, and the results are presented in the next chapter. The greatest loss of genuine DIS events caused by the $(E - P_z)$ requirement is in the “deep” inelastic region, where the scattered electron energy is small.

4.2.4 C5 and Veto Wall

Events triggered by beam-related background or beam-gas interactions were rejected by checking whether the C5 or veto wall were hit.

4.2.5 Detector Conditions

Finally, data taken when any of the critical components of ZEUS was not in a proper data-taking state was rejected. This meant rejecting data taken when the CTD or magnets were off, either the FCAL or RCAL was open, there were a large number of dead channels in the calorimeter, or the data had passed through a processing channel known to produce transmission errors. The gated luminosity for each run was reduced in proportion to the number of events removed for these reasons.

4.3 Identification of the Scattered Electron

An electron identification algorithm was run on all DIS events selected from the summary data. The details of this algorithm and the difficulties inherent in electron finding with the ZEUS calorimeter are presented in this section.

In order to select events where the electromagnetic shower of the scattered electron is fully contained in the calorimeter, the possibility that the scattered electron is misidentified is small, and the efficiency for finding the scattered electron is high, the scattered electron energy, its impact position on the calorimeter, and its scattering angle were required to fulfill certain criteria. After imposition of these criteria a data sample of 27,629 clean electron scattering events remained.

4.3.1 Calorimeter Clusters

Electromagnetic and hadronic showers in the ZEUS calorimeter typically deposit energy in several neighboring calorimeter cells. Identifying isolated showers in the ZEUS calorimeter therefore requires that all cells in which energy has been deposited be grouped together in some fashion to form single entities. These entities are called calorimeter clusters.

Specifically, a calorimeter cluster is defined as a group of cells in which (1) each member has energy above the DU signal suppression threshold (see section 2.2.1.5), (2) each member borders at least one other cell in the group on a side, and (3) there is only one “local maximum”. Graphical illustrations of this definition are given in Figures 20, 21, and 22. In these figures the calorimeter cells are depicted as squares in the x - y plane and the height of each square along the z -axis depicts the amount of energy deposited in the cell.

Figure 20 is a lego plot of a hypothetical single cluster. All the cells in the cluster border at least one other member on a side and there is only one cell of local maximum energy deposition. In contrast, Figure 21 illustrates two hypothetical

clusters. There are two cells which border each other on a corner and there are two cells which have a local maximum energy deposition.

In Figure 22 all the cells containing energy border at least one other cell on a side. However, this large group can be resolved into two smaller clusters since there are two cells which have local maximum energy deposition. The large group of cells is separated into two clusters by assigning the energy in the cells intervening between the two local maxima to one of the two clusters.

4.3.2 Determination of the Scattered Electron Cluster

Identifying the scattered electron begins by finding all calorimeter clusters, and then deciding which of these are electromagnetic showers. One of these showers is then chosen as belonging to the scattered electron.

For each cluster the total energy in the EMC cells of the cluster, E_{EMC} , and the total energy in the HAC cells of the cluster, E_{HAC} , is calculated separately. The key quantity in determining whether a cluster is an electromagnetic shower is the ratio E_{EMC}/E_{total} , where $E_{total} = E_{EMC} + E_{HAC}$. For electromagnetic showers this ratio should be approximately unity.

In computing E_{EMC} the HAC cells of the RCAL immediately adjacent to the beam pipe hole are treated as EMC cells, since they are directly exposed to the interaction point as are ordinary EMC cells.

All clusters having $E_{EMC}/E_{total} \geq 0.95$ are selected as electromagnetic showers and are considered as scattered electron candidates. For each candidate the two EMC cells with the greatest amount of energy are identified, and the sum of their energies, E_{2EMC} , is calculated. The transverse momentum of the two highest energy cells, P_{12EMC} , is calculated as $P_{12EMC} = E_{2EMC} \times \sin \theta_c$, where θ_c angle of the cluster with respect to the event vertex. The scattered electron is chosen as the electron candidate for which the quantity P_{12EMC} is largest.

4.3.3 Efficiency and Misidentification in Finding the Scattered Electron

The method just described for identifying the scattered electron in the ZEUS calorimeter is not fully efficient. Should the scattered electron and a hadron strike the calorimeter in close proximity the showers they produce may overlap. If they are too close together the clustering algorithm will not be able to resolve the two showers. Hence, the electron identification algorithm will not be able to identify the scattered electron correctly.

Under certain circumstances a hadron entering the calorimeter may be misidentified as a scattered electron. This is because in some instances a low energy hadron may stop completely in the EMC section of the calorimeter. The energy it deposits will then be mistaken as an electromagnetic shower. Another possibility is that π^- particles traversing the dead material preceding the calorimeter will participate in the charge exchange process to produce a π^0 particle. The electromagnetic showers created by the two photons from the decay of the π^0 may be mistaken as belonging to the scattered electron.

The efficiency and misidentification in finding the scattered electron were investigated using Monte Carlo simulations and visual scanning of the data taken during the 1992 running period. The results of the efficiency studies are presented in the next chapter. The possibility of misidentification of the scattered electron was kept to a minimum by requiring the energy of the identified scattered electron to be greater than 10 GeV, the justification for which will be explained in Section 4.3.5.

4.3.4 Position and Angle Measurement of the Scattered Electron

The position of a shower is defined as the location at which the maximum amount of energy is deposited by the shower. For all clusters, with the exception of the cluster

belonging to the scattered electron, the shower position, $(\bar{x}, \bar{y}, \bar{z})$, was estimated by taking the energy-weighted average of the geometric centers of all cells in the cluster, i.e.,

$$\bar{x} = \sum_i E_i(x_0)_i / \sum_i E_i, \quad \bar{y} = \sum_i E_i(y_0)_i / \sum_i E_i, \quad \bar{z} = \sum_i E_i(z_0)_i / \sum_i E_i.$$

Here E_i is the energy in the i^{th} cell, $((x_0)_i, (y_0)_i, (z_0)_i)$ are the coordinates of the geometric center of the i^{th} cell, and the summation runs over all the cells in the cluster.

For the scattered electron cluster, refinements are employed to estimate the shower position. For the x position an energy-weighted average is used. However, instead of using the exact geometric centers of the cells, an offset is applied based on the energy measurements on both sides of the cells. For the RCAL, experimental data from the RHES was used. The cell offsets as determined by the RHES were correlated with the cell energy imbalances (difference between energy measurements on opposite sides of the cell) as measured by the calorimeter. A function was generated to describe this correlation; therefore, given the cell imbalances as measured by the calorimeter the offsets are determined. For the FCAL, a standard empirical parametrization was adopted in which the offset for each cell was taken to be $(\lambda/2)\ln(E_R/E_L)$. In this expression λ is the attenuation length of the scintillator, E_R is the energy in the right channel of the cell, and E_L is the energy in the left channel of the cell. In beam tests [27], the value of λ for the ZEUS calorimeter was measured to be 21 cm.

For the y position of the scattered electron cluster in the RCAL and FCAL a theoretical shower profile is used. The y position of the shower is first estimated as the geometric center of the maximum energy cell in the cluster. The fractions of the total shower energy contained in the maximum energy cell and in its neighboring cells directly above and directly below (in the y coordinate) are computed. According to the theoretical shower profile, these fractions determine how much the shower position in y is offset from the geometric center of the maximum energy cell.

For the z position of the scattered electron cluster in the RCAL and FCAL Rossi's parametrization of the depth, \bar{t} , of the shower center of gravity for electromagnetic showers was used [31]. This formula reads

$$\bar{t} = (\ln(E_{total}/E_{crit}) + 0.4)X_{eff},$$

where E_{total} is the total shower energy, E_{crit} is the critical energy, and X_{eff} is the effective radiation length. For the ZEUS calorimeter the values of X_{eff} and E_{crit} were measured in beam tests to be 0.74 cm and 10.6 MeV, respectively [27]. Since the scattered electron always strikes the FCAL and RCAL at an angle, the depth, \bar{t} , of the shower center of gravity is projected onto the z -axis to obtain the z -coordinate of the shower position.

In the BCAL it is only necessary to calculate the shower position in the azimuthal (ϕ) and longitudinal (z) coordinates. In both cases the maximum energy cell in the cluster and its neighboring cell (in the appropriate coordinate) containing the most energy are used. The ratio of the energies of these two cells is used to deduce by what distance the shower position is offset from the geometric center of the maximum energy cell.

The polar angle, θ_c , and azimuthal angle, ϕ_c , of all clusters were defined with respect to the event vertex. They were calculated using the following formulae:

$$\cos \theta_c = (\bar{z} - v_z)/r, \text{ and } \cos \phi_c = (\bar{x} - v_x)/\rho,$$

where $(\bar{x}, \bar{y}, \bar{z})$ are the coordinates of the shower position and (v_x, v_y, v_z) are the coordinates of the event vertex. The quantity

$$r = \sqrt{(v_x - \bar{x})^2 + (v_y - \bar{y})^2 + (v_z - \bar{z})^2}$$

is the distance between the shower position and the event vertex, and the quantity

$$\rho = \sqrt{(v_x - \bar{x})^2 + (v_y - \bar{y})^2}$$

is the length of the projection of r in the transverse plane.

4.3.5 Scattered Electron Energy Restriction

Low energy pions which stop in the EMC section or deposit less than 5% of their energy in the HAC section are the particles most apt to be misidentified as low energy scattered electrons. In order to investigate this, Monte Carlo simulations of electron-proton scattering at HERA in which the ZEUS detector response was modelled were performed. The experimentally measured scattered electron energy spectrum was compared with the Monte Carlo scattered electron energy spectrum. Above electron scattering energies of about 10 GeV, the two spectra were found to agree, after taking into consideration a calorimeter energy scale effect. Below electron scattering energies of about 10 GeV, however, the two spectra were found to disagree. In this region the experimental spectrum contained more events, indicating that there were many misidentified electrons in this region.

As a result, a criterion was imposed on the energy of the scattered electron. This criterion required that the scattered electron energy, E'_e , be such that $E'_e \geq 10$ GeV. Any event in which the scattered electron did not satisfy this requirement was rejected.

Ideally, low energy pions and electrons can be separated by a measurement of the ionization energy loss, $-dE/dx$, as the particles traverse the tracking chambers. However, for the 1993 data-taking the electronic components capable of making this measurement possible were in their first running period. Thus, the tracking chambers still had not been calibrated well enough to make a reliable measurement of $-dE/dx$, and therefore this method for electron-pion separation could not be employed for the analysis in this dissertation.

4.3.6 Scattered Electron Impact Position Restriction

When a scattered electron strikes the calorimeter close to the edge of the beam pipe some of the particles from the ensuing electromagnetic shower will spill into the beam pipe. Any ionization these particles might have produced in the calorimeter will be lost, and the energy of the electron will thus be measured incorrectly.

A requirement was therefore made of the impact position of any scattered electron striking the RCAL. It was required that the impact position of the scattered electron on the RCAL face, (x_{imp}, y_{imp}) , be such that

$$(|x_{imp}| > 16 \text{ cm}) \text{ or } (|y_{imp}| > 16 \text{ cm}).$$

This ensured that the electromagnetic shower of every electron to be used in physics analyses was fully contained within the calorimeter. Any event in which the scattered electron did not fulfill this requirement was rejected.

The inefficiency introduced into the angular distribution by this restriction on the scattered electron impact position was estimated using the observed vertex distribution. The results on this are presented in the next chapter.

4.3.7 Scattered Electron Angle Restriction

For the cross section calculations presented in this dissertation the data were placed in bins of scattered electron energy and scattered electron angle. To keep the effect of the scattered electron impact position restriction on the scattered electron angular distribution small, an upper bound of 170° was placed on the electron scattering angle. In other words, the electron scattering angle, θ_e , was required to be such that $\theta_e \leq 170^\circ$, and any event in which the scattered electron angle did not satisfy this requirement was rejected.

Chapter 5

Radiative Corrections and Acceptance Calculations Using Monte Carlo Methods

It is necessary to apply several corrections to the experimental data before performing the hadron analysis or extracting the proton structure functions (see Appendix A.2). This involves correcting for the detector acceptance, the trigger efficiency, the efficiency in identifying the scattered electrons, kinematical restrictions in event selection, and radiative processes. While most of these corrections are due to hardware or software effects, the radiative corrections are due to an unavoidable physics process arising from the photon emissions by the electrons either before or after scattering.

5.1 The Monte Carlo Package

The Monte Carlo package HERACLES [32] was used to evaluate most of the corrections which will be described in detail below.

HERACLES uses the LEPTO [33] program to simulate non-radiative electron-proton scattering. It also simulates the radiative effects of one-photon emission by either the electron or quark and the one-loop processes. The two simulations can run independently. HERACLES then calls the JETSET [34] program, which uses the Lund string model [35] to fragment the quarks and gluons into known hadrons in the final state. The output of each simulation event is an event record of all final state particles and their four-momenta.

The simulation of DIS events depends upon the distribution functions of the quarks and gluons inside the proton (see Appendix A.3). The ZEUS experiment is studying a kinematic region in which these distribution functions are yet to be measured. Therefore, theoretical extrapolations of the parton distribution functions must be used as inputs to the Monte Carlo simulation. The parton distribution functions in the simulations used in this dissertation were MRSD₀' and MRSD₀' [36]. These distribution functions proved to be very close to the results obtained by the ZEUS experiment. Thus, any errors introduced by using these functions to evaluate the corrections are negligible.

The ZEUS collaboration developed an executive Monte Carlo program named MOZART [37]. MOZART calls HERACLES to simulate electron-proton scattering events. It then feeds the information on the final state particles into the GEANT detector simulation program [38]. GEANT tracks each final state particle through the ZEUS detector, simulating the detector responses to these particles. MOZART stores the simulated responses in the format of the database management package ADAMO. The ADAMO format used for the Monte Carlo events is the same as that used for recording the actual experimental events (Section 2.2.8), which allows the use of the same analysis software for both Monte Carlo and experimental data.

Three Monte Carlo data sets were used for the calculations of the corrections to be described below. To calculate the $(E - P_z)$ acceptance and efficiency for identification of the scattered electrons a set of 36K MOZART events was used. To

calculate the radiative corrections two sets of 340K HERACLES events were used, one set including radiative effects, the other set having the radiative effects turned off. Both sets were generated according to the following kinematical parameters: $2 \times 10^{-5} < x < 0.98$, $Q^2 > 5 \text{ GeV}^2$, $0.01 < y < 0.98$, and $W > 5 \text{ GeV}$.

5.2 Acceptance and Efficiency Calculations

5.2.1 $(E - P_z)$ Acceptance

For the determination of cross sections (see Appendix A.2), the experimental data were binned in E'_e - θ_e space, where E'_e is the scattered electron energy and θ_e is the scattered electron angle. Therefore, in the acceptance calculations the Monte Carlo data were also binned in E'_e - θ_e space. For each bin the $(E - P_z)$ acceptance, $\epsilon_{(E-P_z)}$, was calculated as

$$\epsilon_{(E-P_z)} = \frac{N_{(E-P_z)}}{N_{no \text{ cut}}},$$

where $N_{(E-P_z)}$ is the number of events in the bin remaining after imposing the $(E - P_z)$ selection criterion and $N_{no \text{ cut}}$ is the number of Monte Carlo events in the bin without the $(E - P_z)$ selection criterion. Dividing the experimentally measured number of events in each bin by the value of $\epsilon_{(E-P_z)}$ for that bin corrected for the loss of events due to the imposition of the $(E - P_z)$ selection criterion. Figure 23, which shows $\epsilon_{(E-P_z)}$ as a function of E'_e in four different bins of θ_e , indicates that the $(E - P_z)$ selection criterion reduced the acceptance to an unreasonable level for $E'_e < 10 \text{ GeV}$. In the future, the $(E - P_z)$ selection criterion should be removed to ensure a better acceptance for low energy electrons.

5.2.2 Scattered Electron Impact Position Acceptance

The restriction on the impact position of the scattered electron amounted to accepting only those electrons which struck the RCAL face outside of a square of area $32 \text{ cm} \times 32 \text{ cm}$ around the beam pipe.

Assuming azimuthally symmetric scattering, the impact positions of all electrons having the same scattering angle, θ_e , and vertex, v_z , described a circle on the RCAL face. The impact position restriction cut away part of this circle. Therefore, the acceptance at a given θ_e and v_z , $\epsilon_{box}(\theta_e, v_z)$, is the fraction of the circle which lies outside the 32 cm \times 32 cm box.

The data were corrected in each bin of θ_e by calculating the average acceptance over the bin, $\overline{\epsilon_{box}}$. Dividing the experimentally observed number of events in each bin by the value of $\overline{\epsilon_{box}}$ for the bin corrected for the event loss due to the impact position restriction on the scattered electron.

Events were also excluded in which the electron struck the calorimeter at the boundary between the RCAL and BCAL. As most of the scattering in the ZEUS experiment thus far has been at low Q^2 , the number of events excluded by this restriction was very small. Therefore, emphasis has been placed on the relatively larger correction needed for the RCAL 32 cm \times 32 cm box acceptance.

5.2.3 Trigger Efficiency

Studies by the ZEUS trigger group indicated that the trigger efficiency for DIS events was at the 99% level. The deadtime over the running period was consistently at the 1% level. Therefore, no corrections for either of these inefficiencies were attempted for the analysis presented in this dissertation.

5.2.4 Efficiency for Identifying the Scattered Electrons

The efficiency for identifying the scattered electrons was investigated both by visual scanning and by Monte Carlo analysis. A good fraction of the data was visually scanned using the event display program LAZE [39]. By comparing the scattered electrons identified by the electron identification algorithm with those identified in the visual scan the efficiency for identifying the scattered electron was deemed to be greater than 95% for scattered electrons with energies greater than 10 GeV.

A more quantitative calculation of the scattered electron identification efficiency was undertaken using Monte Carlo data. After binning the data in E'_e - θ_e space, for each bin the scattered electron identification efficiency, ϵ_{elec} , was calculated as

$$\epsilon_{elec} = \frac{N_{id}}{N_{gen}},$$

where N_{id} is the number of correctly identified electrons in the bin and N_{gen} is the number of Monte Carlo events generated in the bin. Division of the experimentally observed number of events in each bin by the value of ϵ_{elec} for that bin corrected for the inefficiency in identifying the scattered electrons. Figure 24 shows ϵ_{elec} versus E'_e in four bins of θ_e . The efficiency is low for $E'_e < 10$ GeV but is nearly 100% for large values of E'_e . This result does not differ from that obtained by the visual scanning method. The low efficiency at small values of E'_e was caused by the difficulties in electron/pion separation when the energy of the scattered electron was less than 10 GeV.

5.2.5 Electron Scattering Angle Resolution

The MOZART data was also used to estimate the resolution on the determination of the electron scattering angle. The electron identification algorithm was run on the MOZART data sample and the electron scattering angle was calculated using the calorimeter information as described in Section 4.3.4. This reconstructed angle, θ_e^{rec} , was then compared with the electron angle generated in the Monte Carlo simulation, θ_e^{gen} , for each correctly identified electron. The distribution of $\theta_e^{gen} - \theta_e^{rec}$ was found to have a standard deviation of 0.4° , which is therefore the resolution on the determination of the electron scattering angle.

5.3 Radiative Corrections

In electron-proton scattering there is a good probability for the electron to emit a real photon either before or after scattering. When this occurs the kinematics of the event are changed. Since the proton form factor is a strong function of Q^2 this renders the observed spectra different from the “theoretical” spectra in which there is no photon emission. It is necessary to remove these radiative effects from the data first before the determination of the Born cross section, which is the cross section appropriate for the extraction of the proton structure functions (see Appendix A.2) and other relevant physics information.

In electroweak theory the electron-proton scattering cross section (see Appendix A.3) contains contributions from the following Feynman diagrams:

- the one-photon or Z^0 exchange process (Figure 25),
- the single-photon emission processes (Figure 26), and
- the one-loop processes (Figure 27).

The single-photon emission diagrams are infrared divergent, meaning that the cross section diverges as the energy resolution on the scattered electron becomes very small. However, inclusion of the one-loop processes will cancel the infrared divergence of the single-photon emission processes as well as preserve the gauge invariance of the scattering process.

The two HERACLES data samples with and without radiative effects were binned in E'_e - θ_e space as in the experimental data. For each bin the data set without the radiative effects was used to calculate the Born cross section for the bin, σ_{Born} . The data set including the radiative effects was used to calculate the “experimental” cross section for each bin, σ_{rad} . The effect of the radiative processes on the Born cross section was found by calculating the ratio

$$\delta_{rad} = \frac{\sigma_{Born}}{\sigma_{rad}}$$

for each bin. The experimentally measured cross section in every bin was then multiplied by the value of δ_{rad} for that bin to obtain the experimental Born cross section. Figure 28 shows δ_{rad} versus E'_e in four different bins of θ_e .

In the Monte Carlo data, initial state and final state radiation from the electron were treated differently. It was found that the scattered electron and any photon it emitted would not be separated in space by a distance larger than the calorimeter segmentation. Therefore, their energies were combined together and regarded as the energy of the scattered electron.

The so-called “QED Compton” radiative events were excluded separately. In these events the initial state electron emits a real photon in a direction parallel to that of the exchanged virtual photon. The momentum transfer for this process is a “minimum”, which makes the process observable. This radiative effect was corrected by removing these events from the experimental data sample. The number of these events was small, and they were easily identified by their azimuthal distributions.

Chapter 6

The Cross Sections for Final State Hadrons in Electron-Proton Scattering

In this dissertation a hadronic final state, X , is considered to be the product of the interaction between a virtual photon, γ^* , and a proton, p : $\gamma^* + p \rightarrow X$. For each event the spatial direction of the momentum of the incident virtual photon is taken as the reference direction.

With nearly 4π solid angle coverage and the ability to make measurements of both charged and neutral particles the ZEUS detector is well-suited for the study of the hadronic final state. Neither of these capabilities were available in previous DIS experiments.

The first section of this chapter presents a study of the rapidity distributions of the final state hadrons. It was found for the first time in this experiment that the hadrons in the virtual photon fragmentation region could be separated from the hadrons in the proton fragmentation region. As a result, all DIS events could be classified on the basis of whether or not virtual photon fragmentation was observed. Under this classification scheme, a special type of event emerged in which *only* fragmentation of the virtual photon was observed. In these events a rapidity gap with a width of more than four units was discovered.

In the second section of this chapter the differential cross sections for the virtual photon fragmentation process are presented. The contribution to the differential cross sections from the rapidity gap process is delineated throughout. Comparisons of the experimental results with a few theoretical models, mostly based on pomeron exchanges, are also presented.

6.1 The Final State Hadrons

6.1.1 The Analysis Method

6.1.1.1 Calculation of the Rapidity

All calorimeter clusters other than those belonging to the scattered electrons were considered to be final state hadrons. The type of each hadron could not be determined, so their masses were unknown as well. Therefore, all hadrons were assumed to be massless. If pion masses were assumed, it was found that the effect was within the experimental statistics quoted in this dissertation. The momentum of each hadron, \vec{p}_h , was determined using the calorimeter measurements of its energy, polar angle, and azimuthal angle (see Section 4.3.4). The four-momentum of the virtual photon, q , was determined from the difference between the four-momentum of the incident and scattered electron, $q = k - k' = (E_{\gamma^*}, \vec{q})$.

The rapidity distribution of the final state hadrons was studied using the spatial direction of the momentum of the incident virtual photon as the reference direction. The directional cosine of every hadron with respect to this direction, $\cos \theta_{\gamma h}$, was found according to the formula

$$\cos \theta_{\gamma h} = \frac{\vec{p}_h \cdot \vec{q}}{|\vec{p}_h| |\vec{q}|}.$$

Since the hadrons were assumed to be massless the pseudorapidity, η , was used. This was calculated from the angle of the hadron according to the formula $\eta = -\ln \tan(\theta_{\gamma h}/2)$.

6.1.1.2 Lorentz Transformation for CMS Analysis

The final state hadronic system was analyzed both in the laboratory frame provided by HERA as well as in the virtual photon-proton center-of-mass system (CMS). To perform the analysis in the CMS the four-momentum of every particle was subjected to a Lorentz transformation. The parameters of the transformation, γ and $\vec{\beta}$, were calculated according to the following formulae:

$$\gamma = \frac{E_p + E_{\gamma^*}}{W}, \text{ and}$$

$$\vec{\beta} = \frac{\vec{p}_p + \vec{q}}{E_p + E_{\gamma^*}},$$

where E_p and \vec{p}_p are the energy and momentum of the incident proton in the HERA frame, E_{γ^*} and \vec{q} are the energy and momentum of the virtual photon in the HERA frame, and W is the CMS energy of the virtual photon-proton system. In the CMS the angles and rapidities of all hadrons were calculated according to the formulae given in the previous paragraph, only using the values of \vec{p}_h and \vec{q} in the CMS.

6.1.1.3 Correction Procedure and Cross Section Calculation

Each DIS event contributes an amount w/\mathcal{L} to the cross section. The quantity w is an event weight which accounts for all acceptances and radiative corrections. It was given by

$$w = \frac{\delta_{rad}(E'_e, \theta_e)}{\epsilon_{(E-P_z)}(E'_e, \theta_e) \epsilon_{elec}(E'_e, \theta_e) \overline{\epsilon_{box}}(\theta_e)}$$

where E'_e is the energy of the scattered electron, θ_e is the angle of the scattered electron, $\epsilon_{(E-P_z)}$ is the acceptance of the $(E - P_z)$ selection criterion, ϵ_{elec} is the scattered electron identification efficiency, $\overline{\epsilon_{box}}$ is the acceptance of the scattered electron impact position restriction, and δ_{rad} is the radiative correction factor. The event weight w is unity if all acceptances are perfect and no radiative corrections are necessary. The quantity \mathcal{L} is the total integrated luminosity used in the analysis, which was 554 (nb)^{-1} (see Section 3.2.1).

In an event in which N^h hadrons are observed in the hadronic final state each hadron contributes an amount $(w/\mathcal{L})/N^h$ to the cross section.

To calculate the differential cross section to produce a hadron with rapidity η , rapidity space was divided into equally spaced bins, each $1/2$ unit of rapidity in width. All final state hadrons were binned according to their rapidities. In each bin the cross section $d\sigma/d\eta$ was calculated according to the formula

$$\frac{d\sigma}{d\eta} = \left(\sum_i \frac{w_i}{\mathcal{L}} \frac{1}{N_i^h} \right) \frac{1}{\Delta\eta}.$$

The quantity w_i is the event weight of the event in which the i^{th} hadron appeared, N_i^h is the total number of hadrons in the event in which the i^{th} hadron appeared, and $\Delta\eta$ is the width of the bin. The summation runs over all hadrons in the bin having energy greater than a threshold value. A threshold was placed on the hadron energies in order to suppress any noise produced by the depleted uranium of the calorimeter. All cross sections to be presented below were investigated using several different hadron energy thresholds. The hadron energy threshold selected for the presentation of the cross sections in this dissertation is 0.4 GeV.

6.1.1.4 Error Calculation

The error on the differential cross section in each bin was assigned the value of $(d\sigma/d\eta)(1/\sqrt{N_{obs}})$, where N_{obs} is the number of hadrons in the bin. This follows from assuming that the number of hadrons observed in a given bin follows a Gaussian distribution having an average and variance of N_{obs} .

6.1.1.5 Background Subtraction

In the data sample the numbers of events which were triggered by the electron and proton pilot bunches were used to estimate the amount of background from electron-gas and proton-gas interactions. After application of the $W \geq 130$ GeV criterion to be described in Section 6.1.2.1 it was found that there were 19 events

from the electron pilot bunches and eight events from the proton pilot bunches in the data sample. From a visual scan it was found that at least six electron pilot bunch events and six proton pilot bunch events were actually triggered by cosmic ray muons. Since the final number of events triggered by the pilot bunches was small a statistical background subtraction was deemed unreliable and therefore was not attempted. The events triggered by the pilot bunches were removed from the data sample before calculation of the differential cross sections.

6.1.2 Analysis of the Rapidity Distributions

6.1.2.1 Rapidity Distributions for Large and Small W

Two-body kinematics dictates that the width of the rapidity space available to the final state particles produced in a two-body interaction is roughly $\ln s$, where s is the square of the CMS energy of the two-body system. Thus, in the virtual photon-proton interactions under study in this dissertation the width of the rapidity space available to the final state hadrons should be roughly $\ln W^2$. This motivates investigating the rapidity distributions for large and small W events separately.

In Figure 29 $d\sigma/d\eta_{cms}$ is plotted versus η_{cms} for $W < 130$ GeV and $W \geq 130$ GeV separately. For $W \geq 130$ GeV, where the rapidity space available to the final state hadrons is larger, two peaks in the rapidity distribution are observed. The remainder of this dissertation examines these two-peaked events, and thus only events where $W \geq 130$ GeV are selected for analysis. This criterion reduced the data sample to about 15K events.

6.1.2.2 Event Classification Based on the Rapidity Distribution

In the HERA frame, with the direction of \vec{q} as the reference direction, one peak in the rapidity distribution was found in the forward hemisphere and therefore contained the virtual photon fragmentation hadrons. The other peak in the rapidity

distribution was found in the rear hemisphere and therefore contained the proton fragmentation hadrons. Thus, the forward hemisphere in the HERA frame is referred to as the “photon fragmentation region” and the rear hemisphere in the HERA frame is referred to as the “proton fragmentation region”.

Three types of events were identified: (1) those in which hadrons were observed in both the photon fragmentation region and proton fragmentation region, (2) those in which hadrons were observed only in the photon fragmentation region, and (3) those in which hadrons were observed only in the proton fragmentation region. This dissertation is concerned with the physics of virtual photon fragmentation, and thus cross sections will be presented for event types (1) and (2) (where hadrons are observed in the photon fragmentation region).

In Figure 30 the hadron rapidity distributions in the CMS are plotted. The open points show the distribution for hadrons in all events, while the closed points show the distribution for those events in which hadrons were observed in the proton fragmentation region and in the photon fragmentation region. It can be seen that the nearest edge of the beam pipe is located at a rapidity of $\eta_{cms} = -2$, since this is where the distributions drop to zero.

Figure 31 shows the hadron rapidity distribution for those events in which hadrons were observed only in the photon fragmentation region. Apparently a rapidity gap exists in the final state hadronic system for these events. The gap lies between the unobserved hadrons from the proton fragmentation which stay in the beam pipe, and the observed hadrons from the virtual photon fragmentation. The gap is at least four units in width, as this is the distance in rapidity between the lower edge of the rapidity distribution at $\eta_{cms} = 2$ and the nearest edge of the beam pipe, which is at a rapidity of $\eta_{cms} = -2$. The rapidity gap events numbered 630, or about 4.2% of the number of events where $W \geq 130$ GeV.

6.2 Cross Sections for Virtual Photon Fragmentation

In this section the differential cross sections for virtual photon fragmentation with respect to several kinematical variables are presented. In each case, the contribution to the differential cross section for virtual photon fragmentation from the process which creates a rapidity gap in the final state hadronic system is shown separately.

Events with a rapidity gap are hitherto unobserved in DIS. Therefore, LEPTO, the basic electron-proton scattering simulation package (see Section 5.1), does not account for events of this type. Ingelman [40] has conjectured that rapidity gap events are produced when the proton emits a pomeron with which the virtual photon interacts. The hypothetical pomeron is a Regge pole having the quantum numbers of the vacuum. The momentum distribution of partons inside the pomeron can be either hard or soft. This model has been implemented in the Monte Carlo program POMPYT [41], which uses the PYTHIA [42] Monte Carlo package.

Nikolaev and Zakharov [43] have conjectured that rapidity gap events are produced when the virtual photon fluctuates into a quark-antiquark pair, each of which interacts with a gluon from the proton. Thus, in this model, the “pomeron” is composed of two gluons, and separately each interacts with either the quark or antiquark from the virtual photon. This model has been implemented in a Monte Carlo program [44], which will be referred to here as the NIKZAK Monte Carlo program. One problem with this model is that the flux normalization cannot be easily fixed. It was found that the cross sections from the NIKZAK simulation were invariably smaller than the experimentally determined cross sections, but that the two could be made to agree best when the NIKZAK cross sections were multiplied by a factor of 3.72. In all NIKZAK cross sections presented in this chapter this factor has been applied in order to facilitate comparison between the experimental results and the NIKZAK results.

Both POMPYT, with hard and soft quark momentum distributions, and NIKZAK were used to simulate the rapidity gap events. The same method used to analyze the experimental data was employed in the analysis the Monte Carlo data, and the cross sections obtained will be compared to the experimental results in the following presentation. The cross sections from running POMPYT with a soft quark momentum distribution did not agree with the experimental cross sections and so will not be presented here.

Since LEPTO alone did not simulate the rapidity gap events, in order to obtain a Monte Carlo prediction for the experimentally measured virtual photon fragmentation cross sections either the POMPYT or NIKZAK cross sections needed to be added to the LEPTO cross sections. This procedure incorporated the effect on the cross sections of the rapidity gap process into the processes already simulated by LEPTO and was adopted to obtain the Monte Carlo predictions for the Q^2 and x photon fragmentation cross sections which are presented now.

6.2.1 Q^2 Distribution

To calculate the differential cross section for photon fragmentation with respect to Q^2 , $\log Q^2$ space above $\log Q^2 = 1$ was divided into equally spaced bins, each $1/3$ unit in width. In addition, one bin between $\log Q^2 = 0.90918$ and $\log Q^2 = 1$ was used. The lower edge of this bin, $\log Q^2 = 0.90918$ or $Q^2 = 8.113 \text{ GeV}^2$, is the kinematical lower limit given the scattered electron energy and angle selection criteria employed. All events in which photon fragmentation was observed were binned according to their Q^2 values. In each bin the differential cross section, $d\sigma/dQ^2$, was calculated according to the formula

$$\frac{d\sigma}{dQ^2} = \left(\sum_i \frac{w_i}{\mathcal{L}} \right) \frac{1}{\Delta Q^2},$$

where w_i is the event weight of the i^{th} event in the bin, ΔQ^2 is the width of the bin, and the summation runs over all events in the bin. The error on the differential cross section in each bin was assigned the value $(d\sigma/dQ^2)(1/\sqrt{N_{obs}})$, where N_{obs} is

the number of events observed in the bin. In Figures 32 and 33 the experimental determination of $d\sigma/dQ^2$ versus Q^2 is plotted as points. The open points show the photon fragmentation cross section, and the contribution to this cross section from the rapidity gap events is plotted separately as closed points. The histograms in Figures 32 and 33 display the cross sections from the POMPYT and NIKZAK simulations, respectively. The dashed histograms show the cross sections obtained by adding the LEPTO and either the POMPYT or NIKZAK cross sections. The solid histograms show the cross sections obtained solely from either the POMPYT or NIKZAK simulations of the rapidity gap events.

6.2.2 x Distribution

To calculate the differential cross section for photon fragmentation with respect to x , $\log x$ space was divided into 16 bins between $x = 1.4743 \times 10^{-4}$ and $x = 1$. The lower edge of the range of x used is the kinematical lower limit of x given the scattered electron energy and angle selection criteria employed. Above $\log x = -3.75$ or $x = 1.778 \times 10^{-4}$ the bins are evenly spaced in $\log x$ space, each being $1/4$ unit in width. All events in which photon fragmentation was observed were binned according to their x values. In each bin the differential cross section, $d\sigma/dx$, was calculated according to the formula

$$\frac{d\sigma}{dx} = \left(\sum_i \frac{w_i}{\mathcal{L}} \right) \frac{1}{\Delta x},$$

where w_i is the event weight of the i^{th} event in the bin, Δx is the width of the bin, and the summation runs over all events in the bin. The error on the differential cross section in each bin was assigned the value $(d\sigma/dx)(1/\sqrt{N_{obs}})$, where N_{obs} is the number of events observed in the bin. In Figures 34 and 35 the experimental determination of $d\sigma/dx$ versus x is plotted as points. The open points show the photon fragmentation cross section, and the contribution to this cross section from the rapidity gap events is plotted separately as closed points. The histograms in Figures 34 and 35 display the cross sections from the POMPYT and NIKZAK

simulations, respectively. The dashed histograms show the cross sections obtained by adding the LEPTO and either the POMPYT or NIKZAK cross sections. The solid histograms show the cross sections obtained solely from either the POMPYT or NIKZAK simulations of the rapidity gap events.

6.2.3 $m_{\gamma^*}^2$ Distribution

All hadrons in the photon fragmentation region collectively form the photon fragmentation system. For each event the invariant mass of this system, $m_{\gamma^*}^2$, is calculated using the four-momentum of all hadrons in the photon fragmentation system as follows:

$$m_{\gamma^*}^2 = \left(\sum_i E_i \right)^2 - \left(\sum_i \vec{p}_i \right)^2,$$

where E_i is the energy of the i^{th} hadron, \vec{p}_i is the momentum of the i^{th} hadron, and the summation runs over all hadrons in the photon fragmentation system.

To calculate the differential cross section for photon fragmentation with respect to $m_{\gamma^*}^2$, equally spaced bins in $\log m_{\gamma^*}^2$ space, each 1/5 unit in width, were used. All events in which photon fragmentation was observed were binned according to their $m_{\gamma^*}^2$ values. In each bin the differential cross section, $d\sigma/dm_{\gamma^*}^2$, was calculated according to the formula

$$\frac{d\sigma}{dm_{\gamma^*}^2} = \left(\sum_i \frac{w_i}{\mathcal{L}} \right) \frac{1}{\Delta m_{\gamma^*}^2},$$

where w_i is the event weight of the i^{th} event in the bin, $\Delta m_{\gamma^*}^2$ is the width of the bin, and the summation runs over all events in the bin. The error on the differential cross section in each bin was assigned the value $(d\sigma/dm_{\gamma^*}^2)(1/\sqrt{N_{obs}})$, where N_{obs} is the number of events observed in the bin. In Figures 36 and 37 the experimental determination of $d\sigma/dm_{\gamma^*}^2$ versus $m_{\gamma^*}^2$ is plotted as points. The open points show the photon fragmentation cross section, and the contribution to this cross section from the rapidity gap events is plotted separately as closed points. The histograms in Figures 36 and 37 display the cross sections obtained from the POMPYT and NIKZAK simulations, respectively.

6.2.4 P_t Distribution

The CMS transverse momentum with respect to the incident virtual photon, P_t , was calculated for each hadron as $P_t = E_h \sin \theta_{\gamma h}$, where E_h is the hadron energy in the CMS and $\theta_{\gamma h}$ is the hadron angle with respect to the virtual photon direction in the CMS. To calculate the invariant cross section, $Ed^3\sigma/d\vec{p}^3$, equally spaced bins in $\log P_t$ space, each 1/4 unit in width, were used. The form of the invariant cross section used was

$$E \frac{d^3\sigma}{d\vec{p}^3} = \frac{d\sigma}{2\pi E dP_t},$$

which includes an average over the azimuthal angle and an integration over the polar angle of the hadron. All hadrons in the photon fragmentation region were binned according to their values of P_t . In each bin the invariant cross section was calculated according to the formula:

$$E \frac{d^3\sigma}{d\vec{p}^3} = \frac{1}{2\pi} \left(\sum_i \frac{w_i}{\mathcal{L}} \cdot \frac{1}{N_i^h} \cdot \frac{1}{E_i} \right) \frac{1}{\Delta P_t},$$

where w_i is the event weight of the event in which the i^{th} hadron appeared, N_i^h is the total number of hadrons in the event in which the i^{th} hadron appeared, E_i is the CMS energy of the i^{th} hadron, and ΔP_t is the width of the bin. The summation runs over all hadrons in the bin. The error on the invariant cross section in each bin was assigned the value $(Ed^3\sigma/d\vec{p}^3)(1/\sqrt{N_{obs}})$, where N_{obs} is the number of hadrons observed in the bin. In Figures 38 and 39 the experimental determination of $Ed^3\sigma/d\vec{p}^3$ versus P_t is plotted as points. The open points show the photon fragmentation cross section, and the contribution to this cross section from the rapidity gap events is plotted separately as closed points. The histograms in Figures 38 and 39 display the cross sections obtained from the POMPYT and NIKZAK simulations, respectively.

6.2.5 T Distribution

The pomeron model predicts a sharp distribution of the four-momentum squared carried by the pomeron, t . For instance, in Ingelman's model the differential cross section with respect to $|t|$, $d\sigma/d|t|$, should behave like the following expression:

$$[F_1(t)]^2 \left(\frac{1}{x_P} \right)^{2\alpha(t)-1},$$

where x_P is the fraction of the proton's momentum carried by the pomeron, and $\alpha(t)$ is the Regge parameter represented approximately by the expression $(1 + 0.085 + 0.25t)$ [45]. In the above expression the factor $F_1(t)$ is a dipole-like form factor of the proton, and the second factor is a Regge "shrinkage" factor which strongly suppresses the distributions at large values of $|t|$.

An experimental measurement of t would entail measuring the four-momentum of all remnant hadrons from the proton. Any remnant hadrons staying in the beam pipe undetected make an experimental measurement of t intractable.

It is possible, however, to calculate the four-momentum transfer squared to the virtual photon. This is done by identifying the photon fragmentation hadrons in each event. The four-momentum transfer squared to the virtual photon is then calculated according to the formula

$$T = \left(E_{\gamma^*} - \sum_i E_i \right)^2 - \left(\vec{q} - \sum_i \vec{p}_i \right)^2,$$

where E_{γ^*} and \vec{q} are the energy and momentum of the virtual photon, E_i and \vec{p}_i are the energy and momentum of the i^{th} hadron, and the summation runs over all hadrons in the event which lie in the photon fragmentation region. T is a negative number; therefore, for cross section calculations $|T|$ was used instead.

To calculate the differential cross section for the rapidity gap process with respect to $|T|$, equally spaced bins in $\log |T|$ space, each $1/3$ unit in width, were used. All rapidity gap events were binned according to their $|T|$ values. In each bin the cross section was calculated according to the formula:

$$\frac{d\sigma}{d|T|} = \left(\sum_i \frac{w_i}{\mathcal{L}} \right) \frac{1}{\Delta|T|},$$

where w_i is the event weight of the i^{th} event, $\Delta|T|$ is the width of the bin, and the summation runs over all events in the bin. The error on the differential cross section in each bin was assigned the value $(d\sigma/d|T|)(1/\sqrt{N_{obs}})$, where N_{obs} is the number of events observed in the bin. In Figures 40 and 41 the experimental determination of $d\sigma/d|T|$ versus $|T|$ for the rapidity gap events is plotted as points. The histograms in Figures 40 and 41 display the cross sections from the POMPYT and NIKZAK simulations, respectively.

6.2.6 β Distribution

A dimensionless variable, $\beta \equiv Q^2/(Q^2 + m_{\gamma^*}^2)$, was used to study the physics of the rapidity gap process. To calculate the quantity $\beta d\sigma/d\beta$, β space was divided into equally spaced bins each 0.1 unit in width. All rapidity gap events were binned according to their β values. In each bin $\beta d\sigma/d\beta$ was calculated according to the formula:

$$\beta \frac{d\sigma}{d\beta} = \left(\sum_i \beta_i \frac{w_i}{\mathcal{L}} \right) \frac{1}{\Delta\beta},$$

where β_i is the value of β in the i^{th} event, w_i is the event weight of the i^{th} event, $\Delta\beta$ is the width of the bin, and the summation runs over all events in the bin. The error on $\beta d\sigma/d\beta$ in each bin was assigned the value $(\beta d\sigma/d\beta)(1/\sqrt{N_{obs}})$, where N_{obs} is the number of events observed in the bin. In Figures 42 and 43 the experimental determination of $\beta d\sigma/d\beta$ versus β for the rapidity gap events is plotted as points. The histograms in Figures 42 and 43 display the cross sections from the POMPYT and NIKZAK simulations, respectively.

Chapter 7

Physics Results and Conclusions

7.1 Summary

In the previous chapter it was demonstrated for the first time that the rapidity gap exists for the final state hadrons in electron-proton scattering. The rapidity gap events were identified as a subset of the events in which virtual photon fragmentation was observed. The experimental cross sections for virtual photon fragmentation and the contribution to these cross sections from the rapidity gap process were presented in the previous chapter. Two sets of theoretical cross sections, both based on the assumption that the rapidity gap events are produced by pomeron exchange, were plotted alongside the experimental results. Now we turn to the question of what can be learned from these distributions.

7.2 Physics Results

The plots of $d\sigma/dQ^2$ versus Q^2 and $d\sigma/dx$ versus x show the Q^2 and x dependence, respectively, of the virtual photon fragmentation and rapidity gap processes. Apart from the difference in magnitude, there is nothing which distinguishes the Q^2 and x spectra of the rapidity gap process from the Q^2 and x spectra of the virtual photon fragmentation process.

There have been previous experiments on proton-proton diffractive scattering [46, 47], $p + p \rightarrow X + p$, and proton-deuteron diffractive scattering [48], $p + d \rightarrow X + d$. One thing these experiments have focussed on is the measurement of the invariant mass, M_X , of the diffractive system X . These experiments have shown [48] that the low-mass end of the M_X^2 spectrum possesses a structure indicative of resonance production. The high-mass end of the M_X^2 spectrum has been observed to follow a M_X^{-2} dependence [46, 48]. Regge theory, using pomeron exchange, has been successfully applied in these experiments to reproduce the observed M_X^{-2} dependence of the high-mass end of the spectra. The plots of $d\sigma/dm_{\gamma^*}^2$ presented in the previous chapter show that the $m_{\gamma^*}^2$ spectrum observed in the ZEUS experiment possesses neither the resonance production structure at the low-mass end of the spectrum nor the M_X^{-2} type dependence at the high-mass end of the spectrum as was observed in proton-proton and proton-deuteron diffractive scattering experiments. The high-mass end of the $m_{\gamma^*}^2$ spectrum in the ZEUS experiment was in fact found to follow approximately a $m_{\gamma^*}^{-4}$ dependence.

The plots of the invariant cross section show the P_t spectrum of the hadrons in the photon fragmentation region. The shape of the P_t spectrum for the virtual photon fragmentation process is similar to that of the rapidity gap process. If the areas under the two curves are each normalized to unity and the normalized curves are plotted on the same graph, it is found that the two curves virtually lie on top of one another. Therefore, aside from its absolute magnitude, nothing about the P_t spectrum of the rapidity gap process distinguishes it from the P_t spectrum of the virtual photon fragmentation process.

The plots of $d\sigma/d|T|$ for the rapidity gap process are particularly enlightening. The ZEUS data exhibit a broad $|T|$ spectrum with large values of $|T|$. On the other hand, built into the pomeron models is a sharp $|t|$ distribution, t being the four-momentum carried by the pomeron, and in these models large values of $|t|$ are strongly suppressed. The POMPYT and NIKZAK simulated data, which were

processed and analyzed using the same method as for the experimental data, also exhibited a broad $|T|$ spectrum containing large values of $|T|$. Therefore, it must be that the T used in the analysis here is not equivalent to the t used in the pomeron models. In other words, the four-momentum transfer squared at the photon vertex is not equal to the four-momentum transfer squared at the proton vertex. This fact indicates that there are unobserved hadrons which remain in the beam pipe, a typical behavior of the multiperipheral production process.

Bjorken has proposed a “hard diffraction” model [49] to explain the existence of the rapidity gap events. In this model the virtual photon pair produces a Bethe-Heitler type of quark-antiquark pair. The rapidity gap events are produced when either quark or antiquark carries most of the momentum of the parent virtual photon. This “fast” quark is referred to as the current quark, since it carries most of the momentum of the virtual photon current. The other “slow” quark is referred to as the constituent quark, and it will be essentially at rest. The square of the amplitude for this process would take the form of a ladder diagram, the rungs and rails of which would be composed of pions. The bottom of the ladder, where the proton line is, would consist of two pions, which would essentially appear to the proton as a ρ^0 particle. Thus, the proton would interact with a slow ρ^0 particle, which would be a non-perturbative situation. Since the proton essentially interacts with a ρ^0 particle, this model bears some resemblance to the vector dominance models of photon-proton interactions.

The hard diffraction model expects that the $\beta d\sigma/d\beta$ curve should level off to a constant non-zero value at low values of β . The plots of $\beta d\sigma/d\beta$ show that such a behavior was not observed in the data. One could argue that the analysis technique employed here would not see the low end of the β spectrum. The contrary was found to be true when the simulation data of the NIKZAK model were used.

7.3 Conclusions

The differential cross sections presented in this dissertation provide a basic description of the physics of virtual photon fragmentation. The most interesting observation which has been made is of the existence of events with a rapidity gap, which here have been considered to be a subset of all events where virtual photon fragmentation is observed. In comparing the virtual photon fragmentation spectra with the rapidity gap spectra it was found that, apart from their absolute magnitudes, there is nothing which distinguishes the two.

In general, the shapes of the spectra obtained from the POMPYT and NIKZAK Monte Carlo simulations reproduced the shapes of the experimental spectra of the rapidity gap process well. One problem with these models, especially pronounced in the NIKZAK simulation, is that the flux normalization was wrong by a large factor.

The most crucial test of the pomeron models came with the $|T|$ spectrum. It was found that the sharp momentum transfer at the proton vertex was impossible to observe at the photon vertex due to the fact that unobserved hadrons remained in the beam pipe. The sharp t distribution is the most characteristic trait of the pomeron models, and it has been found that it is impossible at this time to make an observation of this quantity. Therefore, the fact that the simulated spectra match the experimental spectra is not a clear cut proof of the physical reality of the pomeron model.

If the broad $|T|$ spectrum exhibited by the ZEUS data is due to the presence of unobserved hadrons in the beam pipe it is conceivable that the rapidity gap events are a manifestation of a multiperipheral production process. Perhaps diffraction dissociation of the proton or excitation of the proton into higher mass states is involved in these events as well.

The alternative to the pomeron models is the hard diffraction model of Bjorken. The low- β events expected in this model were not found in the experimental data, however.

Only complete measurements of the backward-going system (with respect to the virtual photon direction) can give the necessary information on the rapidity gap events. Such measurements, while very difficult, would provide the data needed to determine whether the rapidity gap events are caused by the elastic scattering of the proton by the emission of a pomeron with which the virtual photon interacts, or whether such processes as multiperipheral production, diffraction dissociation, or excitation of the proton into higher mass states are involved.

The ZEUS detector will be outfitted with forward detection components (with respect to the ZEUS coordinate system) in future experimental runs in order to attempt these measurements. Data from these detectors is anticipated in the hopes of gaining a more complete understanding of the rapidity gap events.

Appendix A

Cross Sections for Deep Inelastic Scattering

A.1 Conventions for Four-momenta and Units

In this Appendix k is defined as the four-momentum of incident electron, k' is defined as the four-momentum of scattered electron, p is defined as the four-momentum of incident proton, q is defined as $q \equiv k - k'$, and $Q^2 = -q^2$. In the frame provided by HERA, using the ZEUS coordinate system introduced in Section 2.2.1.3, these four-momenta are as follows:

$$k = (E_e, 0, 0, k_{ze}), \quad k' = (E'_e, k'_{xe}, k'_{ye}, k'_{ze}), \quad \text{and} \quad p = (E_p, 0, 0, p_{zp}),$$

where the first component is the energy, and the last three components are the x , y , and z components of momentum, respectively. The energy of the scattered electron is denoted by E'_e and its polar scattering angle by θ_e . Throughout this dissertation we adopt the conventional units of $\alpha = e^2/4\pi$ and setting \hbar and c to unity.

A.2 Cross Section for Single Photon Exchange

The formula for the differential cross section is

$$d\sigma = \frac{|M|^2}{4\sqrt{(p \cdot k)^2 - M_p^2 m_e^2}} (2\pi)^4 \delta^4 \left(k + p - k' - \sum_i p'_i \right) \frac{d^3 \vec{k}'}{(2\pi)^3 2E'_e} \prod_i \frac{d^3 \vec{p}'_i}{(2\pi)^3 2E'_i} \left(\frac{1}{2} \right) \left(\frac{1}{2} \right),$$

where $p'_i = (E'_i, \vec{p}'_i)$ is the four-momentum of the i^{th} final state hadron, and the product and summation run over all final state hadrons. The quantity $|M|^2$ is the square of the matrix element for deep inelastic electron-proton scattering. It includes a summation over the spin states of the initial state electron and initial state proton as well as a summation over the spin states of all final state particles. The two factors of $1/2$ at the end of the expression for $d\sigma$ are present in order to average over the spin states of the initial state electron and initial state proton, and thus to make the cross section that for unpolarized beams.

The square of the matrix element can be expressed as

$$|M|^2 = \left(\frac{e^2}{Q^2} \right)^2 L_{\mu\nu} W^{\mu\nu},$$

where $L_{\mu\nu}$ is the lepton tensor and $W^{\mu\nu}$ is the hadron tensor. By convention, for deep inelastic scattering the factors

$$\int (2\pi)^3 \delta^4 \left(k + p - k' - \sum_i p'_i \right) \prod_i \frac{d^3 \vec{p}'_i}{(2\pi)^3 2E'_i} \left(\frac{1}{2} \right) \left(\frac{1}{2M_p} \right)$$

are absorbed into $W^{\mu\nu}$, which allows the differential cross section to be re-expressed as

$$d\sigma = \frac{4\pi M_p |M|^2}{8p \cdot k} \frac{d^3 \vec{k}'}{(2\pi)^3 2E'_e},$$

having neglected M_p and m_e .

The lepton tensor is symmetric and is expressed as

$$L_{\mu\nu} = 4(k_\mu k'_\nu + k_\nu k'_\mu - g_{\mu\nu} k \cdot k'),$$

where

$$g_{00} = 1; \quad g_{11} = g_{22} = g_{33} = -1; \quad g_{\mu\nu} = 0, \quad \mu \neq \nu.$$

A general form for the hadron tensor must be constructed from kinematics by relying on the principles of Lorentz invariance and current conservation. Mathematically, the principle of current conservation can be expressed as $q_\mu W^{\mu\nu} = q_\nu W^{\mu\nu} = 0$. The two independent four-momenta p^μ and q^μ are utilized to construct the most general form of the hadron tensor as

$$W^{\mu\nu} = V_1 g^{\mu\nu} + V_2 p^\mu p^\nu + V_3 (p^\mu q^\nu + p^\nu q^\mu) + V_4 q^\mu q^\nu + V_5 (p^\mu q^\nu - p^\nu q^\mu),$$

where V_1, V_2, V_3, V_4 , and V_5 are real (since $W^{\mu\nu}$ is Hermitian), invariant functions of the kinematic variables.

With this form of $W^{\mu\nu}$ the current conservation equations become

$$\begin{aligned} V_1 q^\nu + V_2 p \cdot q p^\nu + V_3 (p \cdot q q^\nu + q^2 p^\nu) + V_4 q^2 q^\nu + V_5 (p \cdot q q^\nu - q^2 p^\nu) &= 0, \text{ and} \\ V_1 q^\mu + V_2 p \cdot q p^\mu + V_3 (p \cdot q q^\mu + q^2 p^\mu) + V_4 q^2 q^\mu + V_5 (q^2 p^\nu - p \cdot q q^\nu) &= 0. \end{aligned}$$

For these equations to be identical, as they must be, we must set $V_5 = 0$. The four-vectors p^μ and q^μ are independent; therefore, their coefficients must vanish separately. This leads to the two equations

$$\begin{aligned} V_2 p \cdot q + V_3 q^2 &= 0, \text{ and} \\ V_1 + V_3 p \cdot q + V_4 q^2 &= 0. \end{aligned}$$

These two equations are used to eliminate V_3 and V_4 in the expression for $W^{\mu\nu}$. Thus, there are really only two independent quantities, V_1 and V_2 , and the following assignments are made: $V_1 = -W_1$ and $V_2 = W_2/M_p^2$. With all substitutions completed the expression for $W^{\mu\nu}$ becomes

$$W^{\mu\nu} = -W_1 \left(g^{\mu\nu} - \frac{q^\mu q^\nu}{q^2} \right) + \frac{W_2}{M_p^2} \left(p^\mu - \frac{p \cdot q}{q^2} q^\mu \right) \left(p^\nu - \frac{p \cdot q}{q^2} q^\nu \right). \quad (\text{A.1})$$

The two Lorentz invariant functions W_1 and W_2 remain as parameters to be determined by experiment.

Because current conservation is satisfied at the lepton vertex, $q_\mu L^{\mu\nu} = q_\nu L^{\mu\nu} = 0$, when the contraction $L_{\mu\nu} W^{\mu\nu}$ is performed the only terms in $W^{\mu\nu}$ which will

contribute are $-W_1 g^{\mu\nu}$ and $(W_2/M_p^2)p^\mu p^\nu$. Thus, we have for the contraction of $L_{\mu\nu}$ and $W^{\mu\nu}$

$$\begin{aligned} L_{\mu\nu} W^{\mu\nu} &= 4(k_\mu k'_\nu + k_\nu k'_\mu - g_{\mu\nu} k \cdot k') \left[-W_1 g^{\mu\nu} + \frac{W_2}{M_p^2} p^\mu p^\nu \right] \\ &= 4 \left[W_1 (2k \cdot k') + \frac{W_2}{M_p^2} (2k \cdot p k' \cdot p - M_p^2 k \cdot k') \right] \\ &= 4 \left[W_1 Q^2 + \frac{W_2}{2} \left(\frac{4k \cdot p k' \cdot p - M_p^2 Q^2}{M_p^2} \right) \right], \end{aligned}$$

where we have used the relation $k \cdot k' = -q^2/2 = Q^2/2$, which neglects the electron mass. This result is expressed in frame invariant form. Specializing to the HERA frame involves calculation of the following quantities:

$$k \cdot p = 2E_e E_p, \quad k' \cdot p = 2E_p E'_e \sin^2 \frac{\theta_e}{2}, \quad Q^2 = 4E_e E'_e \cos^2 \frac{\theta_e}{2},$$

where both the electron and proton masses have been neglected. The result for $L_{\mu\nu} W^{\mu\nu}$ in the HERA frame is thus

$$\begin{aligned} L_{\mu\nu} W^{\mu\nu} &= 4 \left[W_1 \left(4E_e E'_e \cos^2 \frac{\theta_e}{2} \right) \right. \\ &\quad \left. + \frac{W_2}{2} \left(\frac{4(2E_e E_p)(2E_p E'_e \sin^2 \frac{\theta_e}{2}) - M_p^2 (4E_e E'_e \cos^2 \frac{\theta_e}{2})}{M_p^2} \right) \right] \\ &\simeq 32 \left(\frac{E_p^2}{M_p^2} \right) E_e E'_e \sin^2 \frac{\theta_e}{2} \left[W_1 \left(\frac{M_p^2}{2E_p^2} \cot^2 \frac{\theta_e}{2} \right) + W_2 \right], \end{aligned}$$

where the $M_p^2(4E_e E'_e \cos^2 \frac{\theta_e}{2})$ term in the coefficient of W_2 has been neglected since $E_p \gg M_p$. The square of the matrix element for deep inelastic electron-proton scattering in the HERA frame is thus

$$|M|^2 = \left(\frac{e^2}{4E_e E'_e \cos^2 \frac{\theta_e}{2}} \right)^2 32 \left(\frac{E_p^2}{M_p^2} \right) E_e E'_e \sin^2 \frac{\theta_e}{2} \left[W_1 \left(\frac{M_p^2}{2E_p^2} \cot^2 \frac{\theta_e}{2} \right) + W_2 \right].$$

Substituting for $|M|^2$ and $(p \cdot k)$ in the differential cross section formula, and letting $d^3 \vec{k}' = E_e'^2 dE'_e d\Omega$, where $d\Omega$ is the element of solid angle into which the electron scatters, we obtain

$$d\sigma = \frac{4\pi M_p \left(\frac{e^2}{4E_e E'_e \cos^2 \frac{\theta_e}{2}} \right)^2 32 \left(\frac{E_p^2}{M_p^2} \right) E_e E'_e \sin^2 \frac{\theta_e}{2} \left[W_1 \left(\frac{M_p^2}{2E_p^2} \cot^2 \frac{\theta_e}{2} \right) + W_2 \right] E_e'^2 dE'_e d\Omega}{8(2E_e E_p) (2\pi)^3 2E'_e}.$$

After simplifying and dividing through by $dE'_e d\Omega$ we obtain

$$\frac{d^2\sigma}{dE'_e d\Omega} = \left(\frac{\alpha^2 E_p \sin^2 \frac{\theta_e}{2}}{2M_p E_e^2 \cos^4 \frac{\theta_e}{2}} \right) \left[W_1 \left(\frac{M_p^2}{2E_p^2} \cot^2 \frac{\theta_e}{2} \right) + W_2 \right].$$

The quantity in parentheses is referred to as the Mott cross section. It is the cross section for the scattering of a point-like, spin-1/2 electron from a structureless proton:

$$\left(\frac{d\sigma}{d\Omega} \right)_{Mott} = \left(\frac{\alpha^2 E_p \sin^2 \frac{\theta_e}{2}}{2M_p E_e^2 \cos^4 \frac{\theta_e}{2}} \right).$$

This identification allows the differential cross section to be written as

$$\frac{d^2\sigma}{dE'_e d\Omega} = \left(\frac{d\sigma}{d\Omega} \right)_{Mott} \left[W_1 \left(\frac{M_p^2}{2E_p^2} \cot^2 \frac{\theta_e}{2} \right) + W_2 \right]. \quad (\text{A.2})$$

The form of $W^{\mu\nu}$ used to derive this result is the general form for the electromagnetic interaction of single photon exchange. When the weak interaction of Z^0 exchange is included $W^{\mu\nu}$ must be modified and another function W_3 , which must also be determined experimentally, is introduced. At low Q^2 the electromagnetic interaction is dominant. However, as Q^2 increases the effects of the weak interaction become more pronounced until eventually they dominate at high Q^2 .

At low values of Q^2 the product νW_2 was observed to follow a scaling behavior [4]. This means that at fixed values of the variable x , the product νW_2 is independent of Q^2 . (The variables Q^2 , ν , and x are discussed in Appendix B). This lead to the following traditional assignments:

$$F_2 \equiv \nu W_2, \text{ and}$$

$$F_1 \equiv M_p W_1.$$

F_1 and F_2 are referred to as the structure functions of the proton. Scaling violations of F_2 , a non-exhaustive list of which can be found in [50], have since been well documented. Working in the infinite momentum frame of the proton, the Callan-Gross relation [51], $F_2 = 2xF_1$, relates F_1 and F_2 and is a consequence of assuming that the quarks are spin-1/2 particles.

A.3 Electroweak Neutral Current Electron-Proton Scattering Cross Section

Experiment has proven that the proton, indeed all hadrons, consists of quarks and gluons. The six quark “flavors” (labelled u , d , c , s , t , and b) and their corresponding antiquarks are sufficient to explain the observed hadron spectroscopy. Each quark comes in one of three “colors”, and the quarks combine in such a way that all hadrons are color singlets, i.e., colorless. Protons consist of three valence quarks (two u quarks and one d quark) and sea quarks, which are quark-antiquark pairs. The quarks interact by the exchange of gluons, which carry color as well. When the quarks are within the proton at small distances they behave like free particles. However, in attempting to remove a quark the gluons act as a strong force to confine the quark within the proton.

The analysis of the proton structure is very physical if performed in the frame in which the momentum of the proton is infinite, so that all masses and momenta transverse to the direction of travel of the proton may be neglected. In this frame, the fraction of the proton’s momentum carried by any individual quark or gluon is denoted by the variable x . The parton distribution functions are the momentum distributions of a given quark flavor or the gluons within the proton. In this Appendix the parton distribution functions are written $q_f(x)$, $\bar{q}_f(x)$, and $g(x)$. The quantity $q_f(x)dx$ is the probability of finding a quark of flavor f carrying a fraction of the proton’s momentum between x and $x + dx$. The quantity $\bar{q}_f(x)dx$ is the probability of finding an antiquark of flavor f carrying a fraction of the proton’s momentum between x and $x + dx$. The quantity $g(x)dx$ is the probability of finding a gluon carrying a fraction of the proton’s momentum between x and $x + dx$.

The fundamental understanding of electron-proton scattering is provided by electroweak theory, which is an integral portion of the standard model. In the standard model all matter consists of fermions: six leptons, six quarks, and their correspond-

ing antileptons and antiquarks. The forces between these particles are mediated by bosons. The lepton-lepton and lepton-quark interactions are mediated by photons, Z^0 bosons, and W^\pm bosons. Quark-quark interactions are mediated by photons, Z^0 bosons, W^\pm bosons, and the eight colored gluons. Since gluons carry color they can interact amongst themselves as well.

In the standard model the particle masses are generated by the introduction of a Higgs boson followed by application of spontaneous symmetry breaking of a local gauge symmetry. As a result, the Z^0 boson obtains a heavy mass while the photon remains massless. The physical fields representing the photon and Z^0 are mixed. This mixing is described by the Weinberg angle, θ_W . The mass of the Z^0 boson, M_Z , and the Weinberg angle are both experimental parameters of the standard model. They have been measured to be $M_Z = 91.187 \pm 0.007$ GeV [52] and $\sin^2 \theta_W = 0.2256 \pm 0.0023$ [53]. (Over the past years, the mean value of $\sin^2 \theta_W$ has been varying between values far beyond the experimental errors.)

In electroweak theory electron-proton scattering is regarded as the interaction of the incident electron with a single quark within the proton. Since when they are within the proton the quarks can be treated as free particles, the complete electron-proton scattering cross section is then the summation of the cross sections for the electron to scatter from all the quarks within the proton. Presented in this section is the cross section for the neutral current interaction, $e + p \rightarrow e' + X$, in which the electron exchanges either a photon or a Z^0 with a quark. Charged current interactions also exist, $e + p \rightarrow \nu_e + X$, in which the electron exchanges a W^- with a quark and the outgoing lepton is a neutrino.

For unpolarized beams, the neutral current electroweak electron-proton scattering cross section in terms of the variables x and y (see Appendix B) is

$$\frac{d^2\sigma}{dx dy} = \frac{\pi\alpha^2}{2sx^2y^2} \left\{ \sum_f (xq_f + x\bar{q}_f) A_f [1 + (1-y)^2] + \sum_f (xq_f - x\bar{q}_f) B_f [1 - (1-y)^2] \right\}.$$

The quantities A_f and B_f are defined as follows:

$$A_f = \lambda_V^{e\gamma\gamma} \lambda_V^{f\gamma\gamma} + 2\lambda_V^{e\gamma Z} \lambda_V^{f\gamma Z} \frac{Q^2}{Q^2 + M_Z^2} + \lambda_V^{eZZ} \lambda_V^{fZZ} \left(\frac{Q^2}{Q^2 + M_Z^2} \right)^2, \text{ and}$$

$$B_f = \lambda_A^{e\gamma\gamma} \lambda_A^{f\gamma\gamma} + 2\lambda_A^{e\gamma Z} \lambda_A^{f\gamma Z} \frac{Q^2}{Q^2 + M_Z^2} + \lambda_A^{eZZ} \lambda_A^{fZZ} \left(\frac{Q^2}{Q^2 + M_Z^2} \right)^2.$$

In both A_f and B_f the first term is the coefficient arising from single photon exchange, the middle term is the coefficient arising from photon- Z^0 interference, and the final term is the coefficient arising from single Z^0 exchange. The quantities λ_V^{eij} , λ_V^{fij} , λ_A^{eij} , and λ_A^{fij} are functions of the fermion-boson coupling constants:

$$\begin{aligned} \lambda_V^{eij} &= 2(v_e^i v_e^j + a_e^i a_e^j); \\ \lambda_A^{eij} &= 2(v_e^i a_e^j + a_e^i v_e^j); \\ \lambda_V^{fij} &= 2(v_f^i v_f^j + a_f^i a_f^j); \\ \lambda_A^{fij} &= 2(v_f^i a_f^j + a_f^i v_f^j); \\ i, j &= \gamma, Z. \end{aligned}$$

The quantities v_e^γ and v_f^γ are the vector coupling constants of the photon to the electron and quark flavor f , respectively, which in the electroweak theory is given by the negative of the fermion charge. Therefore,

$$v_e^\gamma = 1, \text{ and } v_f^\gamma = \begin{cases} -2/3 & f = u, c, t \\ 1/3 & f = d, s, b. \end{cases}$$

The quantities a_e^γ and a_f^γ are the axial-vector coupling constants of the photon to the electron and quark flavor f , respectively. In electroweak theory there is no axial vector coupling to the photon; therefore, $a_e^\gamma = a_f^\gamma = 0$ for all f .

The quantities v_e^Z and v_f^Z are the vector coupling constants of the Z^0 boson to the electron and quark flavor f , respectively. They are expressed in terms of the third component of isospin, I^3 , and fermion charge, Q , as

$$v_e^Z = \frac{I_e^3 - 2Q_e s_W^2}{2s_W c_W}, \text{ and } v_f^Z = \frac{I_f^3 - 2Q_f s_W^2}{2s_W c_W}.$$

The following data apply:

$$I_e^3 = -1/2, \quad I_f^3 = \begin{cases} 1/2 & f = u, c, t \\ -1/2 & f = d, s, b, \end{cases}$$

$$Q_e = -1, \quad Q_f = \begin{cases} 2/3 & f = u, c, t \\ -1/3 & f = d, s, b. \end{cases}$$

The quantities s_W and c_W are the sine and cosine, respectively, of the Weinberg angle.

Finally, the quantities a_e^Z and a_f^Z are the axial vector coupling constants of the Z^0 boson to the electron and quark flavor f , respectively. In electroweak theory these are expressed as

$$a_e^Z = \frac{I_e^3}{2s_W c_W}, \text{ and } a_f^Z = \frac{I_f^3}{2s_W c_W},$$

where I_e^3 and I_f^3 are the same as above.

The reason for the presence of the factors $[1 \pm (1 - y)^2]$ can be understood when the electron-quark interaction is viewed in the center-of-mass of the electron-quark system. In this frame, $1 - y = (1 + \cos \theta^*)/2$, where θ^* is the center-of-mass scattering angle.

The cross section above is for unpolarized beams. The initial state electron can thus either have helicity $+1$ or helicity -1 . If the electron interacts with a quark of the same helicity, then the total z component of angular momentum is zero. Since (1) the helicity of both electron and quark are conserved in the interaction, and (2) the total z component of angular momentum is also conserved in the interaction, there will be no restriction on the scattering angle θ^* and the scattering will be isotropic. The first term of unity in the expression $[1 \pm (1 - y)^2]$ therefore represents the isotropic nature of the scattering between an electron and a quark of the same helicity in their center-of-mass frame.

On the other hand, if the electron interacts with a quark of the opposite helicity then the total z component of angular momentum will be ± 1 . Since both electron and quark helicities are conserved, backscattering ($\theta^* = 180^\circ$) is therefore prevented on the basis of angular momentum conservation. Since the expression $(1 + \cos \theta^*)$ falls to zero at $\theta^* = 180^\circ$, the factor $(1 - y)$ has the effect of suppressing the cross section for backscattering between an electron and quark of opposite helicities in their center-of-mass frame.

A.4 Cross Sections for the Absorption of Longitudinally and Transversely Polarized Virtual Photons

The analysis of electron-proton scattering in terms of the absorption of longitudinally and transversely polarized virtual photons was first performed by L. Hand [54].

In the rest frame of the proton, the differential electron-proton deep inelastic cross section, expressed in terms of the structure functions W_1 and W_2 as introduced in Section A.2, is

$$\frac{d^2\sigma}{dE'_e d\Omega} = \left(\frac{d\sigma}{d\Omega} \right)_{Mott} \left[W_2 + 2W_1 \tan^2 \frac{\theta_e}{2} \right],$$

where

$$\left(\frac{d\sigma}{d\Omega} \right)_{Mott} = \frac{\alpha^2}{4E_e^2} \frac{\cos^2 \frac{\theta_e}{2}}{\sin^4 \frac{\theta_e}{2}}.$$

The meanings of E_e , E'_e , and θ_e in these equations are different than those used above. Here they represent the incident electron energy, scattered electron energy, and scattered electron angle, respectively, in the rest frame of the proton. The scattered electron angle, θ_e , here is measured with respect to the incident electron direction.

The differential cross section can also be expressed in terms of σ_L , the cross section for the absorption of longitudinally polarized virtual photons (which also contains the contribution from scalar photons), and σ_T , the cross section for the absorption of transversely polarized virtual photons. This takes the form

$$\frac{d^2\sigma}{dE'_e d\Omega} = \Gamma_t [\sigma_T + \epsilon\sigma_L],$$

where

$$\begin{aligned}\Gamma_t &= \frac{\alpha}{4\pi^2} \frac{K}{Q^2} \frac{E'_e}{E_e} \left(\frac{2}{1-\epsilon} \right), \text{ and} \\ \epsilon &= \left[1 + 2 \left(1 + \frac{\nu^2}{Q^2} \right) \tan^2 \frac{\theta_e}{2} \right]^{-1}.\end{aligned}$$

The quantity Γ_t is the virtual photon spectrum, ϵ is the polarization parameter, and $K = (W^2 - M_p^2)/2M_p$.

W_1 and W_2 are related to σ_T and σ_L in the following way:

$$\begin{aligned}W_2 &= \frac{K}{4\pi^2\alpha} \left(\frac{Q^2}{Q^2 + \nu^2} \right) (\sigma_T + \sigma_L), \text{ and} \\ W_1 &= \frac{K}{4\pi^2\alpha} \sigma_T.\end{aligned}$$

Experimentally, σ_T and σ_L are extracted at fixed values of Q^2 and W^2 by measuring the quantity $(1/\Gamma_t)(d^2\sigma/dE'_e d\Omega)$ at different values of ϵ . At fixed values of Q^2 and W^2 , the slope of the ‘‘Rosenbluth plot’’ [55] of a straight line, $(1/\Gamma_t)(d^2\sigma/dE'_e d\Omega)$ versus ϵ , gives the value of σ_L , while the intercept at $\epsilon = 0$ gives the value of σ_T .

The quantity R is defined as $R \equiv \sigma_L/\sigma_T$. The value of R should be small if the deep inelastic electron-proton scattering is dominated by the transversely polarized photon. The measurement of R is a tedious task because it requires the variation of the initial beam energies. The best measurements were done systematically at SLAC. The values of R were found to be approximately 0.18 and the variation of these values with respect to Q^2 and W^2 was found to be small. This observation, together with the observation that the ratio of the F_2 functions for the neutron and proton equaled approximately 1/4 at x near unity, indicated that the spin of a quark is 1/2 [7].

W_1 and W_2 can be determined at fixed values of Q^2 and W^2 by measuring $(d\sigma/d\Omega)_{Mott}^{-1} (d^2\sigma/dE'_e d\Omega)$ at different values of $\tan^2(\theta_e/2)$. At fixed values of Q^2 and W^2 the slope of the “Rosenbluth plot” [55] of a straight line, $(d\sigma/d\Omega)_{Mott}^{-1} (d^2\sigma/dE'_e d\Omega)$ versus $\tan^2(\theta_e/2)$, gives the value of $2W_1$, while the intercept at $\tan^2(\theta_e/2) = 0$ gives the value of W_2 . In the ZEUS experiment the extraction of R by variation of the initial beam energies has not yet been attempted. Therefore, separate measurements of the structure functions W_1 and W_2 in the ZEUS experiment have not yet been made. The structure function W_2 has been extracted by making use the SLAC value of R and/or the Callan-Gross relation.

Appendix B

Kinematic Relations in Deep Inelastic Scattering at HERA

In this appendix the same conventions for the incident electron four-momentum k , scattered electron four-momentum k' , and incident proton four-momentum p are followed as were given in Section A.1. M_p will be used to denote the mass of the proton.

In DIS the energy, E'_e , and angle, θ_e , of the scattered electron are independent variables. Therefore, both E'_e and θ_e must be measured in order to fully reconstruct the kinematics of each DIS event.

Five frame invariant kinematic variables, each of which can be expressed in terms of E'_e and θ_e , are important to the analysis of DIS. In this appendix each of these variables will be defined and then expressed in terms of E'_e and θ_e in the HERA frame using the ZEUS coordinates laid out in Section 2.2.1.3. Following that, the physical meaning of each variable will be discussed.

$$Q^2 \equiv -q^2 = -(k - k')^2 \simeq 2k \cdot k' = 4E_e E'_e \cos^2 \frac{\theta_e}{2} \quad (\text{B.1})$$

$$\nu = \frac{p \cdot q}{M_p} = \frac{2E_p}{M_p} \left(E_e - E'_e \sin^2 \frac{\theta_e}{2} \right) \quad (\text{B.2})$$

$$W^2 \equiv (p + q)^2 = M_p^2 + 2p \cdot q + q^2 \simeq 4E_p E_e - 4E_p E'_e \sin^2 \frac{\theta_e}{2} - 4E_e E'_e \cos^2 \frac{\theta_e}{2} \quad (\text{B.3})$$

$$x \equiv \frac{Q^2}{2p \cdot q} = \left(\frac{E_e}{E_p} \right) \frac{E'_e \cos^2 \frac{\theta_e}{2}}{E_e - E'_e \sin^2 \frac{\theta_e}{2}} \quad (\text{B.4})$$

$$y \equiv \frac{p \cdot q}{p \cdot k} = 1 - \frac{E'_e}{E_e} \sin^2 \frac{\theta_e}{2} \quad (\text{B.5})$$

From these relations it is evident that the following relation holds:

$$Q^2 = sxy,$$

where s is the CMS energy squared $s = (p + k)^2 \simeq 2p \cdot k$.

The quantity Q^2 is the negative of the square of the four-momentum transfer between the incident electron and incident proton, or the square of the four-momentum carried by the virtual photon. Q^2 is related to the wavelength of the virtual photon through the Uncertainty Principle. The larger the value of Q^2 is, the smaller is the wavelength of the virtual photon, and smaller wavelengths mean better resolution for probing the proton structure.

The quantity ν is the energy transfer to the incident proton in its rest frame.

The quantity W^2 is the square of the invariant mass of the hadronic final state, which is equivalent to the square of the CMS energy of the virtual photon-proton system.

The variables x and y are scaling variables. Both can only assume values between 0 and 1. In the hypothetical “infinite momentum frame” the incident proton has infinite momentum and hence the masses of all its constituents and any transverse momentum they may have with respect to the direction of travel of the proton can be neglected. In this frame, x is the fraction of the proton’s four-momentum carried by the constituent which was struck by the virtual photon probe.

Finally, the variable y is the fractional energy loss of the electron in the rest frame of the incident proton. This can be seen by evaluating y in the proton rest frame, where it is found that $y = (E_e - E'_e)/E_e$.

In the analysis of this dissertation, the kinematics of all DIS events were constructed by first measuring the energy and angle of the scattered electron. Then each of the variables above was computed according to the formulae given in (B.1) through (B.5).

References

- [1] M. Gell-Mann, “A Schematic Model of Baryons and Mesons.” *Phys. Lett.* **8**, 214 (1964).
- [2] Y. Ne’eman, “Derivation of Strong Interactions from a Gauge Invariance.” *Nucl. Phys.* **26**, 222 (1961).
- [3] O. W. Greenberg, “Spin and Unitary-spin Independence in a Paraquark Model of Baryons and Mesons.” *Phys. Rev. Lett.* **13**, 598 (1964).
- [4] W. K. H. Panofsky, “Low q^2 Electrodynamics, Elastic and Inelastic Electron (and Muon) Scattering.” in *Proceedings of the 14th International Conference on High Energy Physics*, edited by J. Prentki and J. Steinberger, Vienna, 1968, p. 23; M. Briedenbach *et al.*, “Observed Behavior of Highly Inelastic Electron-Proton Scattering.” *Phys. Rev. Lett.* **23**, 935 (1969); G. Miller *et al.*, “Inelastic Electron-Proton Scattering at Large Momentum Transfers and the Inelastic Structure Functions of the Proton.” *Phys. Rev.* **D5**, 528 (1972); J. Friedman and H. Kendall, “Deep Inelastic Electron Scattering.” *Ann. Rev. Nucl. Sci.* **22**, 203 (1972).
- [5] C. N. Yang and R. L. Mills, “Conservation of Isotopic Spin and Isotopic Gauge Invariance.” *Phys. Rev.* **96**, 191 (1954).

- [6] A. Litke *et al.*, “Hadron Production by Electron-Positron Annihilation at 4-GeV Center-of-Mass Energy.” *Phys. Rev. Lett.* **30**, 1189 (1973). The ratio R here should not be confused with another R as defined in reference [4].
- [7] R. P. Feynman, *Photon-Hadron Interactions*, Reading, Massachusetts, Benjamin Publishing Company, 1972, p. 132.
- [8] J. D. Bjorken, “Current Algebra at Small Distances.” in *Proceedings of the International School of Physics “Enrico Fermi”*, edited by J. Steinberger, Varenna, 1967, p. 55. The scaling variable was first introduced by Bjorken as $\omega \equiv 2M_p\nu/Q^2$. The variable x is the inverse of ω .
- [9] J. Kuti and V. F. Weisskopf, “Inelastic Lepton-Nucleon Scattering and Lepton Pair Production in the Relativistic Quark-Parton Model.” *Phys. Rev.* **D4**, 3418 (1971).
- [10] T. Regge, “Introduction to Complex Orbital Momenta.” *Nuovo Cimento* **14**, 951 (1959).
- [11] A. V. Barnes *et al.*, “Pion Charge-Exchange Scattering at High Energies.” *Phys. Rev. Lett.* **37**, 76 (1976).
- [12] S. L. Glashow, Ph.D. dissertation, Harvard University, 1958 (unpublished); A. Salam, invited talk at Nobel Institute, Stockholm, 1964; S. Weinberg, “A Model of Leptons.” *Phys. Rev. Lett.* **19**, 1264 (1967).
- [13] Y. Nambu and G. Jona-Lasinio, “Dynamical Model of Elementary Particles Based on an Analogy with Superconductivity. I.” *Phys. Rev.* **122**, 345 (1961); Y. Nambu and G. Jona-Lasinio, “Dynamical Model of Elementary Particles Based on an Analogy with Superconductivity. II.” *Phys. Rev.* **124**, 246 (1961); J. Goldstone, “Field Theories with ‘Superconductor’ Solutions.” *Nuovo Cimento* **19**, 154 (1961); P. W. Higgs, “Broken Symmetries, Massless Particles

- and Gauge Fields.” *Phys. Lett.* **12**, 132 (1964); P. W. Higgs, “Broken Symmetries and the Masses of Gauge Bosons.” *Phys. Rev. Lett.* **13**, 508 (1964); P. W. Higgs, “Spontaneous Symmetry Breakdown without Massless Bosons.” *Phys. Rev.* **145**, 1156 (1966).
- [14] TASSO Collaboration, R. Brandelik *et al.*, “Evidence for Planar Events in e^+e^- Annihilation at High Energies.” *Phys. Lett.* **B86**, 243 (1979); MARK J Collaboration, D. P. Barber *et al.*, “Discovery of Three-jet Events and a Test of Quantum Chromodynamics at PETRA.” *Phys. Rev. Lett.* **43**, 830 (1979); PLUTO Collaboration, Ch. Berger *et al.*, “Evidence for Gluon Bremsstrahlung in e^+e^- Annihilations at High Energies.” *Phys. Lett.* **B86**, 418 (1979); JADE Collaboration, W. Bartel *et al.*, “Observation of Planar Three-jet Events in e^+e^- Annihilation and Evidence for Gluon Bremsstrahlung.” *Phys. Lett.* **B91**, 142 (1980); MARK II Collaboration, D. Schlatter *et al.*, “Measurement of Energy Correlations in $e^+e^- \rightarrow$ Hadrons.” *Phys. Rev. Lett.* **49**, 521 (1982).
- [15] D. J. Gross and F. Wilczek, “Ultraviolet Behavior of Non-Abelian Gauge Theories.” *Phys. Rev. Lett.* **30**, 1343 (1973); H. D. Politzer, “Reliable Perturbative Results for Strong Interactions?” *Phys. Rev. Lett.* **30**, 1346 (1973); H. D. Politzer, “Asymptotic Freedom: An Approach to Strong Interactions.” *Phys. Rep.* **14C**, 129 (1974).
- [16] A. Chodos, R. L. Jaffe, K. Johnson, C. B. Thorn and V. F. Weisskopf, “New extended model of hadrons.” *Phys. Rev.* **D9**, 3471 (1974); W. A. Bardeen, M. S. Chanowitz, S. D. Drell, M. Weinstein and T.-M. Yan, “Heavy quarks and strong binding: A field theory of hadron structure.” *Phys. Rev.* **D11**, 1094 (1975); T. D. Lee, *Particle Physics and Introduction to Field Theory*, New York, Harwood Academic Publishers, 1981, p. 550.

- [17] V. N. Gribov and L. N. Lipatov, “Deep Inelastic ep Scattering in Perturbation Theory.” *Sov. Journ. Nucl. Phys.* **15**, 438 (1972); V. N. Gribov and L. N. Lipatov, “ e^+e^- -Pair Annihilation and Deep Inelastic ep Scattering in Perturbation Theory.” *Sov. Journ. Nucl. Phys.* **15**, 675 (1972); G. Altarelli and G. Parisi, “Asymptotic Freedom in Parton Language.” *Nucl. Phys.* **B126**, 298 (1977).
- [18] J. D. Bjorken, “Final State Hadrons in Deep Inelastic Processes and Colliding Beams.” in *Proceedings of the 1971 International Symposium on Electron and Photon Interactions*, edited by N. B. Mistry, Ithaca, 1972, p. 282.
- [19] B. H. Wiik, “HERA Status.” in *Proceedings of the Workshop Physics at HERA*, edited by W. Buchmüller and G. Ingelman, Hamburg, 1991. This reviews the status of HERA as of late January 1992.
- [20] B. Rossi, *High-Energy Particles*, Englewood Cliffs, New Jersey, Prentice-Hall, Inc., 1952.
- [21] W. R. Nelson, H. Hirayama and D. W. O. Rogers, “The EGS4 Code System.” SLAC-265, Stanford Linear Accelerator Center (Dec. 1985).
- [22] B. Rossi, *High-Energy Particles*, Englewood Cliffs, New Jersey, Prentice-Hall, Inc., 1952, p. 50. The radiation length, r.l., is defined by the equation

$$(\text{r.l.})^{-1} = 4\alpha \frac{N_A}{A} Z^2 r_e^2 \ln(183Z^{-\frac{1}{3}}),$$

where α is the fine structure constant, N_A is Avogadro’s number, A is the atomic weight, Z is the atomic number, and r_e is the classical electron radius.

- [23] Particle Data Group, L. Montanet *et al.*, “Review of Particle Properties.” *Phys. Rev.* **D50**, p. 1242 (1994). The interaction length in a given medium in units of g cm^{-2} , λ , can be computed from the formula $\lambda = A/(N_A \times \sigma_I)$, where A is the atomic weight, N_A is Avogadro’s number, and σ_I is the nuclear inelastic cross section.

- [24] H. Brückmann, B. Anders and U. Behrens, "Hadron Sampling Calorimetry, A Puzzle of Physics." *Nucl. Instr. and Meth.* **A263**, 136 (1988); H. Brückmann *et al.*, "On the Theoretical Understanding and Calculation of Sampling Calorimeters." in *Proceedings of the 15th Winter Meeting on Fundamental Physics: Lepton-Nucleon Interactions at High Energies*, edited by F. Barreiro and J. L. Sanchez-Gomez, Sevilla, 1987, p. 69.
- [25] B. Lu, L. W. Mo and T. A. Nunamaker, "The Cockcroft-Walton photomultiplier tube base and the Ethernet high voltage controller." *Nucl. Instr. and Meth.* **A313**, 135 (1992).
- [26] A. Caldwell *et al.*, "Design and implementation of a high precision readout system for the ZEUS calorimeter." *Nucl. Instr. and Meth.* **A321**, 356 (1992).
- [27] A. Andresen *et al.*, "Construction and beam test of the ZEUS forward and rear calorimeter." *Nucl. Instr. and Meth.* **A309**, 101 (1991).
- [28] A. Bernstein *et al.*, "Beam Tests of the ZEUS Barrel Calorimeter." *Nucl. Instr. and Meth.* **A336**, 23 (1993).
- [29] I. Ambats *et al.*, "Cosmic ray tests of the ZEUS barrel calorimeter modules." *Nucl. Instr. and Meth.* **A320**, 161 (1992).
- [30] S. Fisher and P. Palazzi, *Adamo Entity-Relationship Programming System: Version 3.3*, Programming Techniques Group, ECP Division, CERN, October 1993.
- [31] B. Rossi, *High-Energy Particles*, Englewood Cliffs, New Jersey, Prentice-Hall, Inc., 1952, p. 257.
- [32] A. Kwiatkowski, H. Spiesberger and H.-J. Möhring, "HERACLES 4.1 – An Event Generator for *ep* Interactions at HERA Including Radiative Processes."

in *Proceedings of the Workshop Physics at HERA*, edited by W. Buchmüller and G. Ingelman, Hamburg, 1991.

- [33] G. Ingelman, “LEPTO version 6.1 – The Lund Monte Carlo for Deep Inelastic Lepton-Nucleon Scattering.” in *Proceedings of the Workshop Physics at HERA*, edited by W. Buchmüller and G. Ingelman, Hamburg, 1991.
- [34] T. Sjöstrand, “The Lund Monte Carlo for Jet Fragmentation and e^+e^- Physics - JETSET version 6.2.” *Comput. Phys. Commun.* **39**, 347 (1986); T. Sjöstrand and M. Bengtsson, “The Lund Monte Carlo for Jet Fragmentation and e^+e^- Physics - JETSET version 6.3 - An Update.” *Comput. Phys. Commun.* **43**, 367 (1987).
- [35] B. Andersson *et al.*, “Parton Fragmentation and String Dynamics.” *Phys. Rep.* **97**, 31 (1983).
- [36] A. D. Martin, R. G. Roberts and W. J. Stirling, “Parton Distributions Updated.” *Phys. Lett.* **B306**, 145 (1993).
- [37] *The ZEUS Detector: Status Report 1993*, DESY 1993, p. 17-18.
- [38] R. Brun *et al.*, GEANT 3.13, CERN DD/EE/84-1 (1987).
- [39] *The ZEUS Detector: Status Report 1993*, DESY 1993, p. 17-21.
- [40] G. Ingelman and P. E. Schlein, “Jet Structure in High Mass Diffractive Scattering.” *Phys. Lett.* **B152**, 256 (1985); G. Ingelman and K. Prytz, “The pomeron structure in DIS and gluon recombination effects.” *Z. Phys.* **C58**, 285 (1993); P. Bruni and G. Ingelman, “Diffractive W and Z production at $p\bar{p}$ colliders and the pomeron parton content.” *Phys. Lett.* **B311**, 317 (1993).
- [41] P. Bruni and G. Ingelman, “POMPYT version 1.0 - A Monte Carlo to Simulate Diffractive Hard Scattering Processes.”, DESY 93-187; P. Bruni and G. Ingel-

man, in *Proceedings of the Europhysics Conference on High Energy Physics*, Marseille, 1993, p. 595.

- [42] H.-U. Bengtsson and T. Sjöstrand, “The Lund Monte Carlo for Hadronic Processes – PYTHIA version 4.8.” *Comput. Phys. Commun.* **46**, 43 (1987).
- [43] N.N. Nikolaev and B.G. Zakharov, “Pomeron structure function and diffraction dissociation of virtual photons in perturbative QCD.” *Z. Phys.* **C53**, 331 (1992).
- [44] A. Solano, Ph.D. dissertation, University of Torino, 1993 (unpublished).
- [45] A. Donnachie and P. V. Landshoff, “Hard Diffraction: Production of High p_T Jets, W or Z , and Drell-Yan Pairs.” *Nucl. Phys.* **B303**, 634 (1988).
- [46] UA4 Collaboration, M. Bozzo *et al.*, “Single Diffraction Dissociation at the CERN SPS Collider.” *Phys. Lett.* **B136**, 217 (1984).
- [47] UA8 Collaboration, R. Bonino *et al.*, “Evidence for Transverse Jets in High-Mass Diffraction.” *Phys. Lett.* **B211**, 239 (1988); A. Brandt *et al.*, “Evidence for a Super-Hard Pomeron Structure.” *Phys. Lett.* **B297**, 417 (1992).
- [48] Y. Akimov *et al.*, “Excitation of High-Energy Protons into Low-Mass States in p - d Interactions.” *Phys. Rev. Lett.* **35**, 763 (1975); Y. Akimov *et al.*, “Diffraction Dissociation of High-Energy Protons in p - d Interactions.” *Phys. Rev. Lett.* **35**, 766 (1975).
- [49] J. D. Bjorken, “Hard Diffraction in Deep Inelastic Scattering.” invited talk given at the 1994 International Conference on Deep Inelastic Scattering, Eilat, Israel, February 6-12, 1994.
- [50] H. L. Anderson *et al.*, “Measurement of Nucleon Structure Function in Muon Scattering at 147 GeV/c.” *Phys. Rev. Lett.* **37**, 4 (1976); H. L. Anderson *et al.*, “Measurement of the Proton Structure Function from Muon Scattering.” *Phys.*

Rev. Lett. **38**, 1450 (1977); L. W. Mo, "High Energy Muon Scattering at FER-MILAB." in *Proceedings of the 1975 International Symposium on Lepton and Photon Interactions at High Energies*, edited by W. T. Kirk, Stanford, 1975, p. 651; R. E. Taylor, "Inelastic Electron-Nucleon Scattering Experiments." in *Proceedings of the 1975 International Symposium on Lepton and Photon Interactions at High Energies*, edited by W. T. Kirk, Stanford, 1975, p. 679; BCDMS Collaboration, A. C. Benvenuti *et al.*, "A High Statistics Measurement of the Nucleon Structure Function $F_2(x, Q^2)$ from Deep Inelastic Muon-Carbon Scattering at High Q^2 ." *Phys. Lett.* **B195**, 91 (1987); BCDMS Collaboration, A. C. Benvenuti *et al.*, "A High Statistics Measurement of the Proton Structure Functions $F_2(x, Q^2)$ and R from Deep Inelastic Muon Scattering at High Q^2 ." *Phys. Lett.* **B223**, 485 (1989); BCDMS Collaboration, A. C. Benvenuti *et al.*, "A High Statistics Measurement of the Deuteron Structure Functions $F_2(x, Q^2)$ and R from Deep Inelastic Muon Scattering at High Q^2 ." *Phys. Lett.* **B237**, 592 (1990); NMC Collaboration, P. Amaudruz *et al.*, "Proton and deuteron F_2 structure functions in deep inelastic muon scattering." *Phys. Lett.* **B295**, 159 (1992); L. W. Whitlow *et al.*, "Precise measurements of the proton and deuteron structure functions from a global analysis of the SLAC deep inelastic electron scattering cross sections." *Phys. Lett.* **B282**, 475 (1992); ZEUS Collaboration, M. Derrick *et al.*, "Measurement of the Proton Structure Function F_2 from the 1993 HERA Data." DESY-94-143, August 1994.

- [51] C. G. Callan and D. J. Gross, "High-energy Electroproduction and the Constitution of the Electric Current." *Phys. Rev. Lett.* **22**, 156 (1969).
- [52] Particle Data Group, L. Montanet *et al.*, "Review of Particle Properties." *Phys. Rev.* **D50**, p. 1233 (1994).

- [53] Particle Data Group, L. Montanet *et al.*, “Review of Particle Properties.” *Phys. Rev. D* **50**, p. 1309 (1994). The value quoted is a combination of the measurements by the four CERN electron-positron experiments ALEPH, DELPHI, L3, and OPAL.
- [54] L. Hand, Ph.D. dissertation, Stanford University, 1961 (unpublished); L. Hand, “Experimental Investigation of Pion Electroproduction.” *Phys. Rev.* **129**, 1834 (1963).
- [55] M. N. Rosenbluth, “High Energy Elastic Scattering of Electrons on Protons.” *Phys. Rev.* **79**, 615 (1950).

Tables

Table 1: Parameters of HERA Beams

Beam Attribute	Electron	Proton
Nominal energy	30 GeV	820 GeV
Injection energy	14 GeV	40 GeV
Nominal particle current	60 mA	160 mA
Number of bunches	220	220
Nominal bunch length	8.0 mm	110 mm
Beam width at interaction point	0.26 mm	0.29 mm
Beam height at interaction point	0.02 mm	0.07 mm
Radiation energy loss per turn	127 MeV	6.24×10^{-6} MeV
Nominal filling time	15 min	20 min

Table 2: Parameters of HERA Rings

Ring Attribute	Electron	Proton
Total number of magnets	2009	1819
Main dipoles maximum field strength	0.165 T	4.68 T
Main dipoles bending radius	606 m	584 m
Number of conventional RF cavities	82	2 (4)
Number of superconducting RF cavities	16	–
Frequency of RF cavities	499.776 MHz	52.033 (208.13) MHz

Table 3: Subtriggers Involving Calorimeter Alone

Name	Description: Conditions to Satisfy the Subtrigger
EMC_E(10068)	Total energy in EMC section, excluding region around FCAL and RCAL beam pipe holes, greater than 10.068 GeV
BEMC_E(3404)	Total energy in BEMC section greater than 3.404 GeV
Et(11574)	Total transverse energy, excluding region around FCAL beam pipe hole, greater than 11.574 GeV
FBCAL_Emiss(12162)	Missing energy, calculated using only FCAL and BCAL, greater than 12.162 GeV
CAL_E(14968)	Total energy in entire calorimeter, excluding region around FCAL and RCAL beam pipe holes, greater than 14.968 GeV
REMC_E(2032)	Total energy in REMC section, excluding region around beam pipe hole, greater than 2.032 GeV
FBCAL_Emiss*Et	(Missing energy, excluding RCAL, greater than 10.104 GeV) .AND. (Total transverse energy greater than 3.93 GeV)
REMCth(3750)	REMC threshold sum of energy in region around beam pipe hole greater than 3.75 GeV

Table 4: Subtriggers Involving Calorimeter and Other Components

Name	Description: Conditions Satisfying Subtrigger
FMU _s *CAL _{mx} *CV _v	(FMUON triggered at small angle) .AND. ((FCAL threshold sum of energy greater than 1.25 GeV) .OR. (Total energy in entire calorimeter greater than 0.464 GeV)) .AND. (No signal from either C5 or veto wall)
FMU _l *CAL _{mx} *gTRK*CV _v	(FMUON triggered at large angle) .AND. ((FCAL threshold sum of energy greater than 1.25 GeV) .OR. (Total energy in entire calorimeter greater than 0.464 GeV)) .AND. ("Good" quality tracking in CTD) .AND. (No signal from either C5 or veto wall)
CAL _E *BMU*aTRK	(Total calorimeter energy greater than 0.464 GeV) .AND. (BMUON triggered) .AND. ("Any" quality tracking in CTD)
RCAL _E *RMU*aTRK*CV _v	(Total RCAL energy greater than 0.464 GeV) .AND. (RMUON triggered) .AND. ("Any" quality tracking in CTD) .AND. (No signal from C5 or veto wall)
LE _e *REMC _E	(Energy in LUMI electron calorimeter greater than 5 GeV) .AND. (RCAL energy greater than 0.464 GeV)
REMC _E *aTRK*FbpCV _{iv}	(Total REMC energy greater than 0.464 GeV) .AND. ("Any" quality tracking in CTD) .AND. (FCAL threshold sum of energy in region around beam pipe hole less than 3.75 GeV) .AND. (No signal from either C5 or veto wall)

Figures

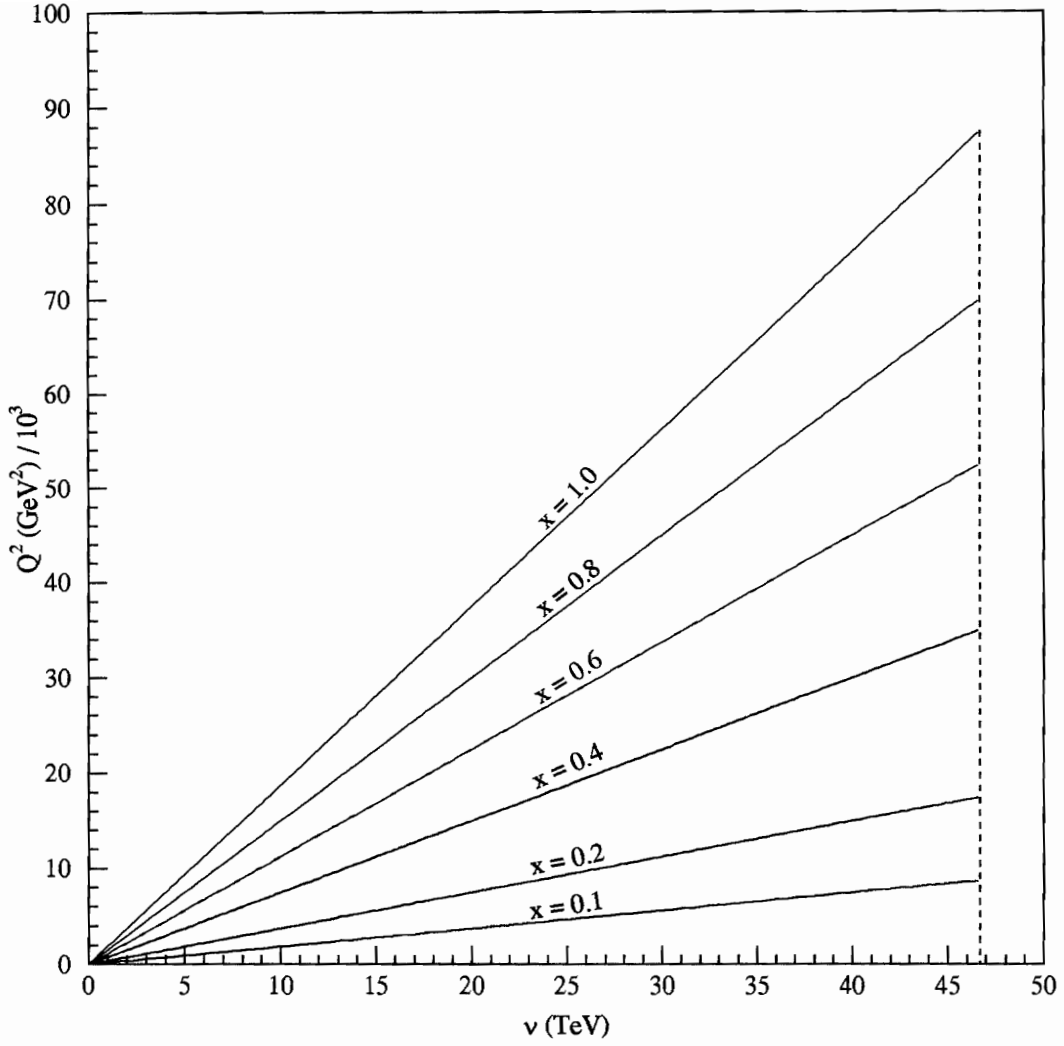


Figure 1: Kinematic region in $Q^2 - \nu$ space available to the ZEUS experiment. Lines of constant x are shown. By way of comparison, the kinematic region available to previous fixed-target experiments extended from $\nu = 0$ to $\nu = 0.5$ TeV and $Q^2 = 0$ to $Q^2 = 400 \text{ GeV}^2$.

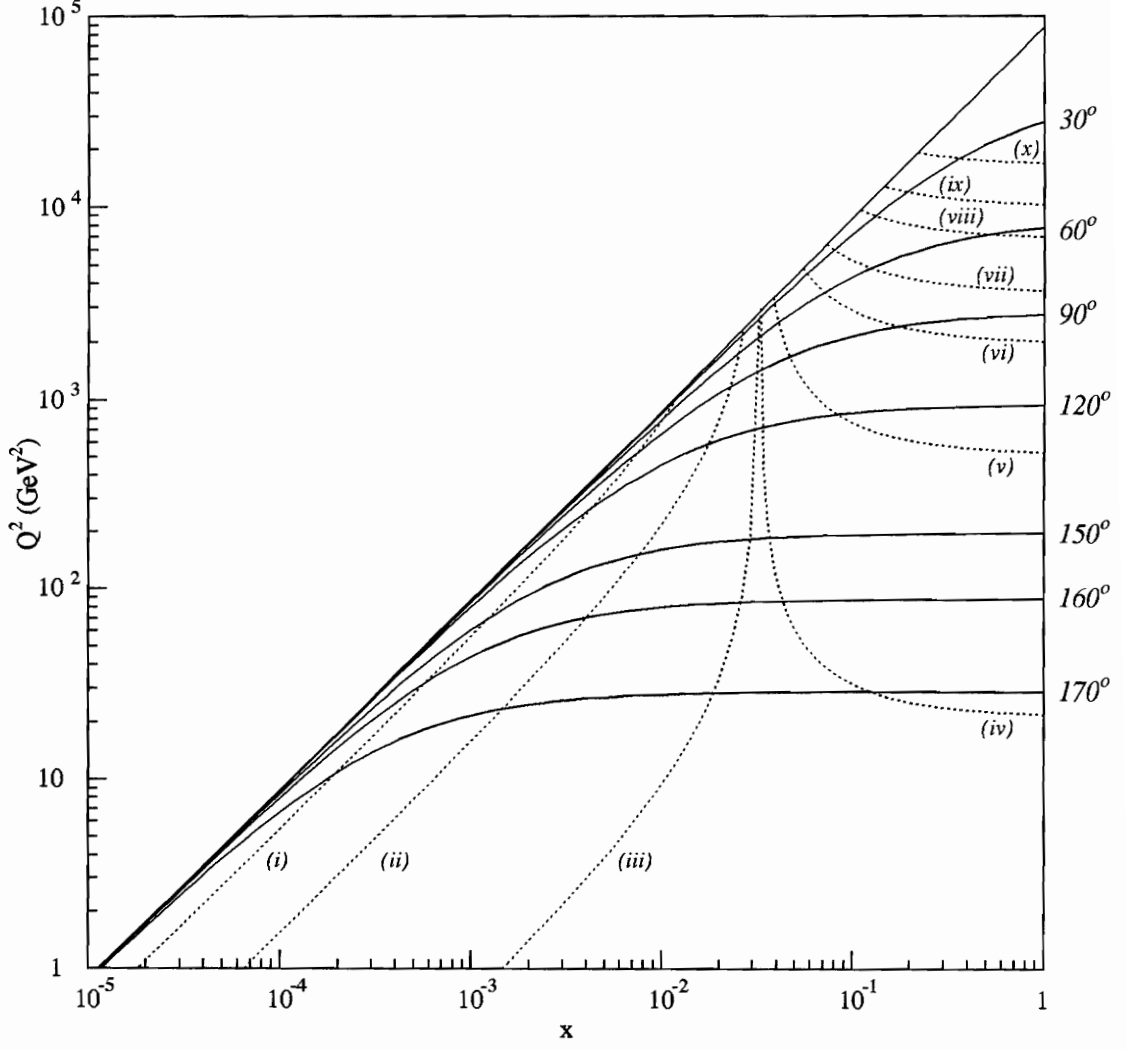


Figure 2: Kinematic region in $Q^2 - x$ space available to the ZEUS experiment. Solid lines are contours of constant scattered electron angle, θ_e , and are labeled at the right. Dotted lines are contours of constant scattered electron energy, E'_e . They correspond to the following energies: (i) $E'_e = 10$ GeV, (ii) $E'_e = 22$ GeV, (iii) $E'_e = 26.5$ GeV, (iv) $E'_e = 26.9$ GeV, (v) $E'_e = 31.5$ GeV, (vi) $E'_e = 45$ GeV, (vii) $E'_e = 60$ GeV, (viii) $E'_e = 90$ GeV, (ix) $E'_e = 120$ GeV, (x) $E'_e = 180$ GeV.

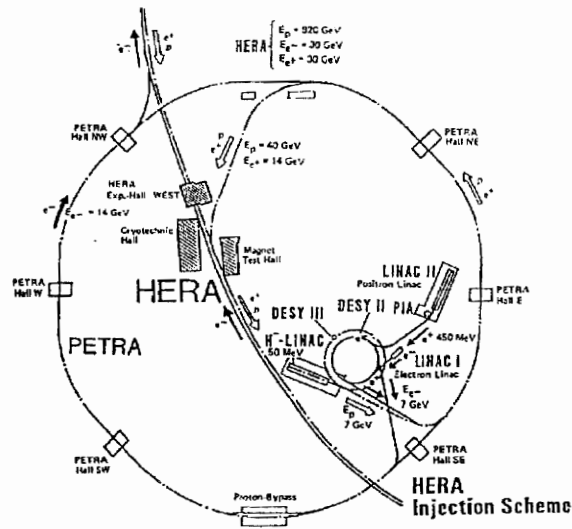
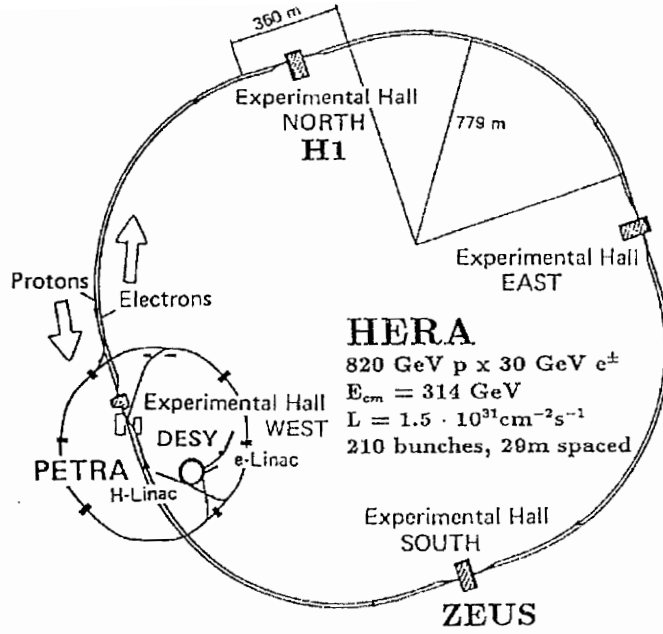


Figure 3: An aerial view of the HERA electron-proton collider and injection scheme.

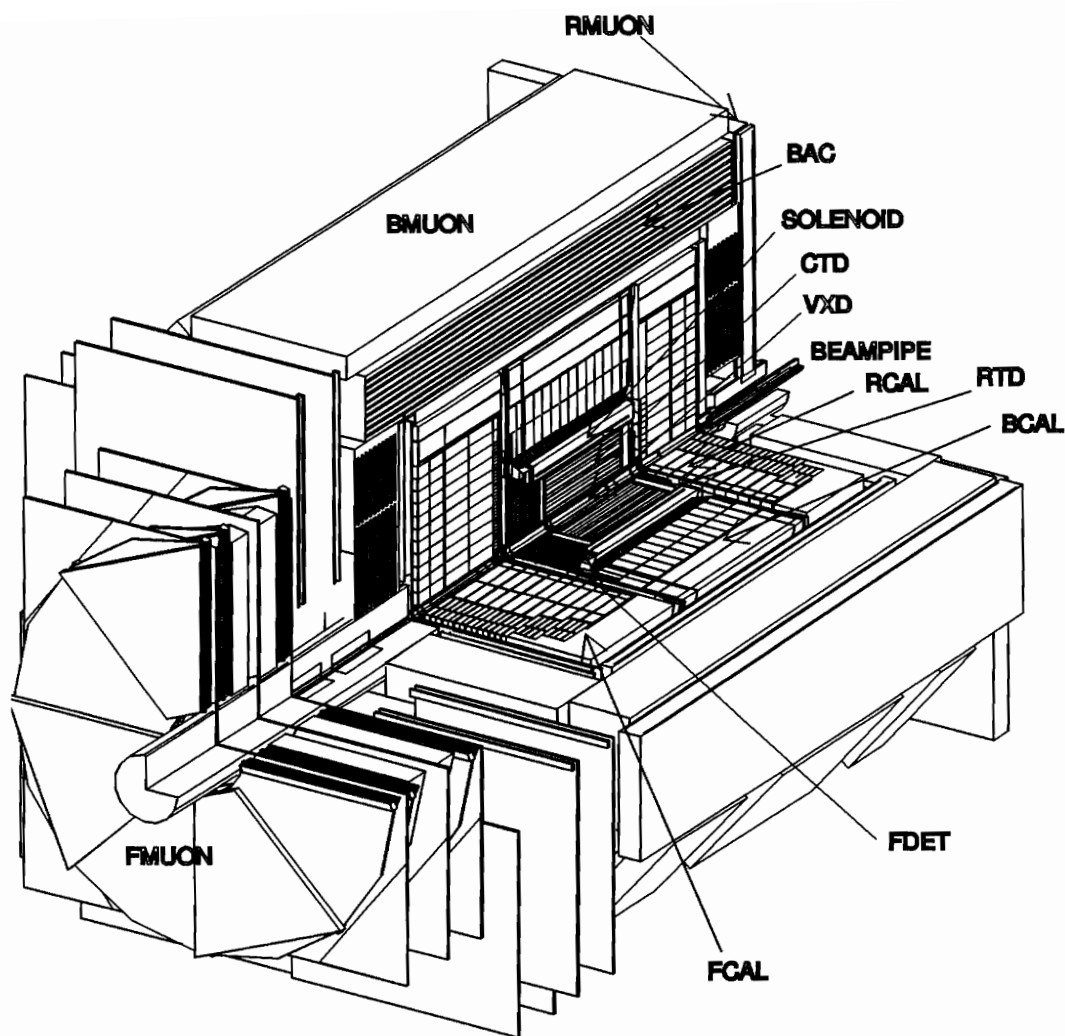


Figure 4: Three-dimensional view of the ZEUS detector. Shown are the central tracking components (VXD, CTD, FDET, RTD), the calorimeter (FCAL, BCAL, RCAL, BAC), the muon detection system (FMUON, BMUON, RMUON), and the solenoid. Protons enter along the $+z$ direction heading towards the FCAL, and electrons enter along the $-z$ direction heading towards the RCAL.

Overview of the ZEUS Detector
(longitudinal cut)

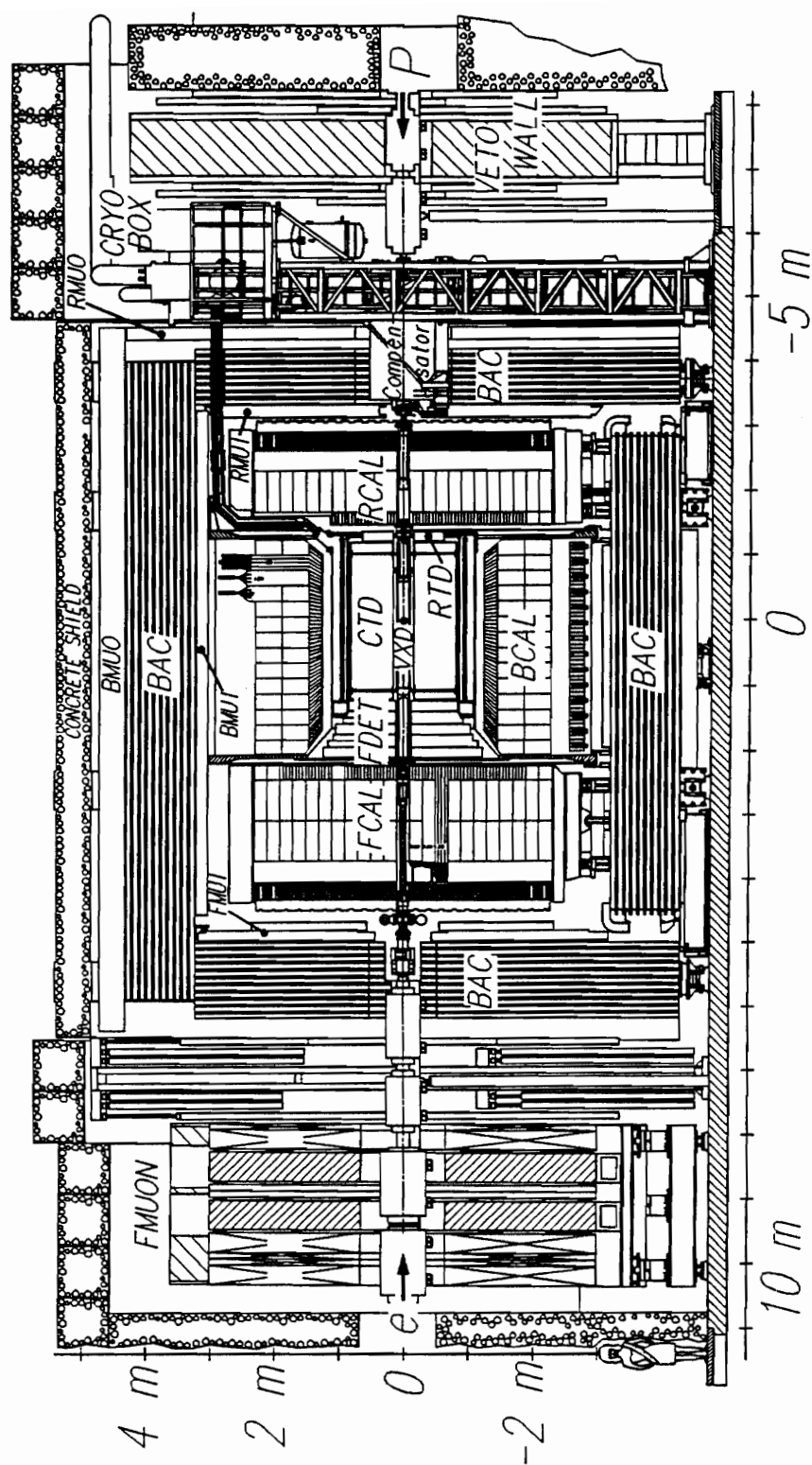


Figure 5: A r - z projection of the ZEUS detector.

Overview of the ZEUS Detector
(cross section)

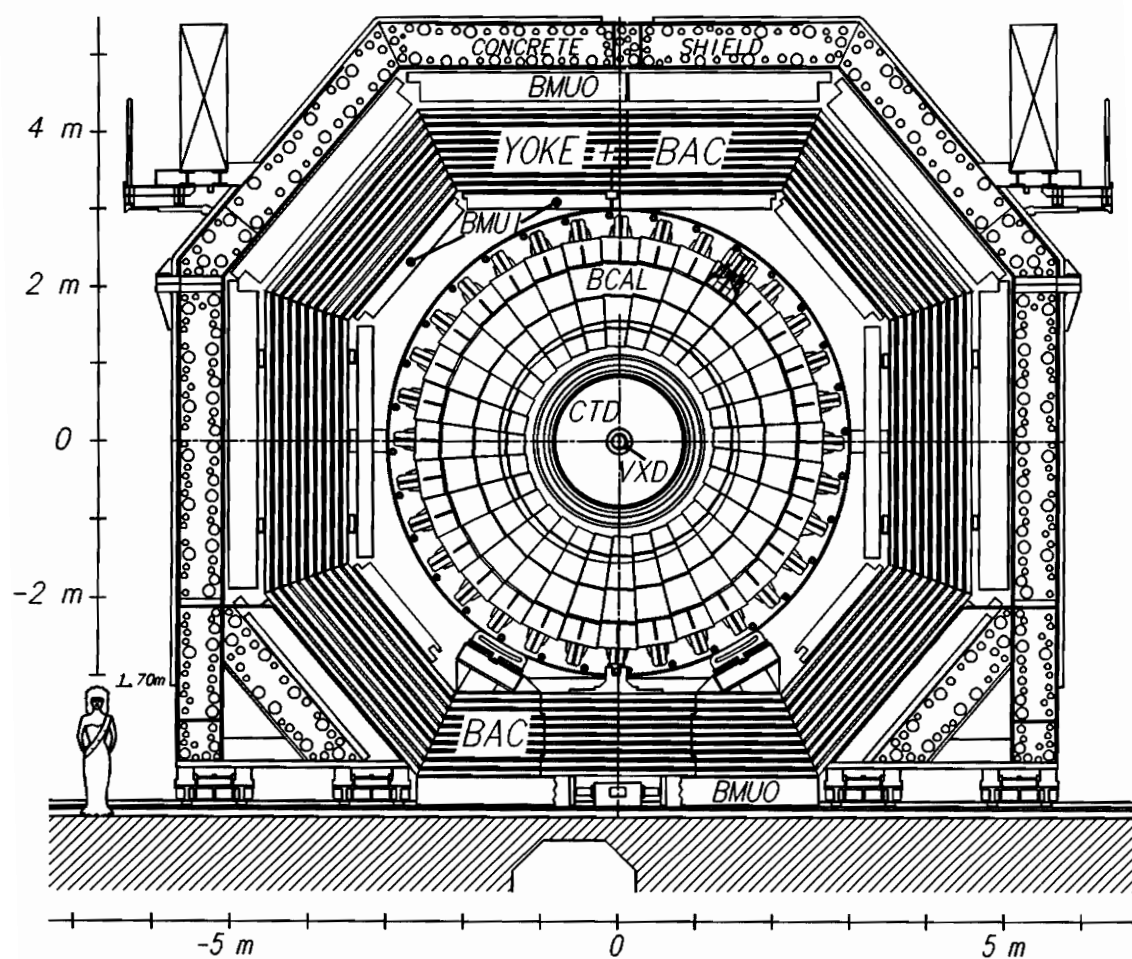


Figure 6: A x - y projection of the ZEUS detector

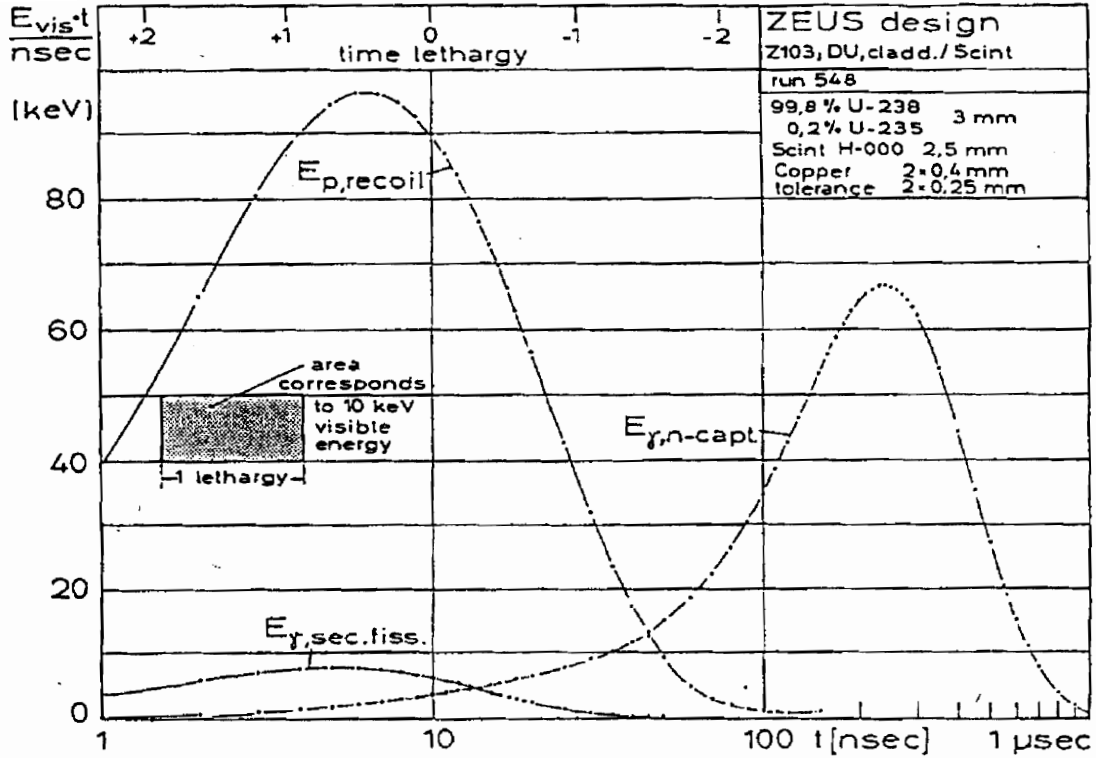


Figure 7: Seen in this figure is the contribution to the calorimeter response from proton recoil in the scintillator and neutron capture. The plot is of the visible energy per nsec multiplied by the time at which the energy appears in the detector layer against the logarithm of the time at which the energy appears in the detector layer. This means the area under the curve gives the integrated contribution to the visible energy from the given process. There is also a small contribution to the visible energy from secondary fissions. The calculations for this plot, which are reported in [24] from where this plot is taken, were carried out using Monte Carlo methods for a DU-scintillator design.

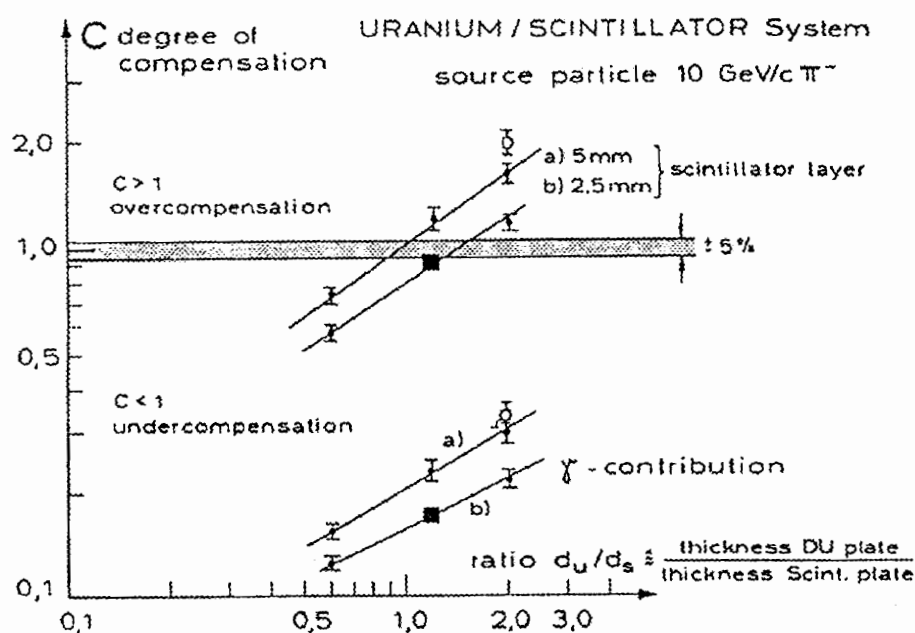


Figure 8: Here is plotted the degree of compensation, C , versus the ratio of DU layer thickness to scintillator layer thickness. There are two curves for scintillator layer thicknesses of 2.5 mm and 5 mm. The regions of overcompensation and undercompensation are indicated, as is the area about $C=1$, where compensation is achieved. This plot is taken from [24].

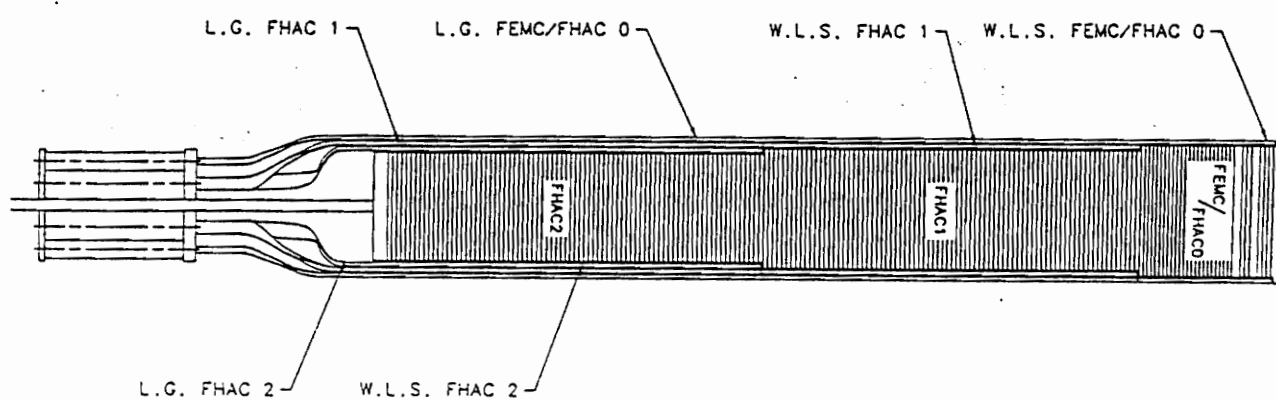


Figure 9: A cross sectional view through a tower of the FCAL. Shown are the FEMC, FHAC1 and FHAC2 sections. Wavelength shifter (WLS) bars run perpendicular to the scintillator tiles on both sides of the tower. They are connected to light guides (LG) which direct the light into photomultiplier tubes at the back end of the tower. The extra large gaps in the FEMC section are for placement of a hadron-electron separation system.

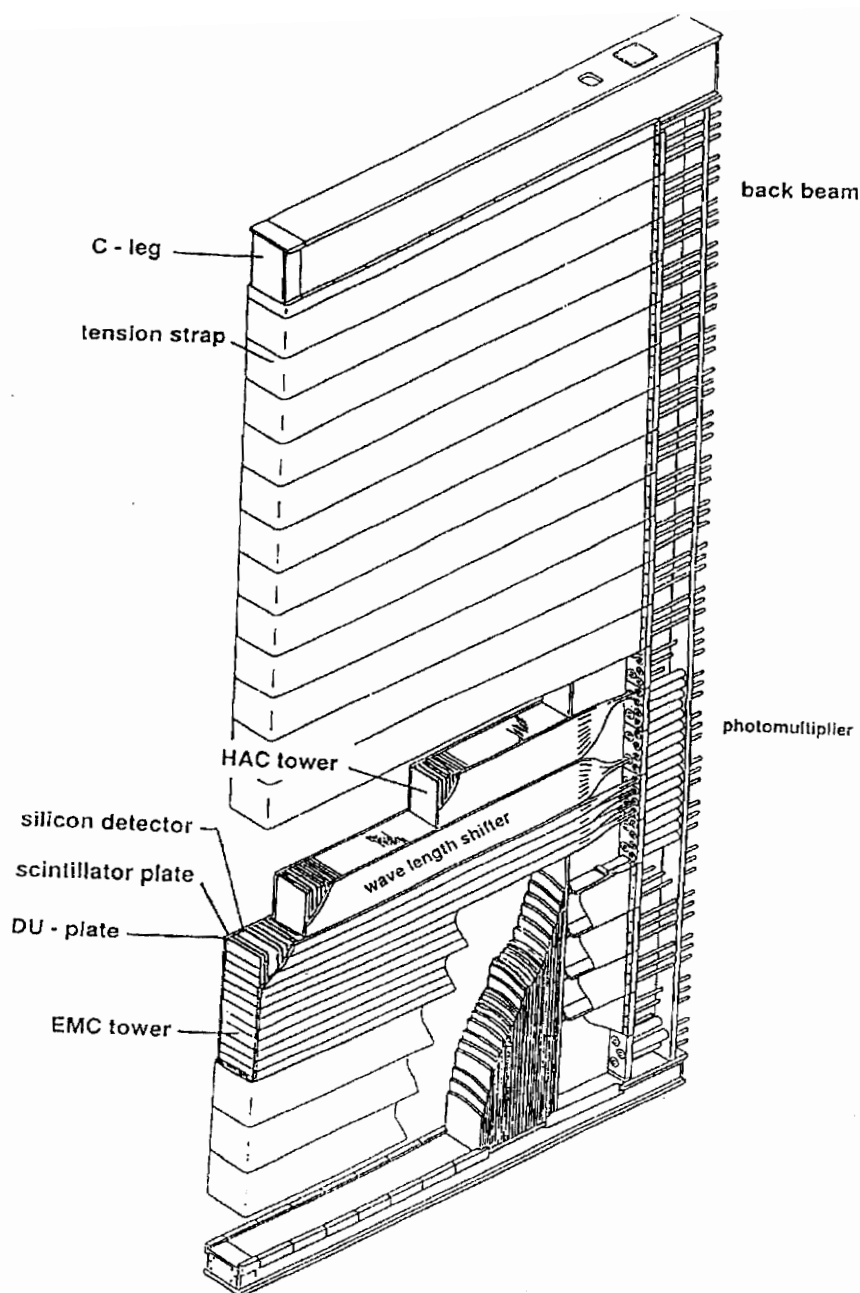


Figure 10: A single FCAL module is shown here, showing the stacked tower design. The fundamental elements of note are as follows: (a) the construction of alternating layers of DU and scintillator plates, (b) the wavelength shifter bars placed perpendicular to the scintillator plates and extending back to the photomultiplier tubes and (c) the gap for a hadron-electron separation system (here denoted “silicon detector”).

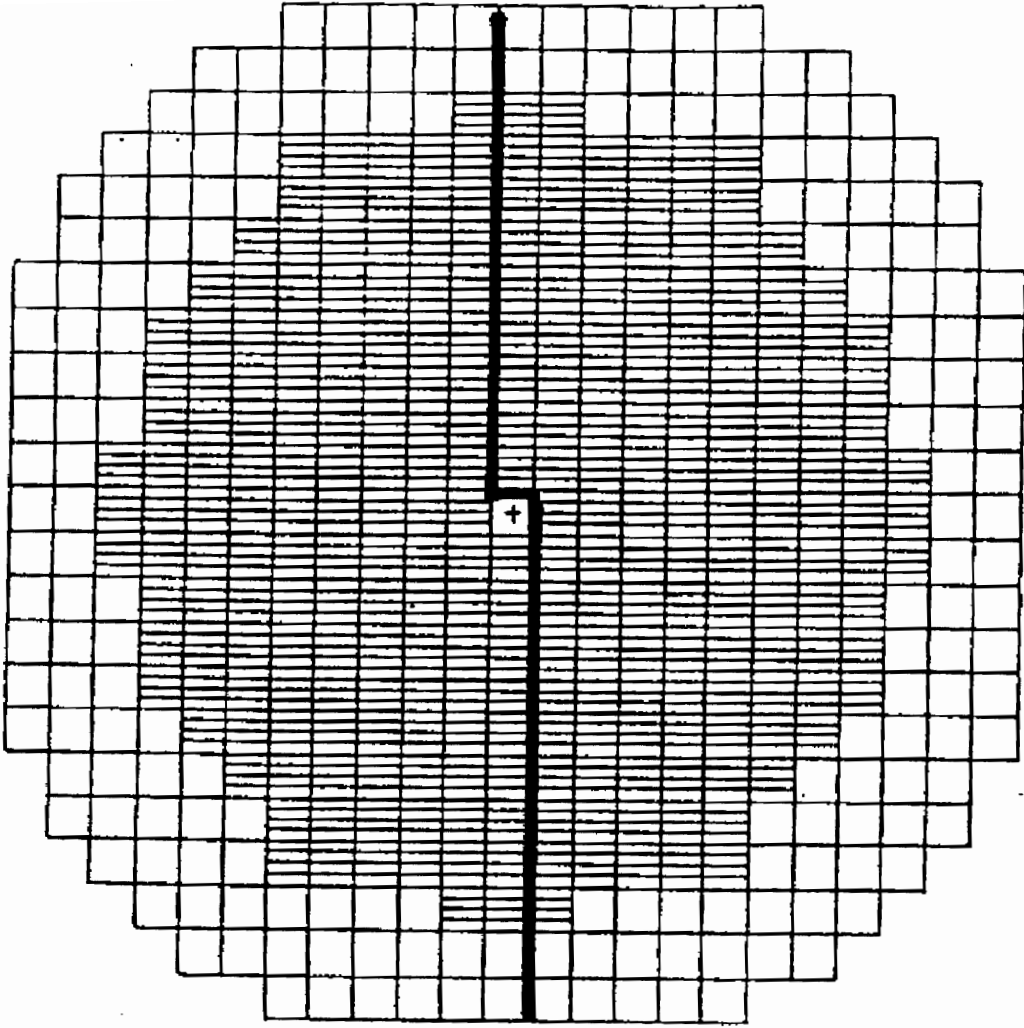


Figure 11: The FCAL as seen from the interaction point. The large squares are $20\text{ cm} \times 20\text{ cm}$. The small rectangles represent the FEMC cells and are $20\text{ cm} \times 5\text{ cm}$. The z -axis points into the page, and the hole in the center is for passage of the beams. The dark line shows where the FCAL is mechanically divided to allow for opening and closing.

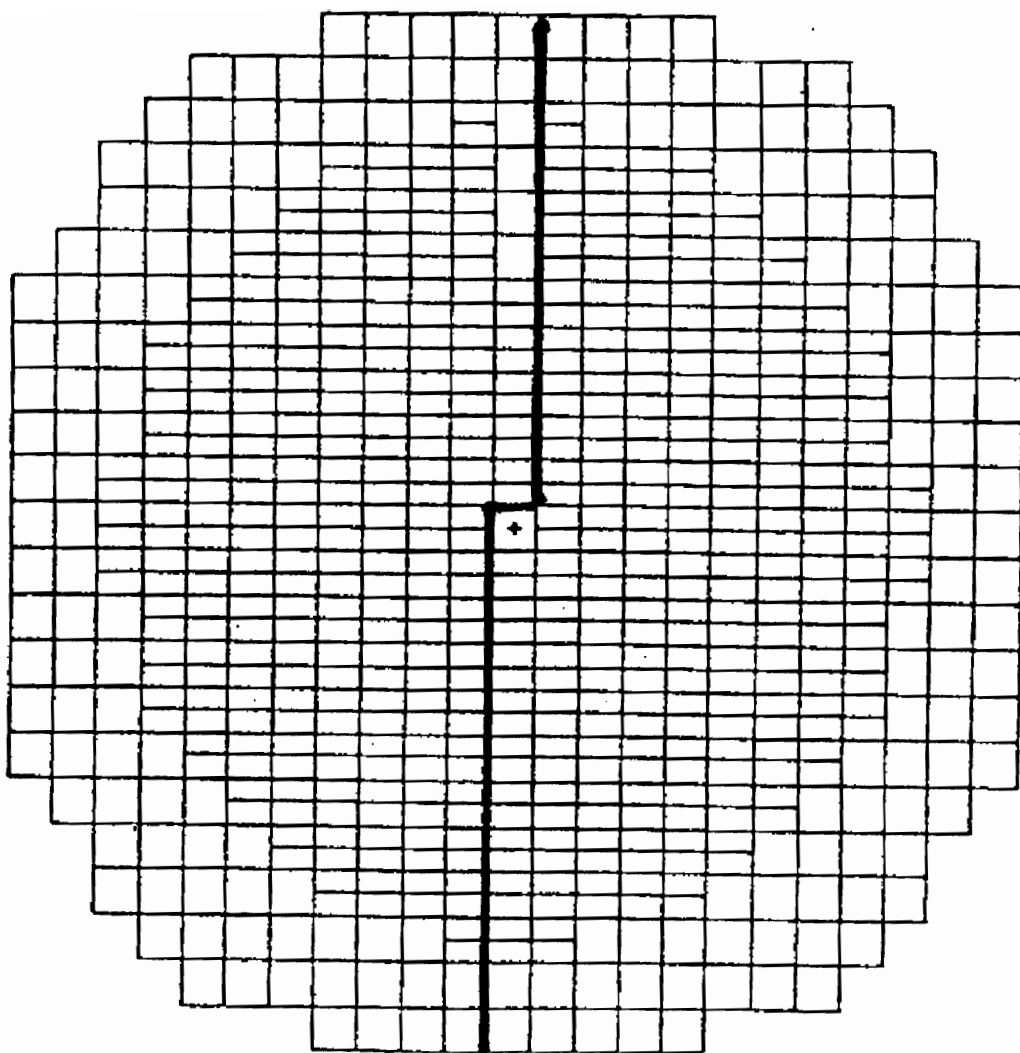


Figure 12: The RCAL as seen from the interaction point. The large squares are $20\text{ cm} \times 20\text{ cm}$. The small rectangles represent the REMC cells and are $20\text{ cm} \times 10\text{ cm}$. The $-z$ -axis points into the page, and the hole in the center is for passage of the beams. The dark line shows where the RCAL is mechanically divided to allow for opening and closing.

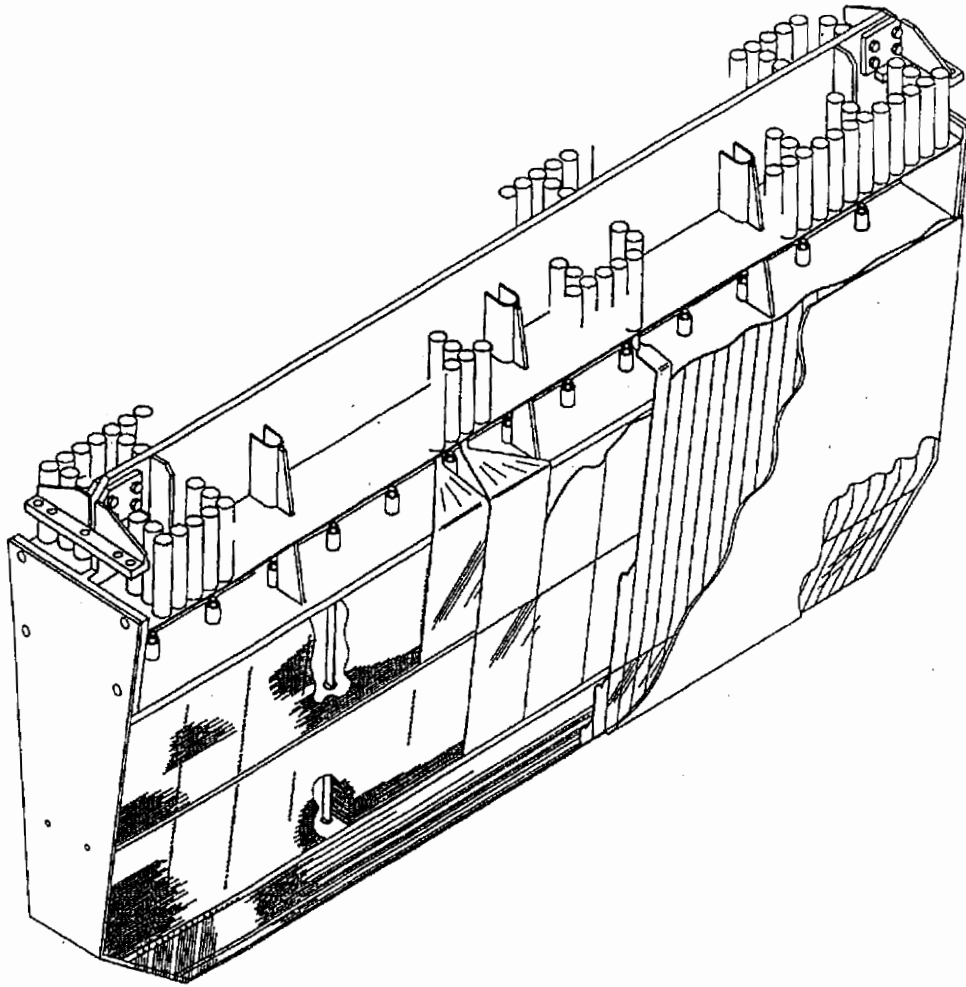


Figure 13: A cut-away view of a single BCAL module.

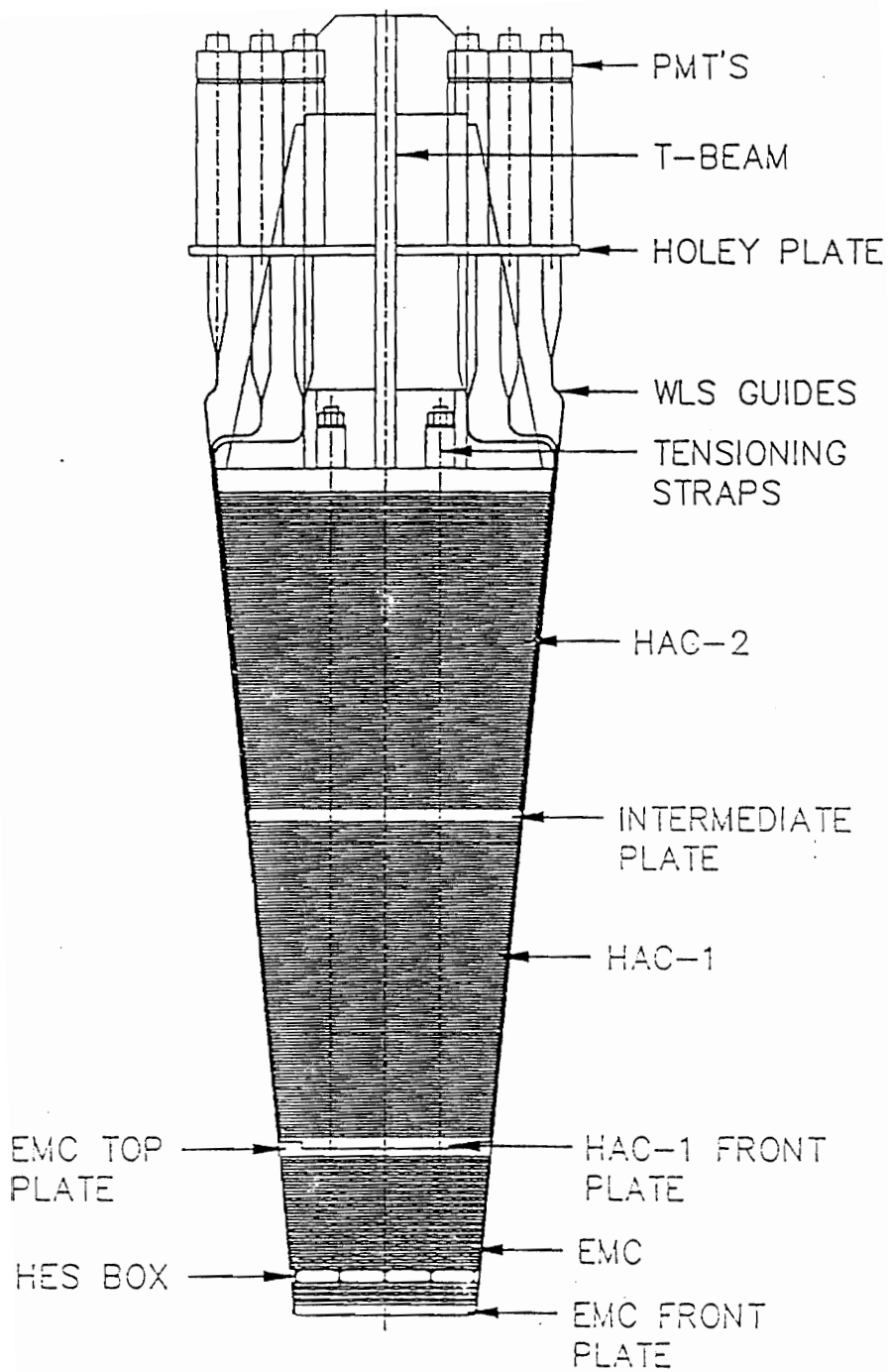


Figure 14: Cross sectional view through a BCAL tower.

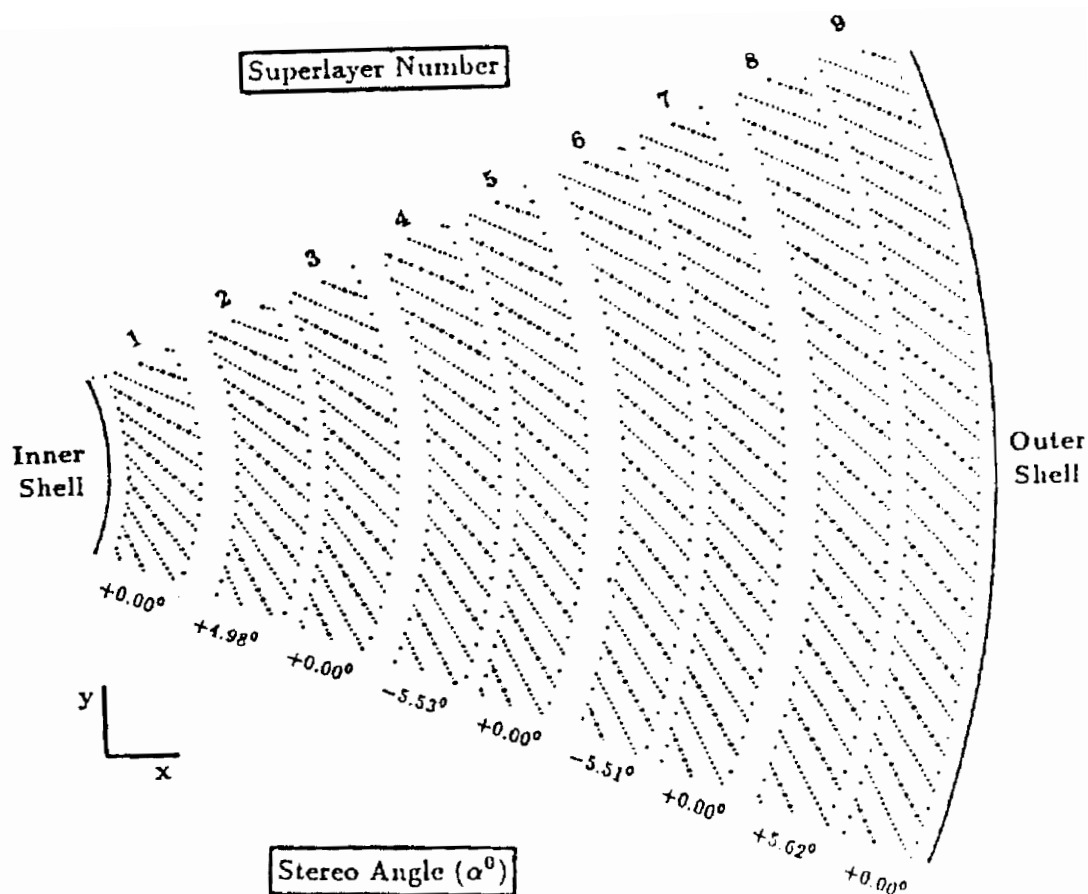


Figure 15: One octant of the CTD is shown here. The CTD consists of nine superlayers, each one being eight sense wires deep along the radius. The sense wires are the thick dots, and the field wires are the thin dots. The plane of the sense wires is tilted by a 45° angle to account for the direction of the electron drift.

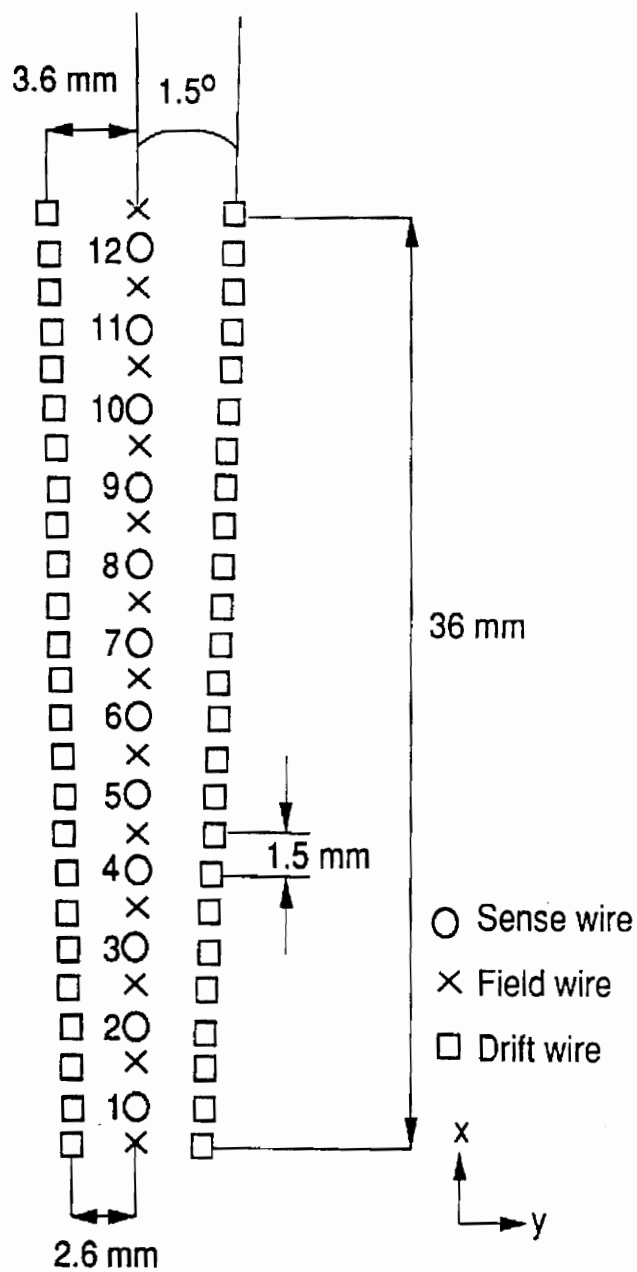


Figure 16: A single cell of the VXD. The radial direction is upward along the x -axis.

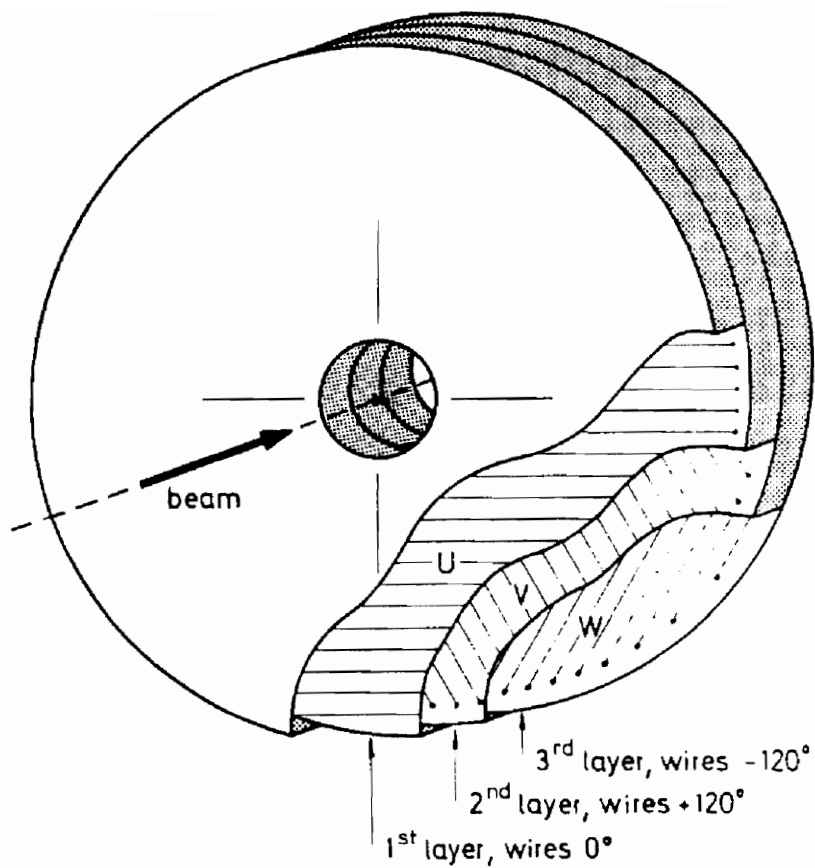


Figure 17: The wire chambers of the forward (FTD) and rear (RTD) tracking systems.

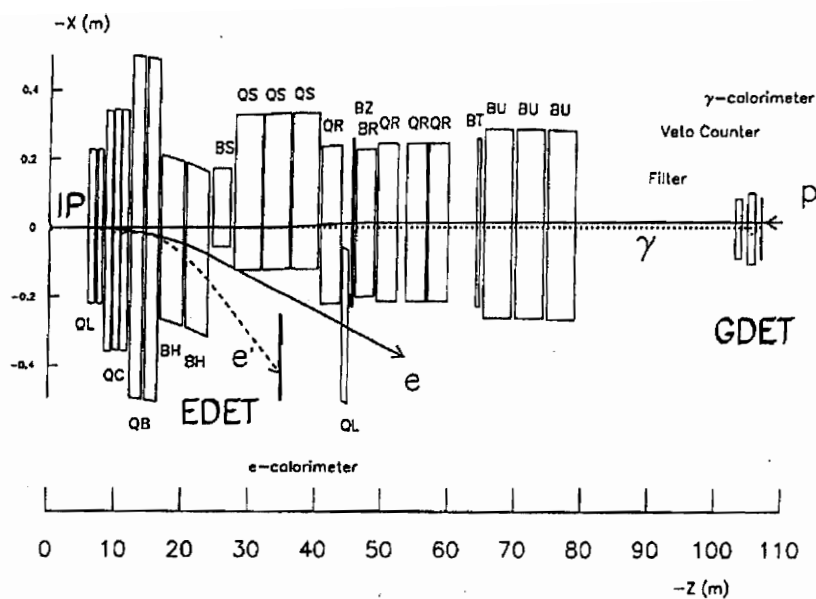


Figure 18: The layout of the ZEUS luminosity monitoring system. The x and z axes are shown, and the nominal interaction point is labelled “IP”. The magnets of HERA are shown: dipole magnets have labels beginning with a B, while quadrupole magnets have labels beginning with a Q. The photon detector is labelled “GDET” and the electron detector is labelled “EDET”. An example of a scattered photon, γ , and a scattered electron, e' , shown. The arrow labelled “e” gives the direction of the electron colliding beam.

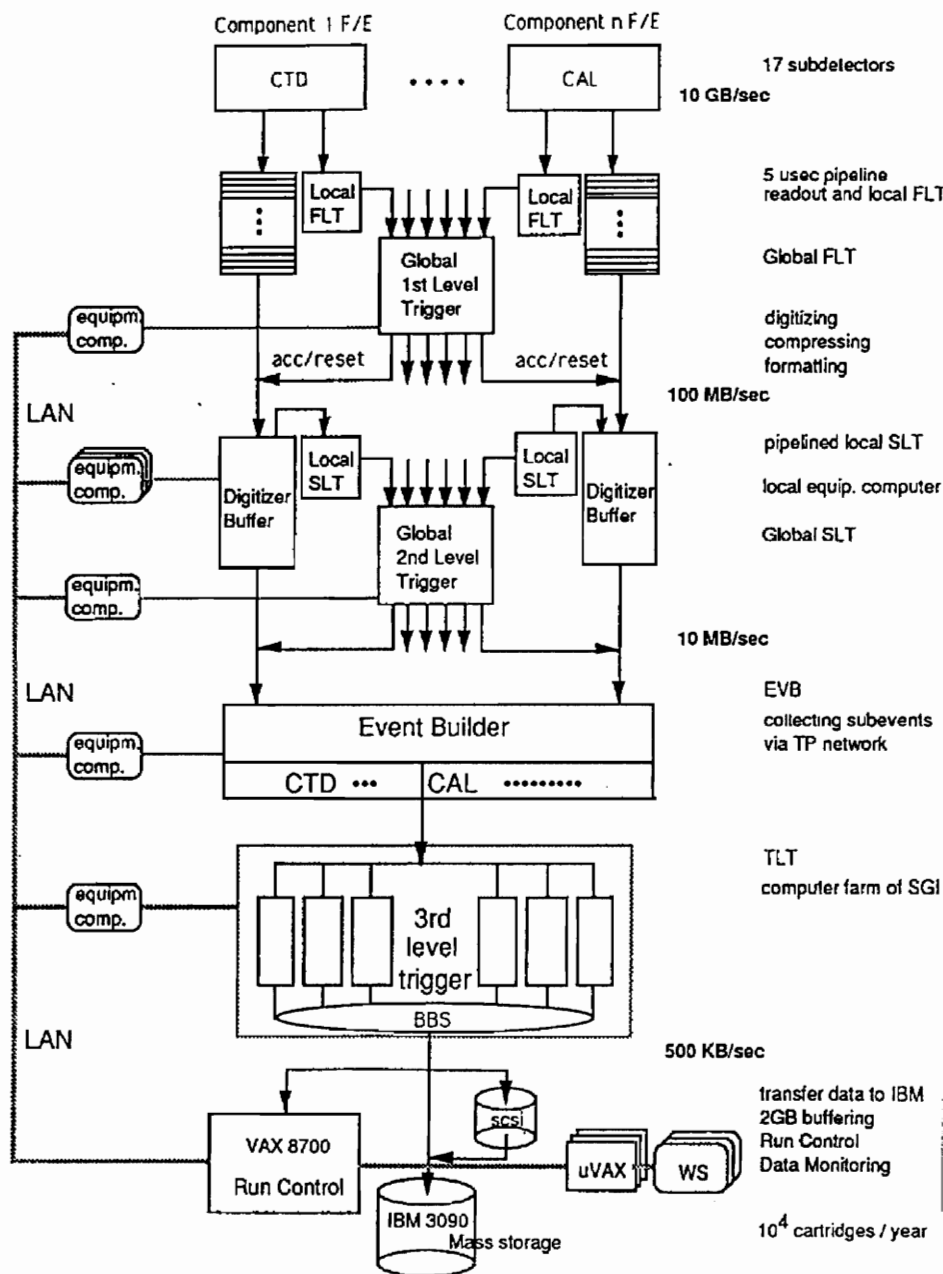


Figure 19: Schematic of the data acquisition system of the ZEUS experiment. The main elements of note are as follows: (a) each subcomponent and its own local FLT, (b) the analog pipelines of the FLT, (c) the global first level trigger (GFLT) and its accept or clear decision (acc/reset), (d) the digital pipelines of the subcomponent second level triggers (SLT), (e) the global second level trigger (GSLT), (f) the event builder (EVB), (g) the third level trigger (TLT), and finally (h) the offline storage.

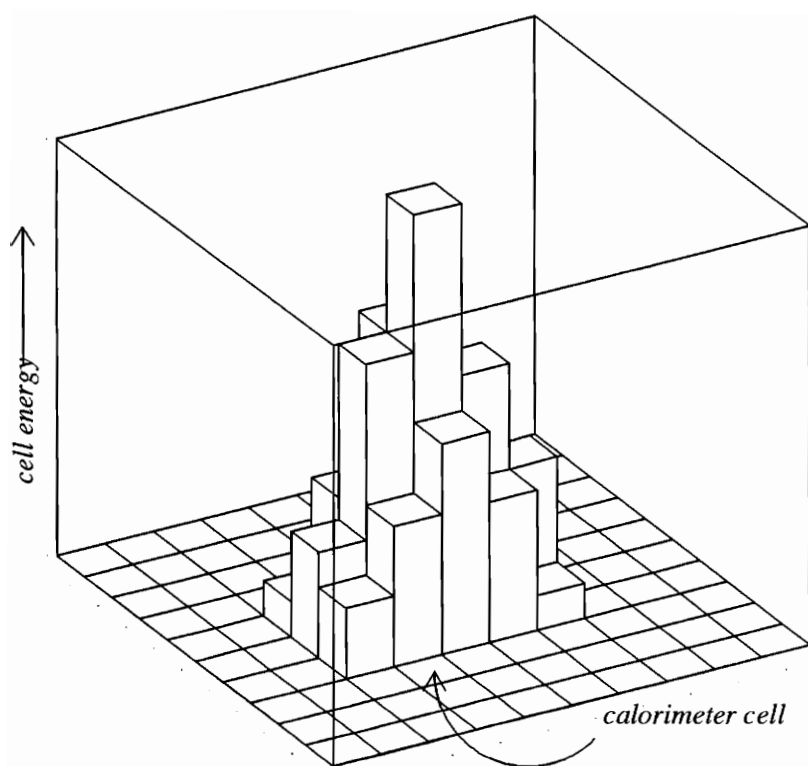


Figure 20: “Lego” plot of a single calorimeter cluster.

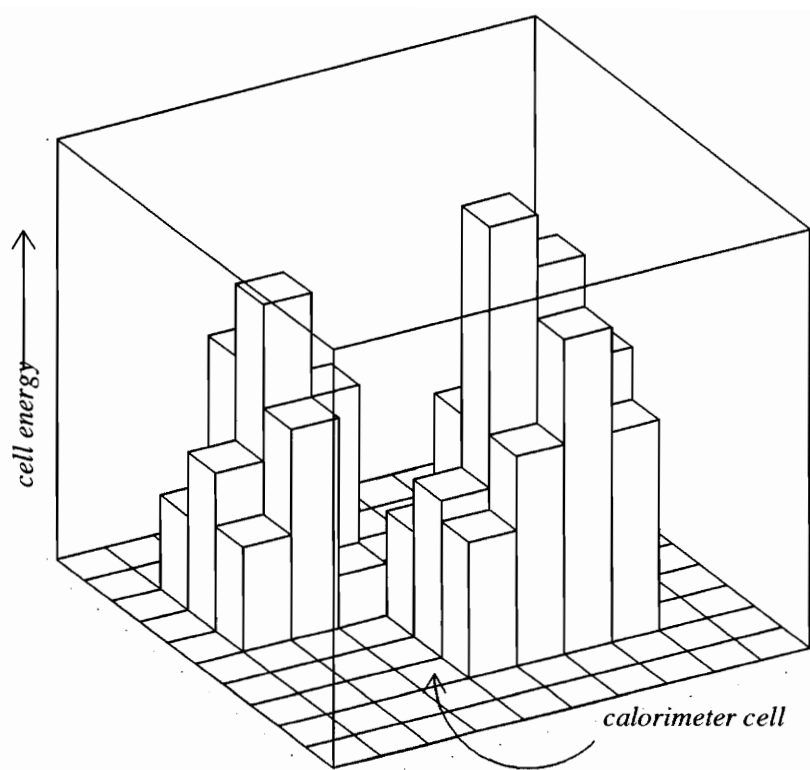


Figure 21: Lego plot of two calorimeter clusters. The two clusters divide along the two cells which are touching on a corner.

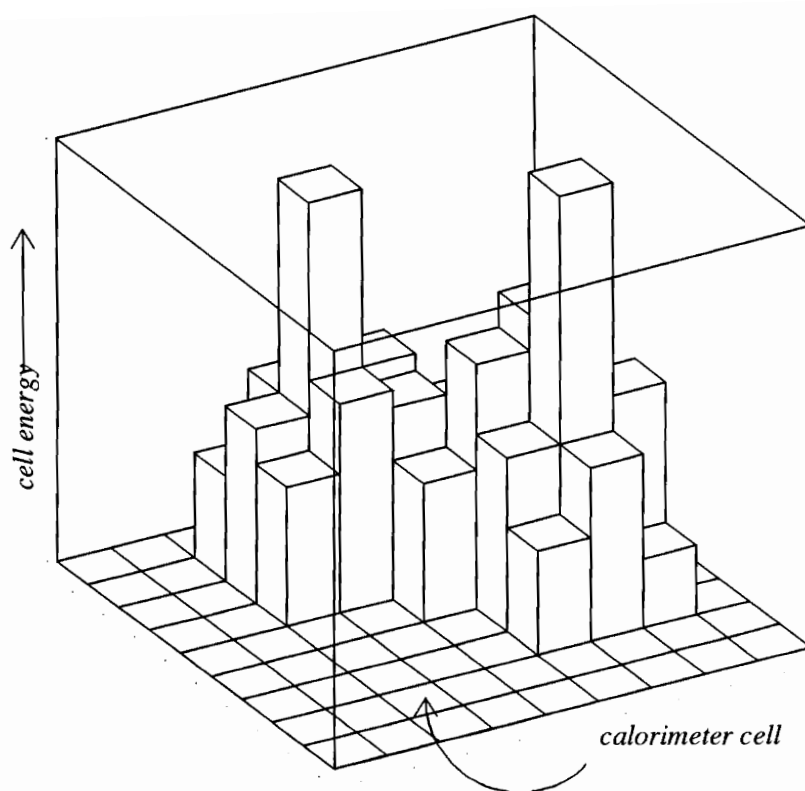


Figure 22: Lego plot of two calorimeter clusters. There are two local maximum energy deposition cells which form the seeds for two separate clusters. The two clusters are divided along the intervening cells of local minimum energy deposition.

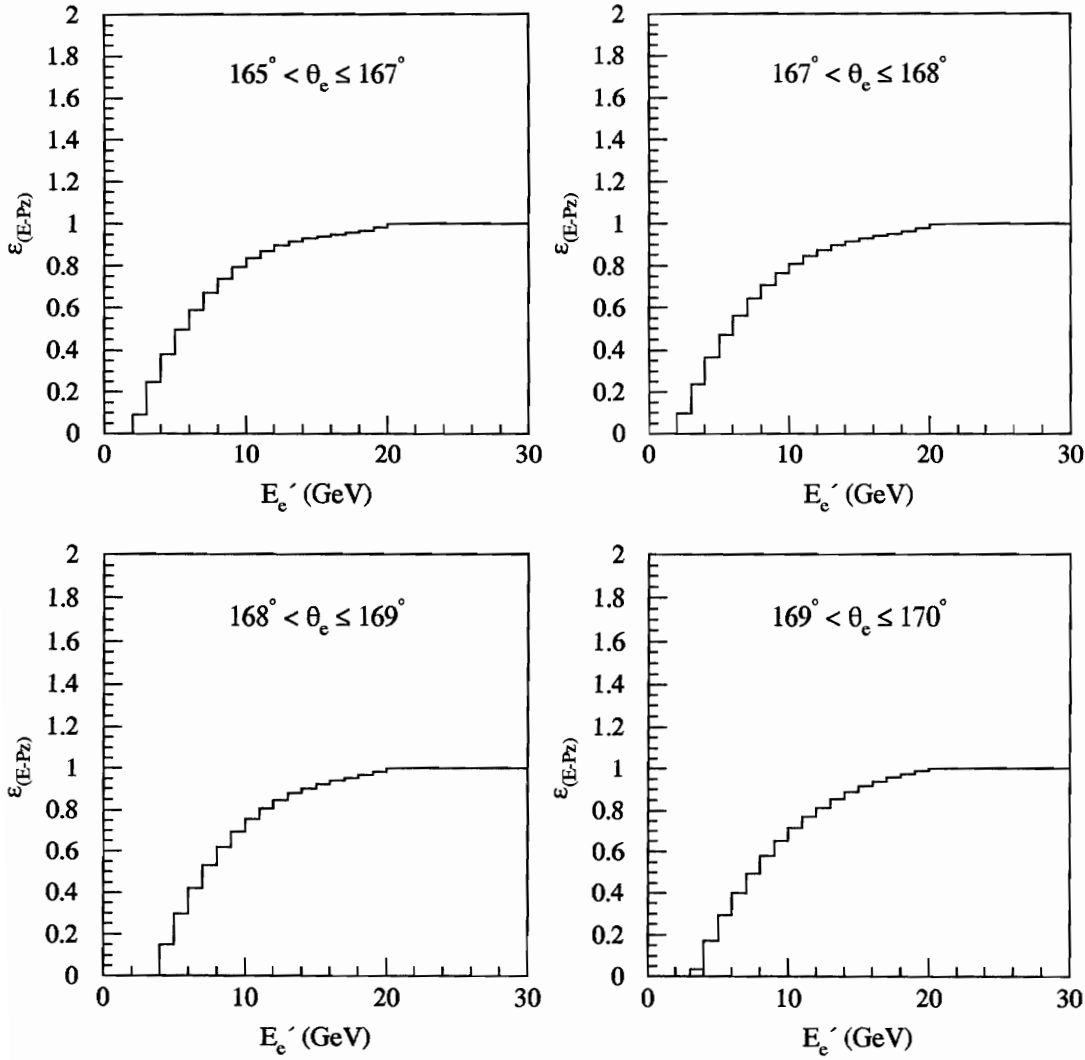


Figure 23: $(E - P_z)$ acceptance as a function of E'_e in four bins of θ_e . The $(E - P_z)$ acceptance was calculated with Monte Carlo data which had been processed through MOZART.

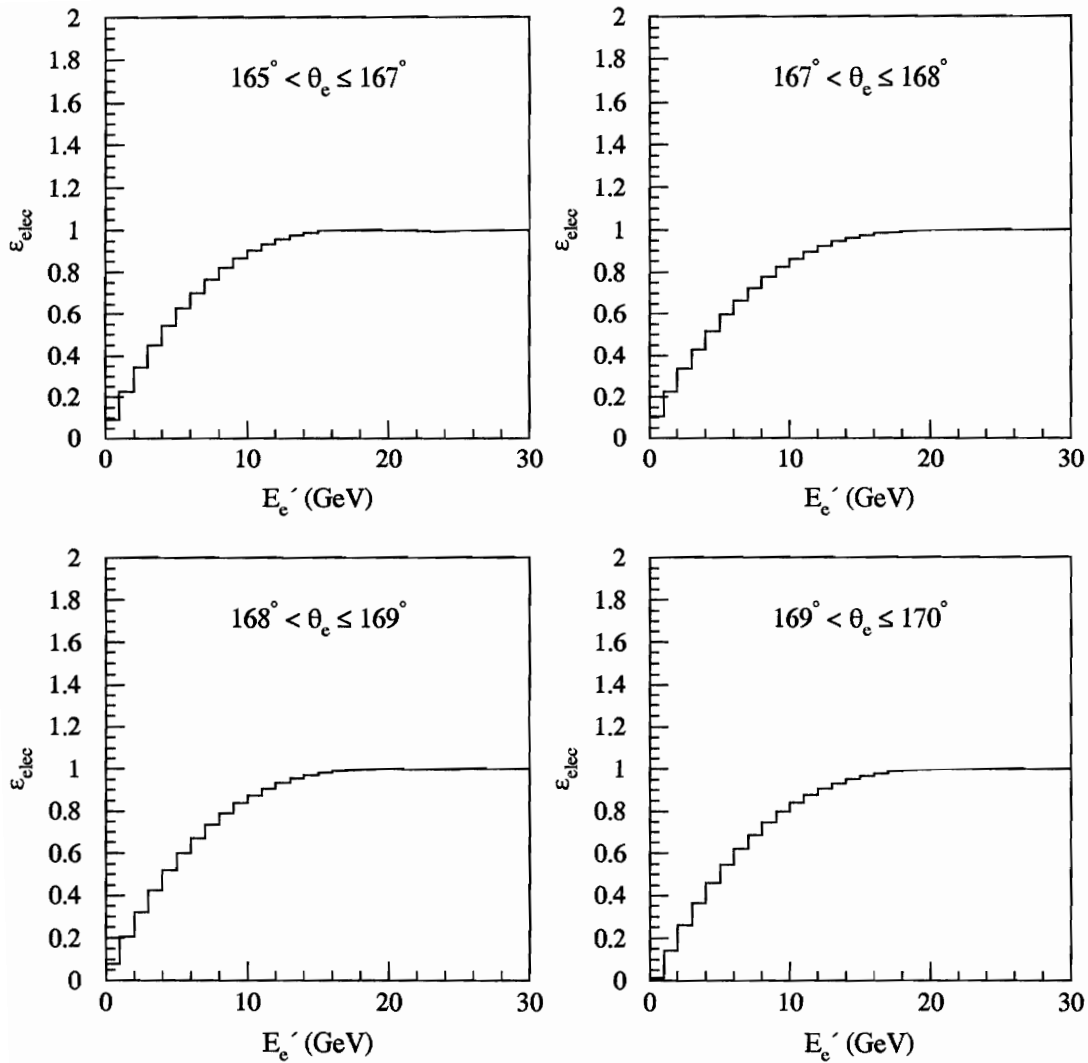


Figure 24: Scattered electron identification efficiency as a function of E'_e in four bins of θ_e . The calculations were done with Monte Carlo data which had been processed through MOZART.

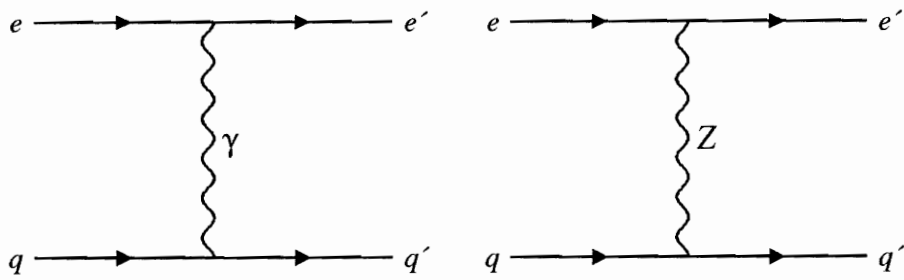


Figure 25: One boson exchange diagrams for DIS. The electron, e , exchanges a virtual photon, γ , or Z boson with a quark, q .

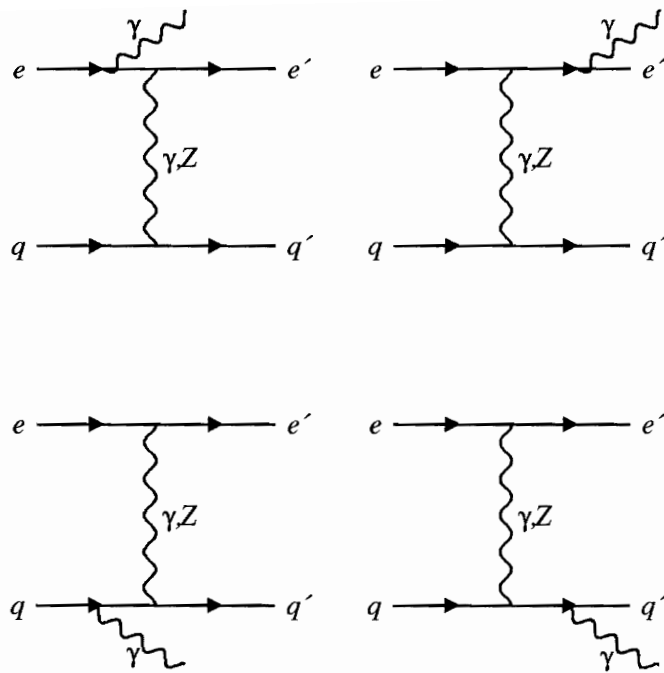


Figure 26: One photon emission diagrams in DIS. Either the initial state electron, e , final state electron, e' , initial state quark, q , or final state quark, q' , can emit a real photon during the interaction.

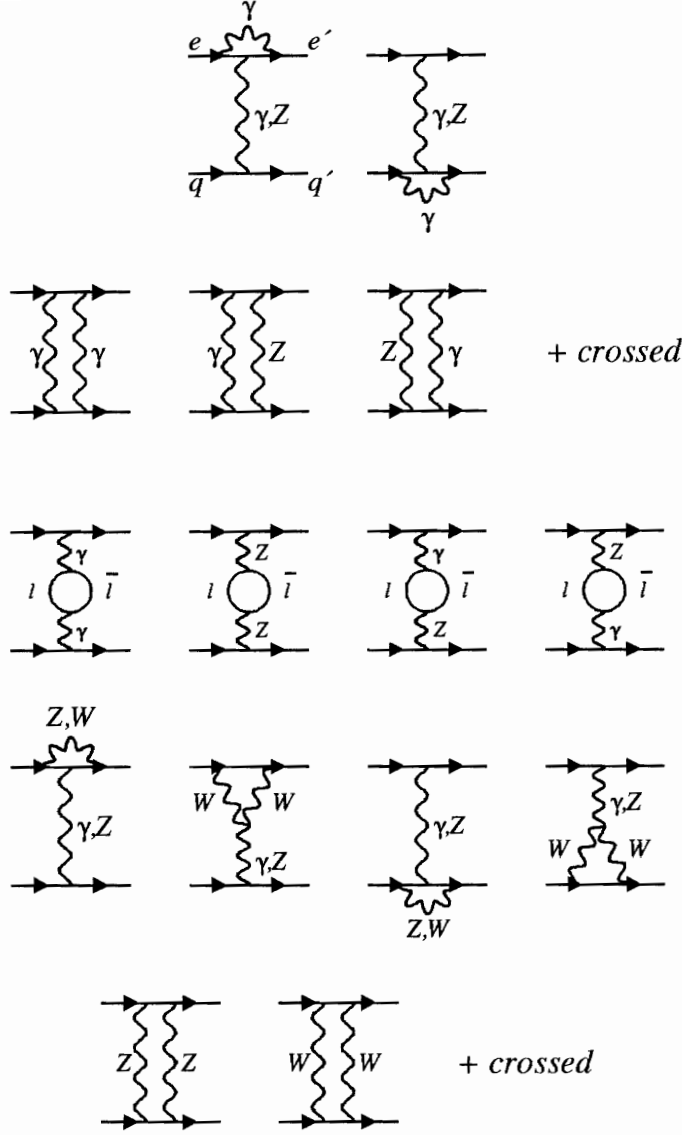


Figure 27: One loop diagrams in DIS. The initial state electron is represented by e , the initial state quark by q , the final state electron by e' , and the final state quark by q' . $l\bar{l}$ represents any charged lepton-antilepton pair. The exchanged, emitted, and absorbed particles are virtual photons (γ), Z bosons, and W bosons.

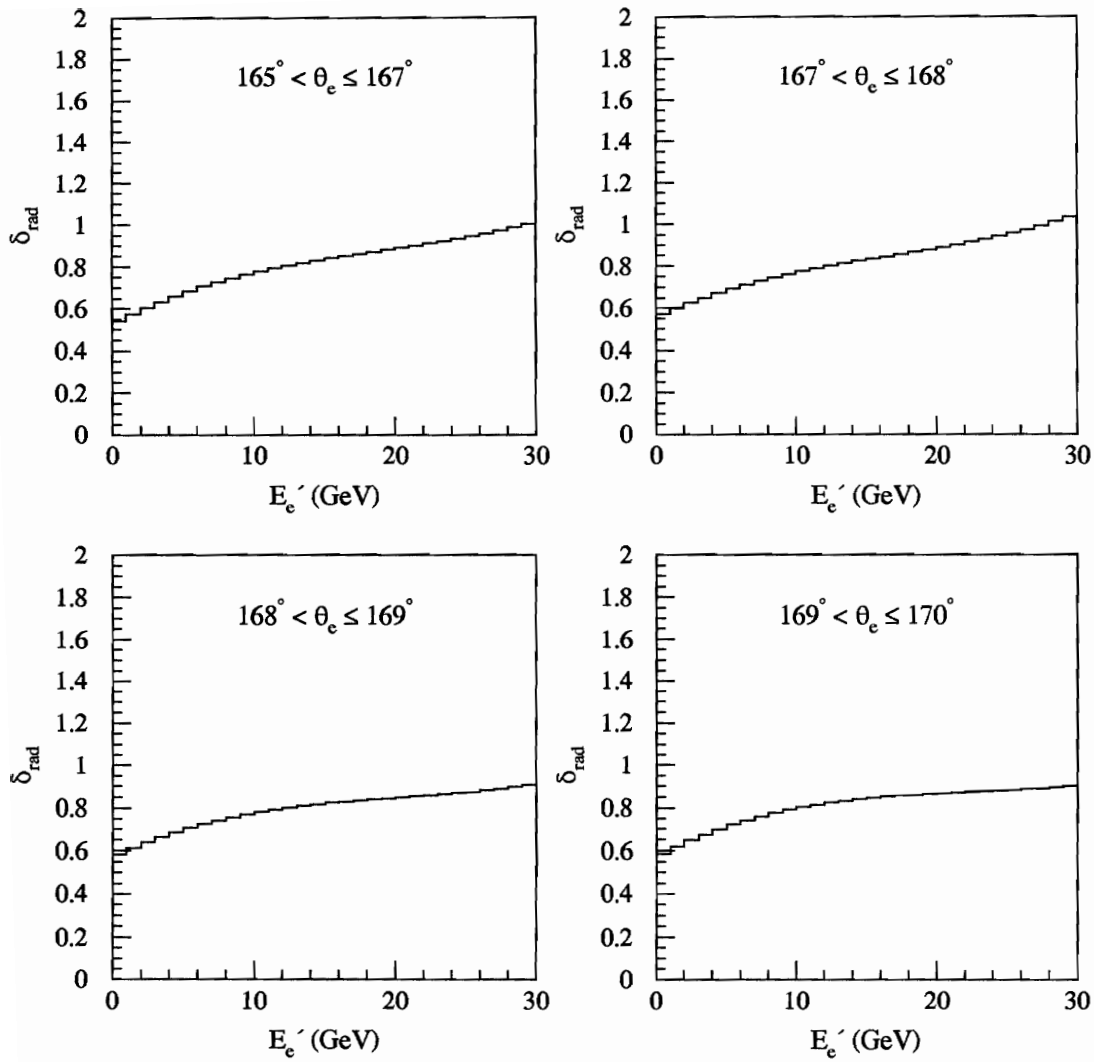


Figure 28: Radiative corrections as a function of E'_e in four bins of θ_e . The radiative corrections were calculated with HERACLES.

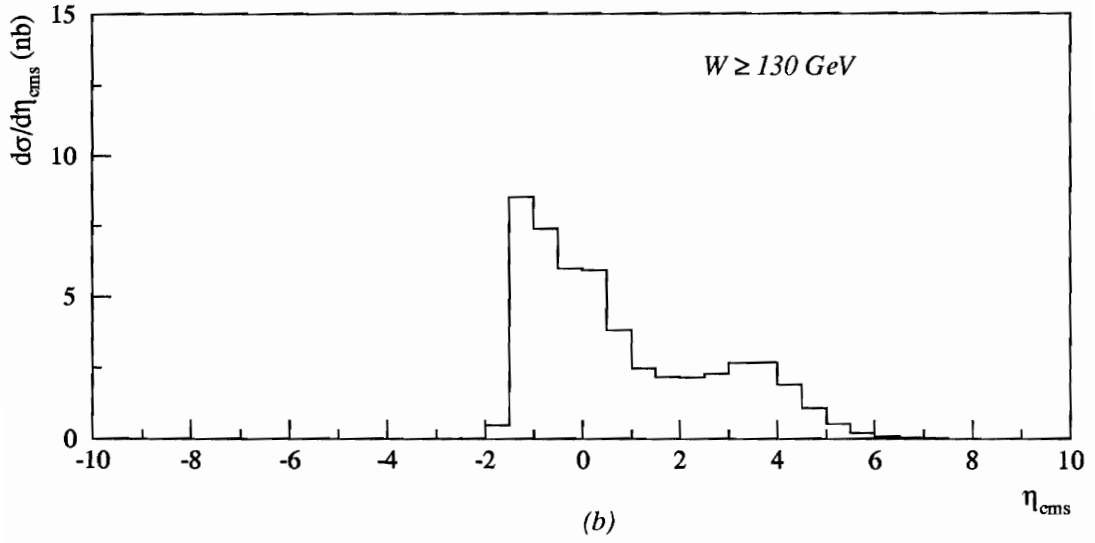
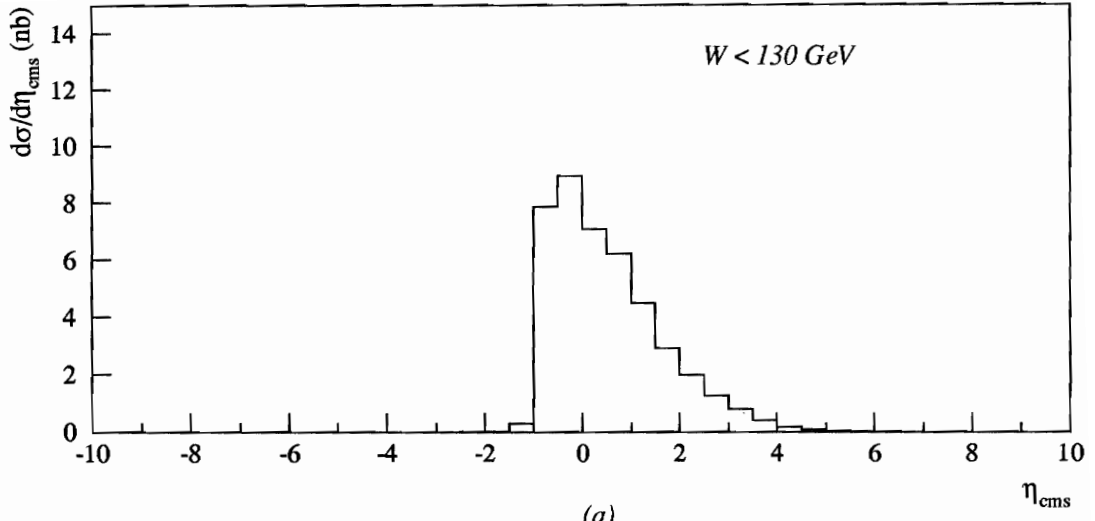


Figure 29: The η_{cm} distribution for (a) $W < 130 \text{ GeV}$ and (b) $W \geq 130 \text{ GeV}$.

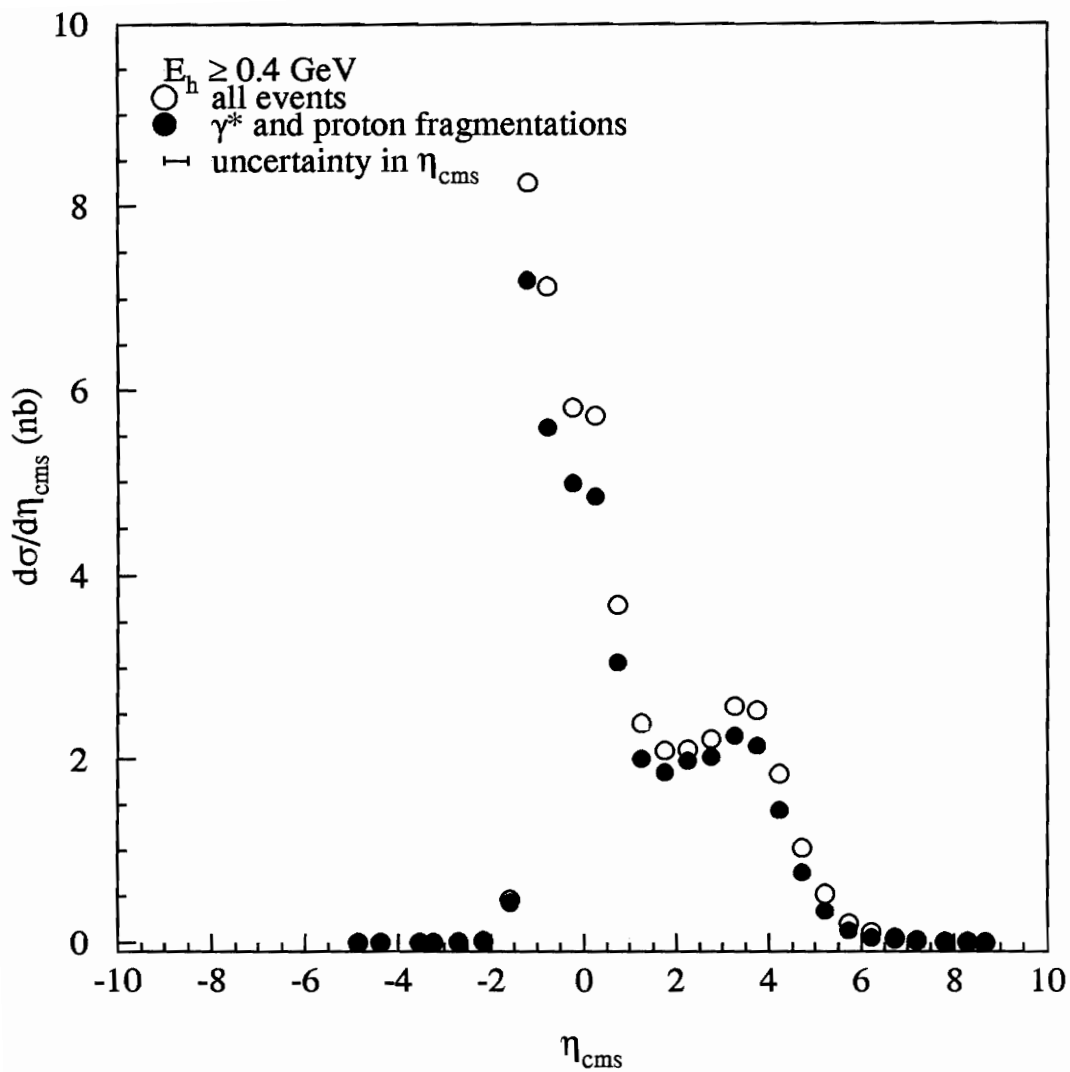


Figure 30: The η_{cms} distribution for all events (open points) and for events where hadrons are observed in both the proton and photon fragmentation regions (closed points).

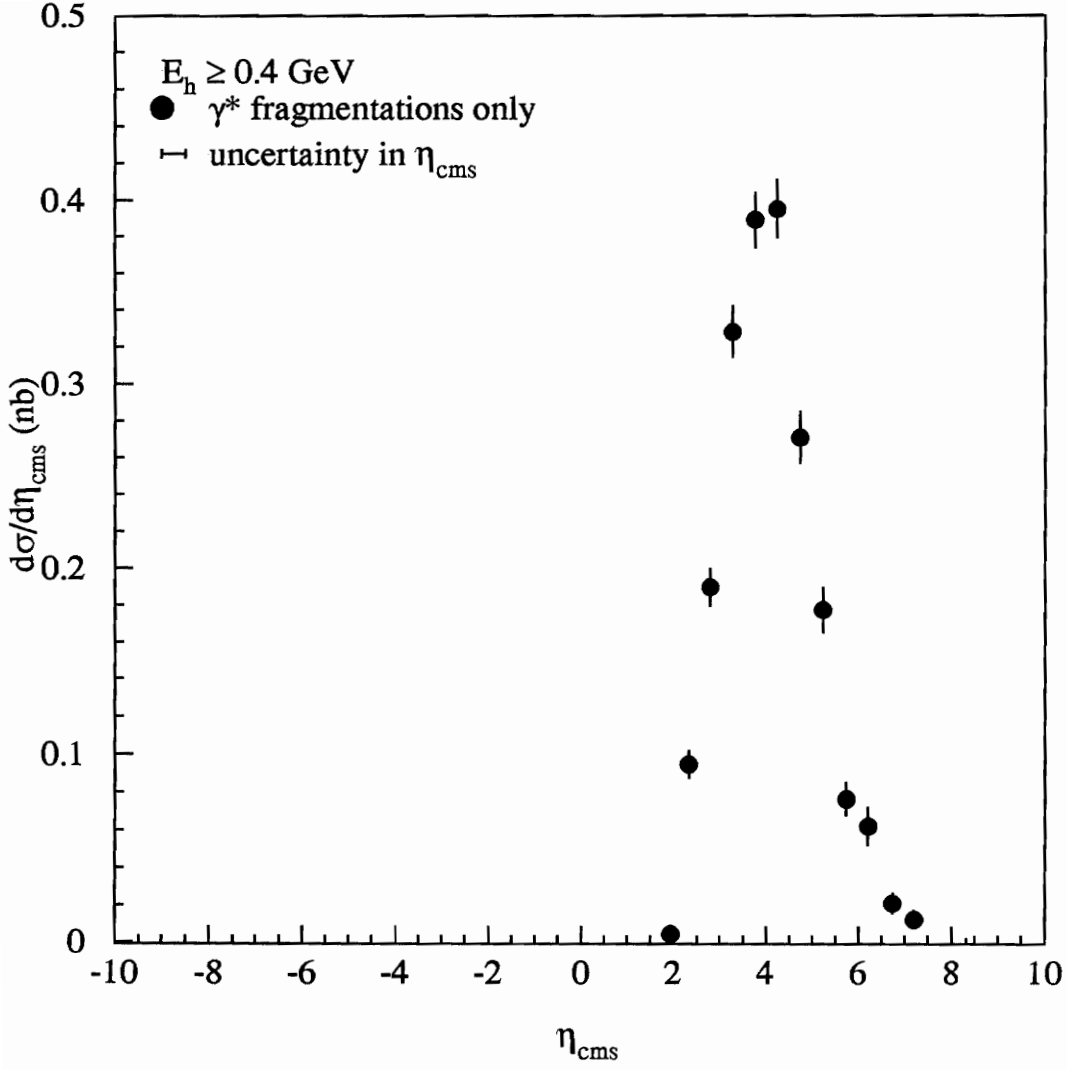


Figure 31: The η_{cms} distribution for events in which hadrons are observed only in the photon fragmentation region. Errors appear as bars on the points.

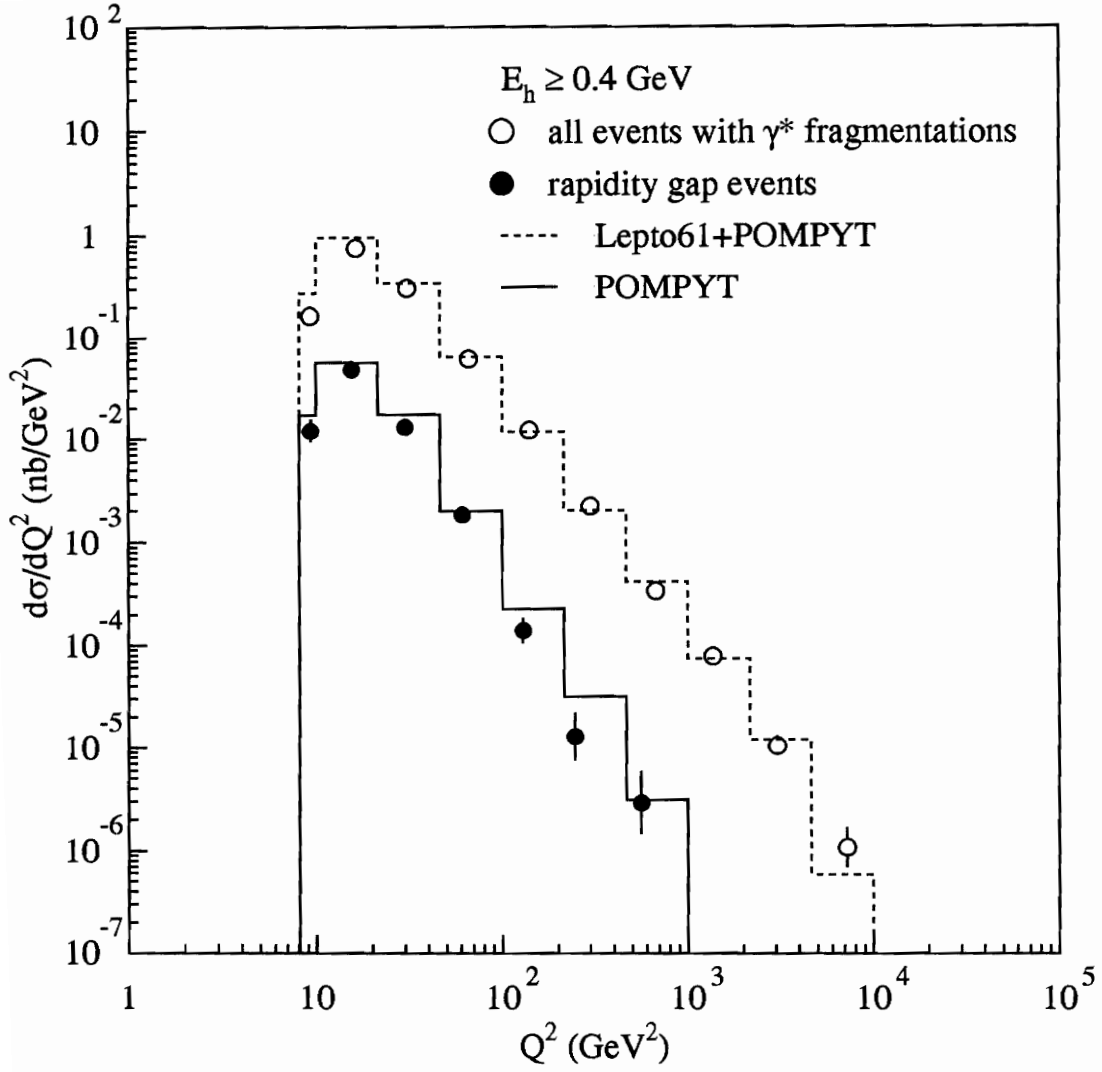


Figure 32: The differential cross section for virtual photon fragmentation with respect to Q^2 . The abscissa point for each bin is the average Q^2 of all events in the bin, and errors are plotted as bars on the points. The differential cross section obtained from the POMPYT simulation is also shown.

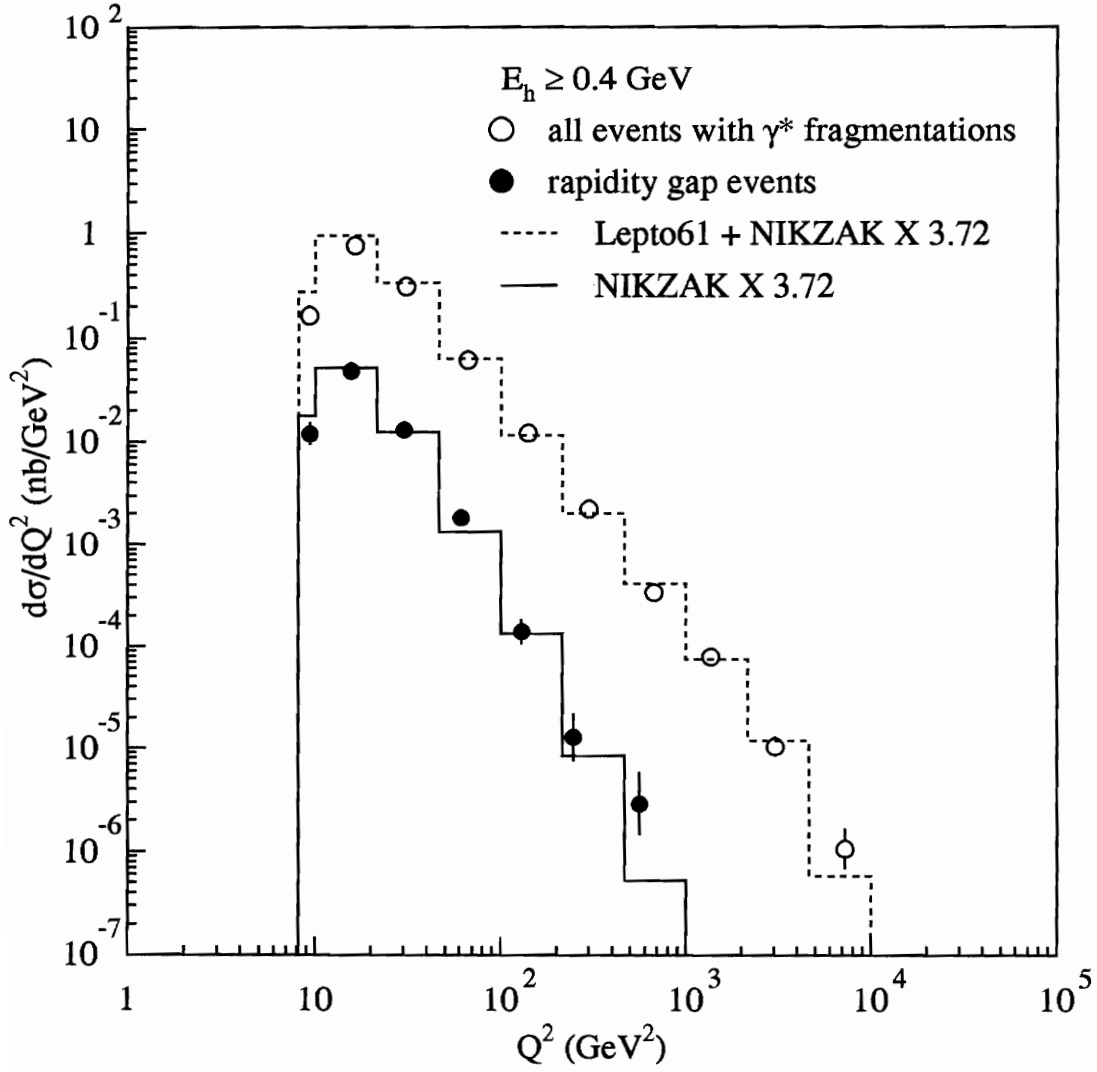


Figure 33: The differential cross section for virtual photon fragmentation with respect to Q^2 . The abscissa point for each bin is the average Q^2 of all events in the bin, and errors are plotted as bars on the points. The differential cross section obtained from the NIKZAK simulation is also shown.

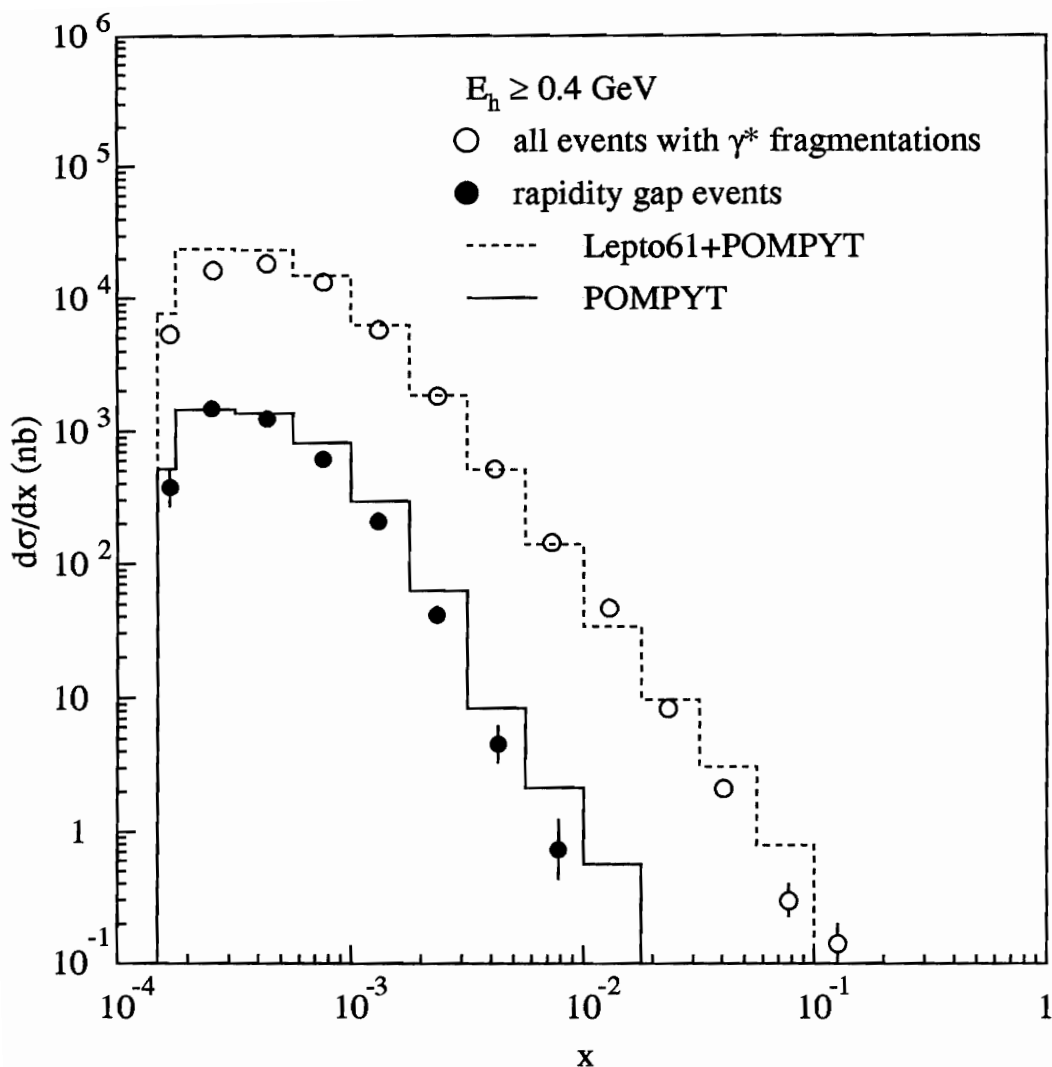


Figure 34: The differential cross section for virtual photon fragmentation with respect to x . The abscissa point for each bin is the average x of all events in the bin, and errors are plotted as bars on the points. The differential cross section obtained from the POMPYT simulation is also shown.

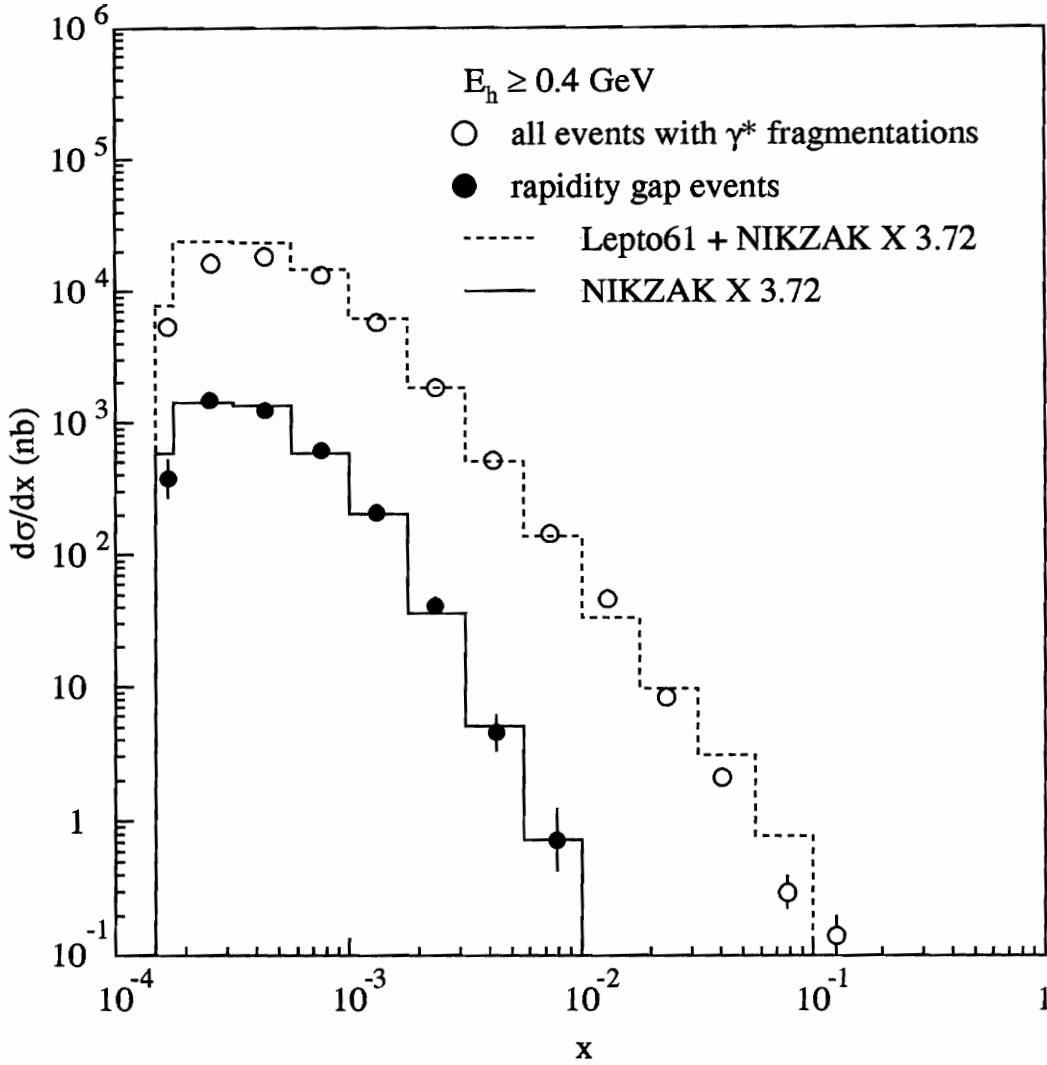


Figure 35: The differential cross section for virtual photon fragmentation with respect to x . The abscissa point for each bin is the average x of all events in the bin, and errors are plotted as bars on the points. The differential cross section obtained from the NIKZAK simulation is also shown.

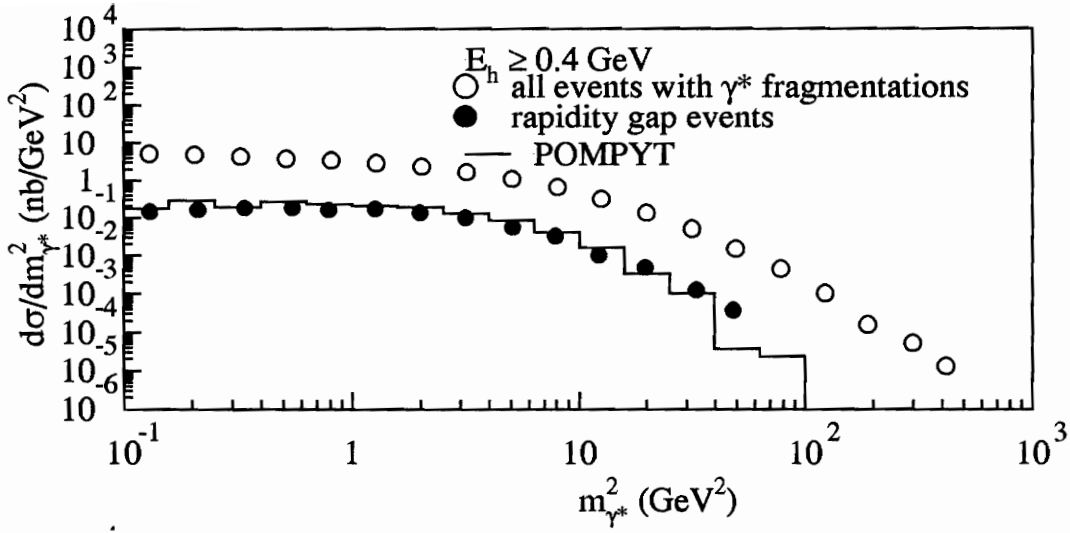


Figure 36: The differential cross section for virtual photon fragmentation with respect to $m_{\gamma^*}^2$. The abscissa point for each bin is the average $m_{\gamma^*}^2$ of all events in the bin, and errors are plotted as bars on the points. The differential cross section obtained from the POMPYT simulation is also shown.

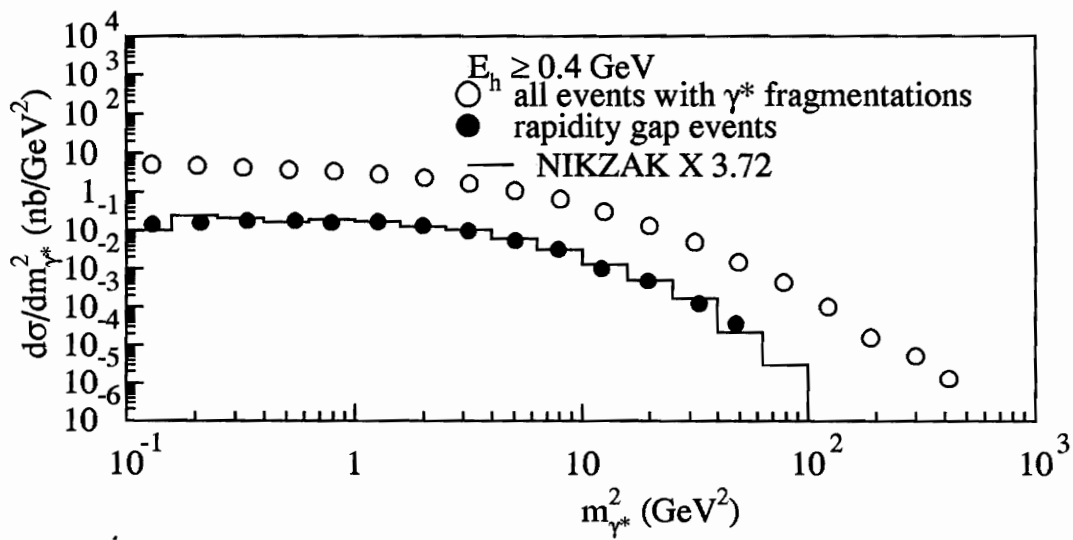


Figure 37: The differential cross section for virtual photon fragmentation with respect to $m_{\gamma^*}^2$. The abscissa point for each bin is the average $m_{\gamma^*}^2$ of all events in the bin, and errors are plotted as bars on the points. The differential cross section obtained from the NIKZAK simulation is also shown.

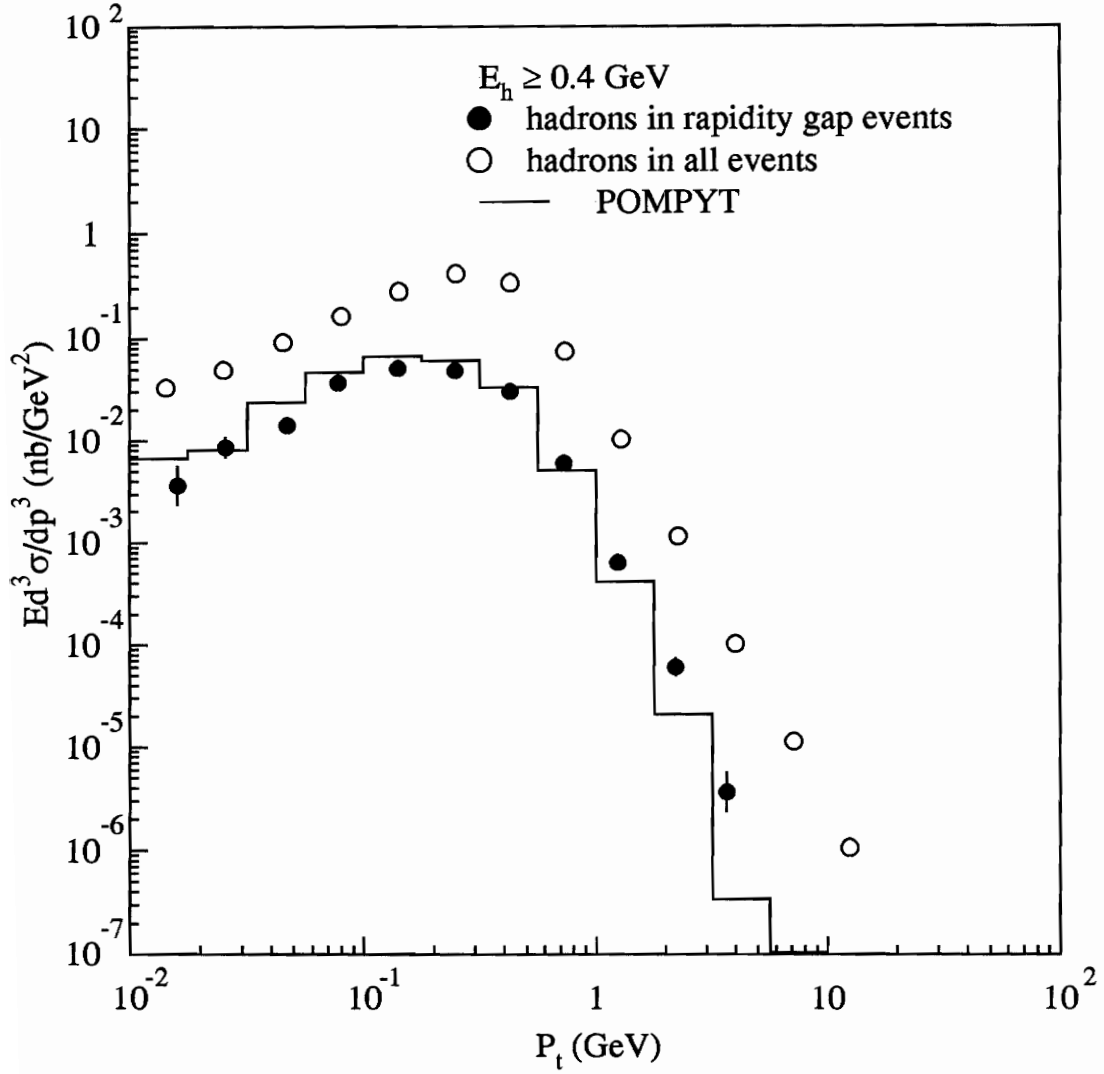


Figure 38: The invariant cross section versus the CMS transverse momentum, P_t , for hadrons in the photon fragmentation region. The abscissa point for each bin is the average P_t of all hadrons in the bin, and errors are plotted as bars on the points. The invariant cross section obtained from the POMPYT simulation is also shown.

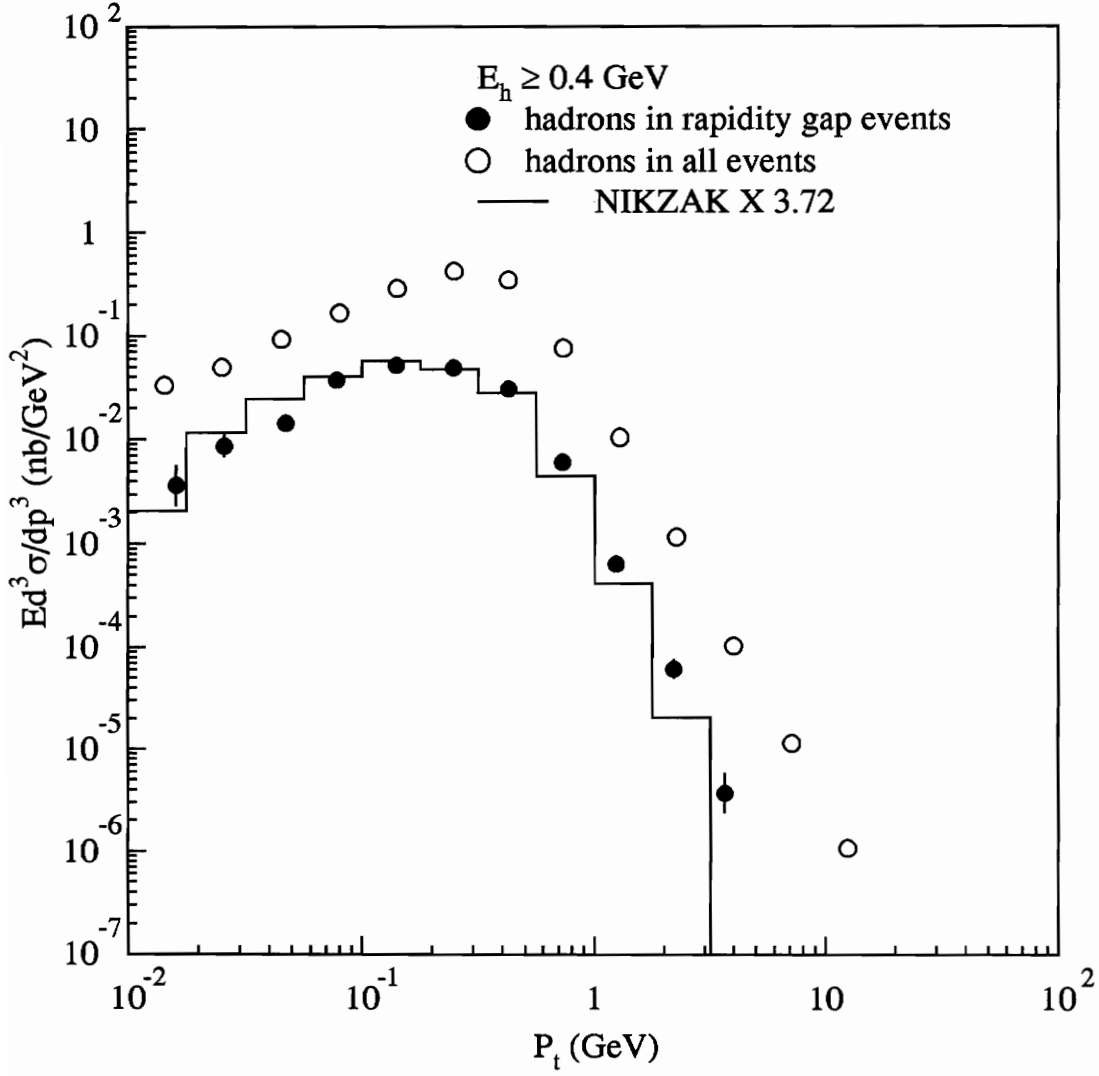


Figure 39: The invariant cross section versus the CMS transverse momentum, P_t , for hadrons in the photon fragmentation region. The abscissa point for each bin is the average P_t of all hadrons in the bin, and errors are plotted as bars on the points. The invariant cross section obtained from the NIKZAK simulation is also shown.

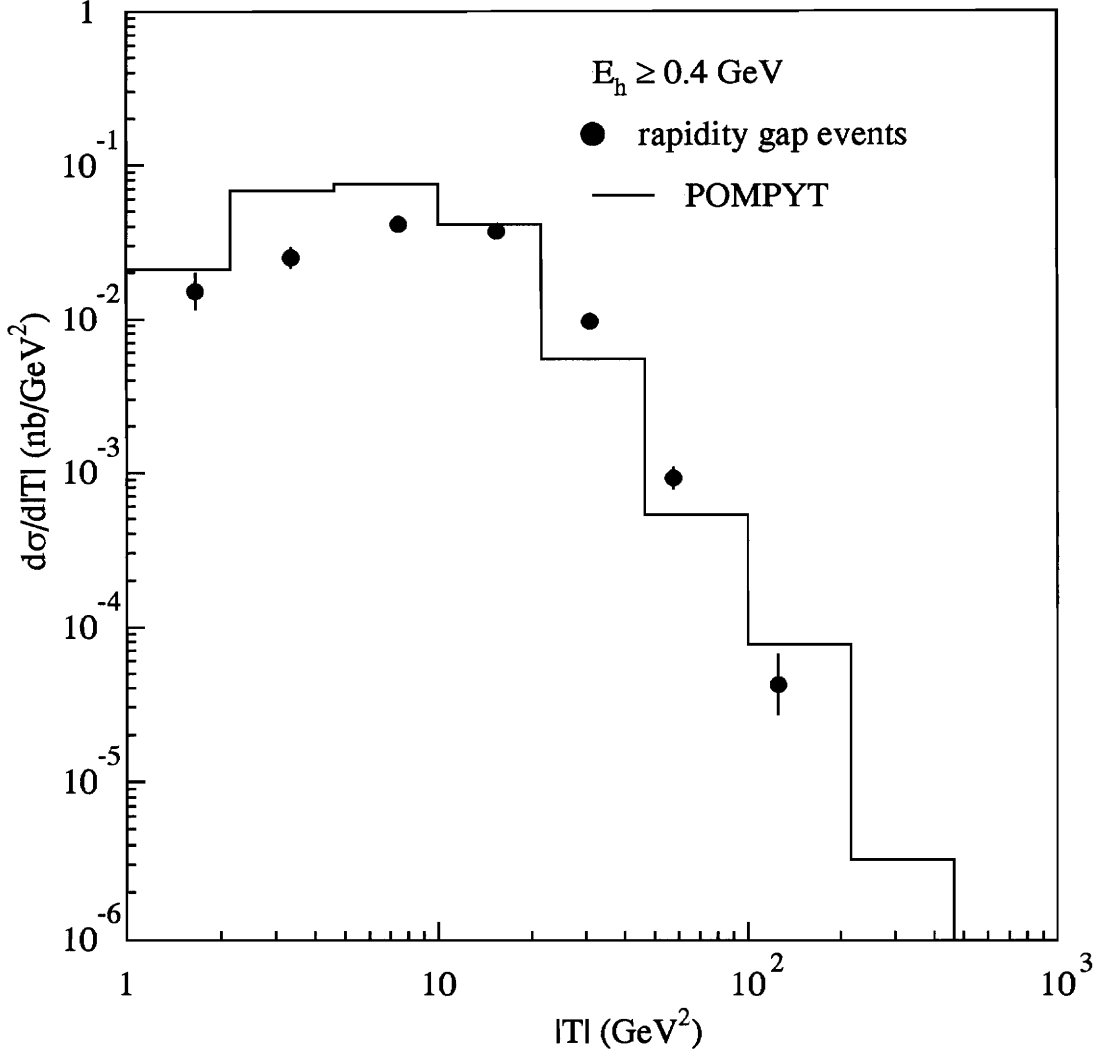


Figure 40: The differential cross section for the rapidity gap process with respect to $|T|$, where T is the square of the four-momentum transfer to the virtual photon system. The abscissa point for each bin is the average $|T|$ of all events in the bin, and errors are plotted as bars on the points. The differential cross section obtained from the POMPYT simulation is also shown.

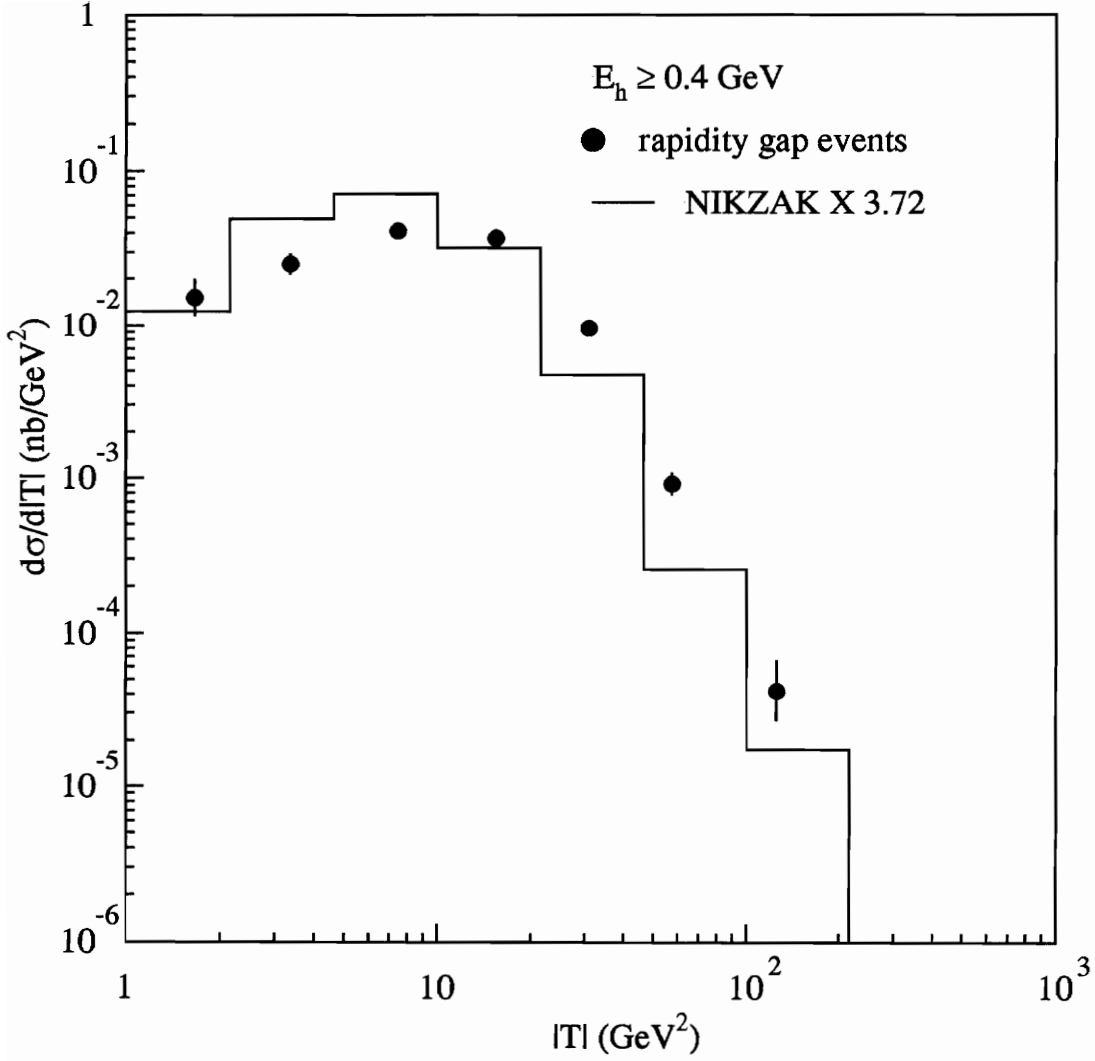


Figure 41: The differential cross section for the rapidity gap process with respect to $|T|$, where T is the square of the four-momentum transfer to the virtual photon system. The abscissa point for each bin is the average $|T|$ of all events in the bin, and errors are plotted as bars on the points. The differential cross section obtained from the NIKZAK simulation is also shown.

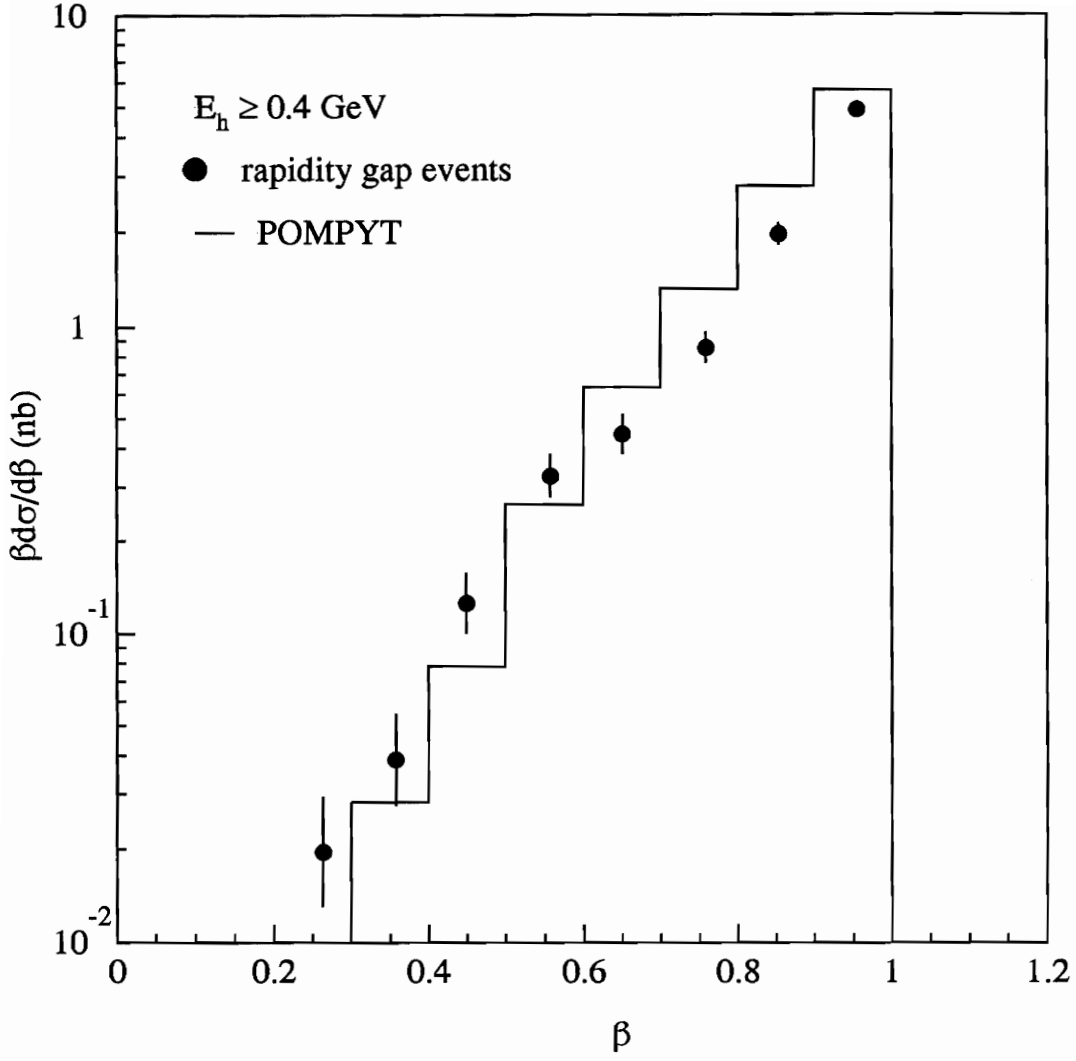


Figure 42: $\beta d\sigma/d\beta$ versus β for the rapidity gap process. The abscissa point for each bin is the average β of all events in the bin, and errors are plotted as bars on the points. $\beta d\sigma/d\beta$ obtained from the POMPYT simulation is also shown.

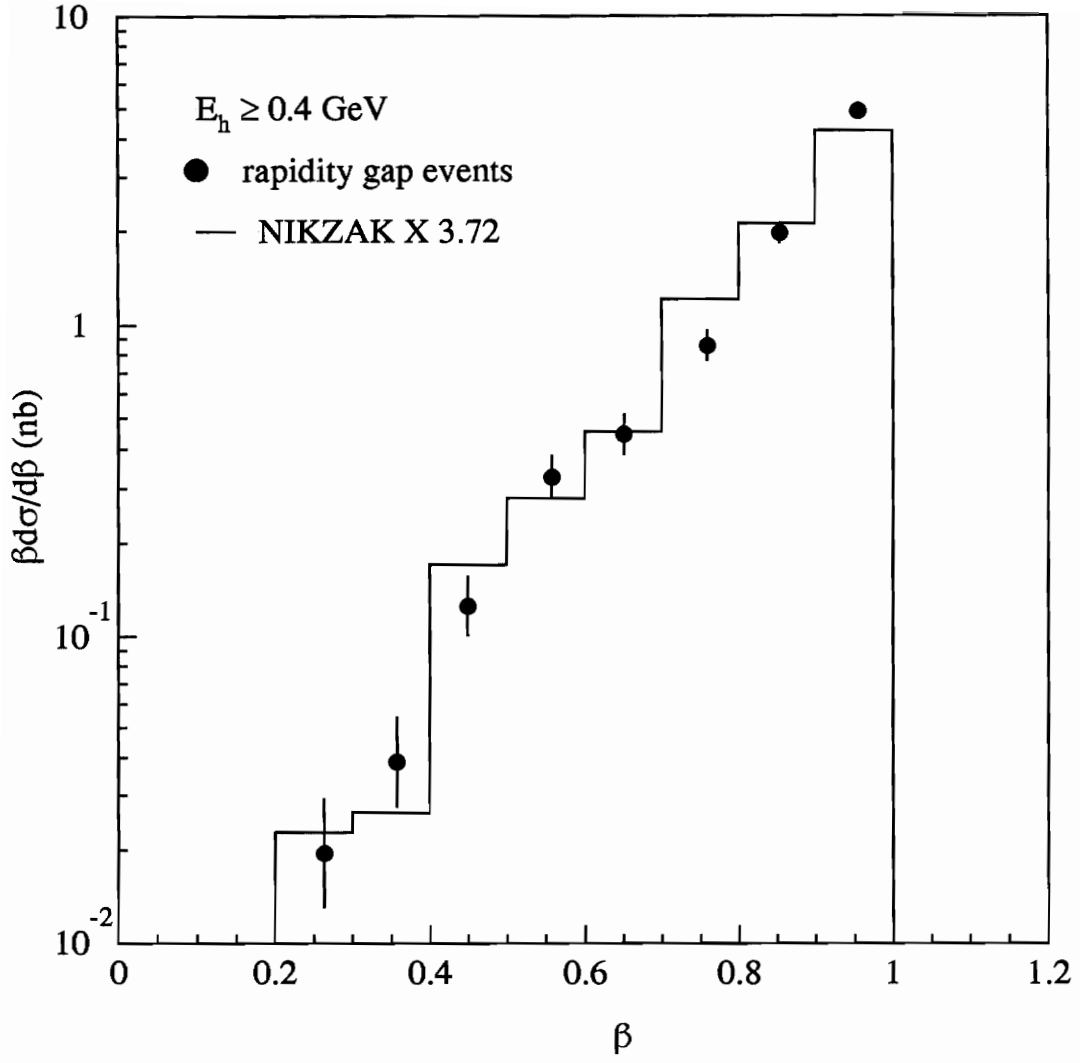


Figure 43: $\beta d\sigma/d\beta$ versus β for the rapidity gap process. The abscissa point for each bin is the average β of all events in the bin, and errors are plotted as bars on the points. $\beta d\sigma/d\beta$ obtained from the NIKZAK simulation is also shown.

Vita

Born in Arlington, Virginia in 1966, Keith Blankenship was reared in Manassas, Virginia. He graduated from the Virginia Commonwealth University in Richmond, Virginia in 1988, receiving bachelor's degrees in both Mathematics and Music. He worked for two years in the Cost Analysis and Research Division of the Institute for Defense Analyses in Alexandria, Virginia before entering the graduate school of the Virginia Polytechnic Institute and State University in 1990. He was the recipient of the Philip Morris Fellowship designated for a first-year graduate student in physics. The research for his doctoral dissertation took him to the laboratory DESY in Hamburg, Germany for one and one-half years. Besides the discipline of physics, his interests include swimming, running, weightlifting, and reading the biographies of great American luminaries.

Keith Blankenship